THE UNIVERSITY OF QUEENSLAND
AUSTRALIA

New Insights into Organic Light Emitting Devices: photophysics, recombination, and out coupling

Fatemeh Pegah Maasoumi

A thesis submitted for the degree of Doctor of Philosophy at

The University of Queensland in 2016

School of Mathematics and Physics

Abstract

Display technology is expected to have a market industry value greater than 70 billion US dollars by 2026. Although organic light emitting devices have found their way into the display industry, there is still a need for higher device efficiencies, lower cost materials, and easier, scalable production methods. This drives the need to gain a deeper understanding of organic semiconductors, which can pave the way to these goals. As such, there is undeniable demand for new classes of semiconductor materials, ideally with a high photoluminescence quantum yield, balanced charge transport, and high light out-coupling through dipole engineering.

This thesis describes a body of work which specifically addresses the task of independent control over luminescent, transport and processing properties of organic semiconducting materials with dendritic structures. A family of Ir(III) complexes is introduced and studied including dendrimers; poly(dendrimers); and co-polymers. In the first instance, photo-physical and electrical properties of materials are described, before building on this knowledge to develop efficient organic light emitting diodes. The dipole orientation was furthermore studied in these materials as an intrinsic property of with a view to achieving higher out coupling. Finally, moving away from a material-centric approaches and dendritic design, the charge transport and emissive properties of organic semiconductors were simultaneously studied in a heterostructure light-emitting field effect transistor by cryogenic techniques.

The main findings from this research were as follows: I) the photophysical properties improved by increasing the number of dendron branches in the dendritic structure. This delivers extra insulating space between the chromophore cores which leads to less concentration quenching; II) combining dendrimers with a polymer backbone was beneficial not only toward improving the film quality but also providing heteroleptic structures which are more likely to contain horizontally oriented emissive dipoles; III) the results of temperature-dependent measurements demonstrated that, as the device was cooled down, the intrinsic hole mobility followed an Arrhenius response with the overall EQE increases.

The implications of these findings are toward simplifying the device structures using more efficient devices. This can be achieved by means of highly luminescent materials as well as enhancement in device out coupling, meaning that light can be emitted preferably perpendicular to the device output plane. The fundamental studies also established some ground rules for engineering high radiative efficiencies in light-emitting field effect transistors, which should aid in

both material and architecture design for future device iterations. Future work may concentrate on chemically engineering the material structures for better properties as well as control over dipole orientation.

Declaration by author

This thesis is composed of my original work, and contains no material previously published or written by another person except where due reference has been made in the text. I have clearly stated the contribution by others to jointly-authored works that I have included in my thesis.

I have clearly stated the contribution of others to my thesis as a whole, including statistical assistance, survey design, data analysis, significant technical procedures, professional editorial advice, and any other original research work used or reported in my thesis. The content of my thesis is the result of work I have carried out since the commencement of my research higher degree candidature and does not include a substantial part of work that has been submitted to qualify for the award of any other degree or diploma in any university or other tertiary institution. I have clearly stated which parts of my thesis, if any, have been submitted to qualify for another award.

I acknowledge that an electronic copy of my thesis must be lodged with the University Library and, subject to the policy and procedures of The University of Queensland, the thesis be made available for research and study in accordance with the Copyright Act 1968 unless a period of embargo has been approved by the Dean of the Graduate School.

I acknowledge that copyright of all material contained in my thesis resides with the copyright holder(s) of that material. Where appropriate I have obtained copyright permission from the copyright holder to reproduce material in this thesis.

Publications during candidature

Peer-reviewed journal articles

- D. Gendron, E. Gann, K. Pattison, **F. Maasoumi**, C. E. McNeill, S. E. Watkins, P. L. Burn, B. J. Powell and P. E. Shaw, *"Synthesis and properties of pyrrolo[3,2-b]pyrrole-1,4-diones (isoDPP) derivatives",* Journal of Materials Chemistry C, *2*, 4276–4288, (**2014**).
- **F. Maasoumi**, M. Ullah, P. E. Shaw, J. Li, P. L. Burn, P. Meredith and E. B. Namdas, *"Charge transport and recombination in heterostructure organic light emitting transistors",* Organic Electronics, *25*, 37-43, (**2015**).
- K. Muhieddine, M. Ullah, **F. Maasoumi**, P. L. Burn and E. B. Namdas, *"Hybrid Area Emitting Transistors: Solution Processable and with High Aperture Ratios"*, Advanced Material, 27(42), 6677-6682, (**2015**).
- A. Armin, P. Wolfer, P. E. Shaw, M. Hambsch, **F. Maasoumi**, M. Ullah, E. Gann, C. R. McNeill, J. Li, Z. Shi, P. L. Burn and P. Meredith, *"Simultaneous enhancement of charge generation quantum yield and carrier transport in organic solar cells ",* Journal of Materials Chemistry C, 3(41), 10799-10812, (**2015**).
- M. Ullah, R. Wawrzinek, **F. Maasoumi**, S. C. Lo and E. B. Namdas, *"Transparent and low voltage operating organic light emitting transistors processed at low temperature ",* Advanced Optical Materials, 3(0), 1-5, **(2016)**.

Conference presentation

- **F. Maasoumi**, M. Ullah, P. E. Shaw, J. Li, P. L. Burn, P. Meredith and E. B. Namdas, *"Charge transport and recombination in heterostructure organic light emitting transistor*s", Organic Field Effect Transistors XII, SPIE Optics and Photonics , San Diego USA, **(2015)**, poster presentation.

Publications included in this thesis

- **F. Maasoumi**, M. Ullah, P. E. Shaw, J. Li, P. L. Burn, P. Meredith and E. B. Namdas, *"Charge transport and recombination in heterostructure organic light emitting transistors"*, Organic Electronics, *25*, 37-43, (**2015**).

Incorporated as Chapter 6.

Contributor	**Statement of contribution**
F. Maasoumi	Designed experiments (80%) Device fabrication (90%) Paper writing (80%) Paper editing (10%)
Dr M. Ullah	Designed experiments (10%) Device fabrication (10%) Paper writing (10%) Paper editing (15%)
Dr P. E. Shaw	Photophysical characterisation (100%) Paper writing (10%) Paper editing (10%)
Dr J. Li	Polymer synthesis (100%) Paper editing (10%)
Prof. P. L. Burn	Project supervision Paper editing (15%)
Prof. P. Meredith	Project supervision Paper editing (20%)
Dr E. B. Namdas	Project supervision Designed experiments (10%) Paper editing (20%)

Contributions by others to the thesis

Chapter 3

The iridium dendrimer used for study was synthesised by Dr. Renji Wang. The ellipsometry measurements were performed by Dr. Ravi Chandra Raju Nagiri on films that I prepared. The photoelectron spectroscopy in air (PESA) measurements of ionization potential were performed by Dr. Dani Stoltzfus at CSIRO in Clayton, Melbourne on films that I prepared.

Chapter 4

The dendrimer and poly(dendrimer) compounds were designed by Prof. Paul L. Burn and synthesised by Dr. Ross D. Jansen-van Vuuren. The ellipsometry measurements were performed by Dr. Ravi Chandra Raju Nagiri on films that I prepared. The photoelectron spectroscopy in air (PESA) measurements of ionization potential were performed by Dr. Dani Stoltzfus at CSIRO in Clayton, Melbourne on films that I prepared.

Chapter 5

The co-polymer dendrimers were designed by Prof. Paul L. Burn and synthesised by Dr. Ross D. Jansen-van Vuuren. The photoelectron spectroscopy in air (PESA) measurements of ionization potential were performed by Dr. Dani Stoltzfus at CSIRO in Clayton, Melbourne on films that I prepared.

Chapter 6

The DPP-DTT polymer was synthesised by Dr. Jun Li from the institute of Material Research and Engineering, Singapore. Dr. Mujeeb Ullah designed the asymmetric shadow masks. Dr. Ullah also provided guidance and help in first device fabrication. The temperature dependent photoluminescent measurement on Super Yellow was performed by Dr. Paul E. Shaw. The silicon nitride substrates were diced by Khalid Muhieddine.

This thesis would not been possible without the collaboration with the CSIRO, Clayton, Melbourne. Dr. Mark Bown, Dr. Chris Dunn and Dr. Jenny O'Connell who supervised the OLED device fabrication and characterisation procedures carried out in the work described in this thesis.

Statement of parts of the thesis submitted to qualify for the award of another degree

None.

Acknowledgements

With these acknowledgements, I hope to do justice to the tremendous debt of gratitude I owe to those who have supported me through love, friendship and intellect, and helped and inspired me to be the researcher I am today.

To my mom, Zohreh Shahbazi, words are not enough for me to offer my affectionate gratitude for your incredible dedication during my entire life. You are the one who planted the idea of being a researcher by taking me as your companion on all your medical conferences. Distance may separate us but I always feel like the luckiest girl to have you as my mom, my teacher, my best friend.

To Pouria, my lovely brother, I miss you to bits. I still can't believe how hard it is to be so far from my life shadow. It was you who took over my responsibilities back home so that I could pursue my dreams. I owe you one. To John Lindorfer, my wonderful godfather, you filled my life not only with your fatherly kindness and support but with all the experience, wisdom, and knowledge you shared with me. You taught me to be a positive fighter just as you have been. A flash back to my M.Phil, I would like to sincerely thank Prof. Alireza Bahrampour. It was you who encouraged me a lot to pursue science. I wouldn't be able to strive for my dreams here in the first place if it wasn't for your guidance and support.

To my PhD supervisors, Prof. Paul Meredith and Dr. Ebinazar Namdas. Paul, thank you so much for taking me on as your student and also standing beside me for a long time to get me to Australia. I am so grateful to have you not only as my supervisor but also as someone who listened to me and helped me with my decisions. Ebinazar, thank you so much for always having your door open to me, and being willing to discuss anything and everything that needed discussing. I really appreciate your responsible and kind heart in supervision. To Prof. Paul Burn, thank you for profound insights and guidance throughout my PhD. I am grateful to have worked with a pioneer in the field.

To Dr. Ardalan Armin, pal, what can I say, you were my mentor from the very first step in the lab. To say that you provided me with the tools and support I needed. My eternal thanks to you for teaching me so much of the science that I am pursuing now, giving me confidence and for wonderful discussions we have had on just about every topic. To Dr. Mike Hambsch, thank you for all of the scientific advice and thanks for taking me for running, cycling, hiking and all the fun times we had together. You always talk me down from every ledge just like you were next to me, even from the other side of the globe.

Dr. Paul Shaw, it was with you and Dr. Mujeeb Ullah, that I have learned a great deal of experimental skills. A special thanks to both of you for all of the training, help and fruitful discussions. Dr. Andrew Clulow, many thanks for teaching me a lot more chemistry, English and also beer brewing skills (I will attempt to do that sometime!).

To Khalid, my PhD buddy, we did it. My PhD journey was a lot easier with you making the bad days seem not as bad. Thanks for showering me with your limitless kindness, support and 24/7 proofreading of whatever I wrote. Thanks for giving me heart even when you needed it most. To Dr. Kristen Tandy, thanks for all the hugs and letters. You were such a lovely friend who supported me in tough times when I needed it the most. Dr. Ross Van Vuuren, thank you so much for your great materials, all the social activities and fruitful discussions. To Steven, you‘ve never hesitate to help me with my urgent chemistry enquiries, thank you and good luck with your PhD.

I have to give a big thank you to the amazing scientists in CSIRO, Dr. Mark Bown, Dr. Chris Dunn, and Dr. Jenny O’Connell. You came along just when I needed and are some of the most enthusiastic and positive people I have ever met in science. I am so lucky to have had the opportunity to work with you.

A substantial amount of thanks to Murray Kane and Stephanie Golding, SMP postgraduate administrative officers and Rob Kembery, the business manager at COPE, for all of the help you have provided me with and your immense patience. To Rob Webb and Helmut Land at the UQ chemistry workshop, a special thanks to both of you for making and fixing all the precious equipment.

To the wonderful crew at COPE, who helped me with bits and pieces in and out of the lab. In no particular order: Helen, Vincent, Ravi, Robert, Soniya, Renji, Ajay, Fan, Ajeesh, Martin, Aren, Larry, Kinitra. Thank you; I couldn’t ask for a better crowd to work with.

Last and not least, to the family I was privileged enough to choose.

Nahid and Mehdi, with you guys I feel loved, thanks for being my siblings away from home. To continue on the note of feeling home, I must mention the wonderful Marianne and Luke. You took so much care of me, without even asking or needing to be asked (especially at big T time). You are my Australian family forever. To Safa, thanks for your sisterly love and support. To Sahar, thanks for sending me positive energy. To the lovely couple, Nasim and Farid, thanks for your awesome tea time company. To a special couple, Niloufar and Behnam thanks for the peaceful times you gave me.

A special thanks to my amazing housemates, Shao, Swathi, Ely. Shao, thanks for your thoughtfulness and for always being happy to help. It was nice to get out and talk about everything other than work. Swathi, thanks for the love, support and for making me your delicious masala tea every single morning. Ely, thanks for your excellent cheesecakes.

To Inna, thanks for the great time we had together. To Christian, you came along at the very end and when I really needed someone to remind me of joy and laughter, thanks brownie. A great deal of thanks to Saleh & Sima, Shahram, Pouria, Asha, Rob & Karrera, Michelle, Karyn, Julia. Thanks for your company and fun time.

To my best friends, Marjon, Paria, Nazli, Aboozar, Speher, and Mehrsa your eternal friendship is always a light to follow when the tunnels darken. You guys were believed in me even when I did not. I love you all.

Keywords

Organic semiconductors, light emitting, diodes, transistors, dendrimers, poly(dendrimers), iridium, photo-physics

Australian and New Zealand Standard Research Classifications (ANZSRC)

ANZSRC code: 100702, Molecular and Organic Electronics, 50%

ANZSRC code: 03030, Optical Properties of Materials, 30%

ANZSRC code: 091208, Organic Semiconductors, 20%

Fields of Research (FoR) Classification

FoR code: 1007, Nanotechnology, 50%

FoR code: 0205, Optical Physics, 30%

FoR code: 0912, Material Engineering, 20%

To Zohreh Shahbazi

My mom, My hero, My best friend….

Table of Contents

Abstract I

Declaration by author III

Publications during candidature IV

Contribution by others to the thesis VI

Acknowledgments VIII

Keywords and Classifications XI

Table of Contents XIII

List of Figures XVI

List of Tables XXII

List of Abbreviations and Symbols XXIII

Chapter 1: Introduction 1

- 1.1 Motivation 1
- 1.2 Properties of organic semiconductors 3
  - 1.2.1 Energy levels and nomenclature 4
- 1.3 Dendrimers 5
- 1.4 Luminescence and electroluminescence 6
- 1.5. Organic light emitting diodes 8
  - 1.5.1 Operating mechanism, parameters, and performance metrics 8
  - 1.5.2 Loss mechanism and dipole orientation in OLEDs 11
- 1.6 Organic light emitting field effect trabsistors 15
  - 1.6.1 Operating mechanism, parameters and performance metrics 15
  - 1.6.2 Temperature-dependent measurements 18
- 1.7 Aims of this project 20
- References 22

Chapter 2 : Experimental Methods and Equipment 28

- 2.1 Introduction 28
- 2.2 Materials 28
- 2.3 Material characteristics 29
  - 2.3.1 Energy level eastimation 29
  - 2.3.2 Absorption 29

2.3.3 Photoluminensce 29

2.3.4 Photoluminescence quantum yield 30

2.3.5 Photoluminescence decay lifetime 32

2.3.6 Ellipsometry 33

2.3.7 Dipole orientation measurement 33

2.4 Device fabrication 35

2.4.1 Substrate preparation 36

2.4.2 Thin film deposition 36

2.4.3 Film thickness determination 36

2.4.4 Contact deposition 37

2.5 Device characterisation 37

2.5.1 Standard measurements for light emission 37

2.5.2 Colourimetry 40

2.5.3 Standard OLED characterisation 42

2.5.4 Standard LEFET characterisation 43

2.5.4.1 Optical characterisation 43

2.5.4.2 Electrical characterisation 44

References 46

Chapter 3: Highly Efficient Solution-Processable Dendrimer OLEDs 47

3.1 Introduction 47

3.2 Material design and experimental methods 48

3.3 Photo-physical properties 50

3.4 Device performance 52

3.5 Dipole orientation 56

3.6 Conclusion 59

References 60

Chapter 4 : Effects of Polymerisation and Dendronisation on iridium (III) OLEDs 62

4.1 Introduction 62

4.2 Singly-dendronised dendrimer and poly(dendrimer) 63

4.2.1 Material design and experimental methods 63

4.2.2 Photo-physical properties 65

4.2.3 Device performance 69

4.2.4 Dipole orientation 73

4.3 Doubly-dendronised dendrimer and poly(dendrimer) 75

4.3.1 Material design and experimental methods 75

4.3.2 Photo-physical properties 77

4.3.3 Device performance 80

4.4 Conclusion 84

References 86

Chapter 5 : Ambipolar Poly(dendrimers) 88

5.1 Introduction 88

5.2 Material design and experimental methods 89

5.3 Photo-physical properties 91

5.4 Device performance 94

5.5 Conclusion 98

References 99

Chapter 6 : Charge Transport and Recombination in Heterostructure Organic Light Emitting Transistors 100

6.1 Introduction 100

6.2 Experimental procedure 101

6.2.1 Device fabrication 101

6.2.2 Temperature dependent measurement 103

6.2.3 Photoluminescence quantum yield measurement 105

6.3 Results and discussions 105

6.3.1 Room temperature 105

6.3.2 Variable temperature mobility measurements 108

6.3.3 Variable temperature radiative recombination efficiency 112

6.4 Conclusion 114

References 115

Chapter 7 : Summary, Conclusion, and Outlook 118

Appendix 122

List of Figures

1.1 A next generation iWatch, which will have a 1.3-1.5 inch flexible OLED-display…………...…2

1.2 a) Figure 1.2 a) The bonding system of ethene showing the σ- and π-bonds, b) the corresponding energy level diagram of ethene. The lowest energy electronic excitation shown is between the bonding π-orbital and the antibonding π*-orbital, adapted from………………………………...4

1.3 A schematic diagram of the first generation of a dendritic structure consisting of a core, branching units and surface groups………………………………………………………………5

1.4 A Jablonski diagram illustrating the possible relaxation pathways in the singlet and triplet manifolds…………………………………………………………………………………………7

1.5 OLED device structure, a) an OLED comprising a single active layer, b) a schematic mechanism of OLED operation illustrating the basic processes of electroluminescence. Holes are injected from the anode into the HOMO of the hole injection layer and pass to the hole transport layer. Electrons are injected from the cathode into the LUMO of the electron injection layer EIL and pass to the electron transport layer. Excitons are formed in the emissive layer and emission will occur, c) a multilayer OLED……………………………………………………....9

1.6 a) Schematic illustration of loss mechanisms in an OLED. With no out-coupling enhancement only a small amount of emission escapes to be observed, b) the distribution of different optical losses for a comparable fluorescent or phosphorescent emitters with similar stack layer thickness, refractive indices and emission spectra…………………………………………...…12

1.7 a) The conventional definition for dipole orientation, b) A cross-sectional schematic view of the angular dependent PL spectrum set up , c) A schematic diagram of the experimental setup with angle notations and emission polarizer orientations for recording s- and p- polarized emission, adapted from…………………………………………………………………………………14

1.8 Schematic diagrams including the p-type operating mechanisms of a) a single layer LEFET and b) a multi-layer LEFET……………………………………………………………………...16

1.9 a) Transfer characteristics of a n-type LEFET showing the source-drain current (IDS) as a function of the applied gate voltage (VG) with a fixed source-drain voltage (VDS). b) The output characteristics of the LEFET showing the IDS as a function of VDS for different values of VG……………………………………………………………………………………………18

1.10 A schematic of the Multiple Trapping and Release Model adopted from……..……………19

2.1 Schematic diagram of the experimental set up of PLQY measurement of organic thin films….30

2.2 Relationship between the optical anisotropy in films and molecular orientation………………34

2.3 Close up of the angle dependent PL spectrum setup from two directions……………………...35

2.4 Schematic device structure for OLED and LEFET……………………………………………..36

2.5 Normalized CIE 1931 eye response curve as a function of wavelength………………………..38

2.6 a) CIE 1931 colour-matching functions $\bar{x}(\lambda)$, $\bar{y}(\lambda)$, and $\bar{z}(\lambda)$ which represent red, green , blue light respectively as a function of wavelength, note that the green colour-matching function $\bar{y}(\lambda)$, is identical to the eye response curve. b) chromaticity diagram representing the possible colours the human eye can perceive with x and y co-ordinates ………………………………………….…41

2.7 Two photographs showing the experimental set-up for OLED testing utilised at the CSIRO test facility………………………………………………………………………………………….42

2.8 Photographs showing the experimental setup for LEFET testing utilised at the COPE test facility……………………………………………………………………………………….44

3.1 The chemical structures of a) G1 Ir(ppy)$_3$, b) CBP, and c) TPBi………………………………48

3.2 a) Device structure, b) energy diagram for different layers. The HOMO and LUMO of TPBi and CBP were taken from literature respectively. The work function for metals were taken from original material sheets provided by CSIRO, the energy level of G1 Ir(ppy)$_3$ were obtained from PESA measurements as explained in Chapter 2……………………………………………………….....49

3.1 Absorption and PL spectrum for G1 Ir(ppy)$_3$ in solution (solid line), in neat film (dash line), and in CBP blend film (dot line), the samples were excited at a wavelength of325 nm for PL measurements………………………………………………………………………………….51

3.4 Photoluminescence lifetime measurement (TCSPC) for G1 Ir(ppy)$_3$ in a degassed solution (square), in neat film (circle), and in CBP blend (star). The samples were excited by a 372 nm LED and the emission was detected at 515 nm (peak)……………………………………………...51

3.5 Current density and luminance characteristics for neat and CBP blend devices. The square represents the neat films while the circle represents the blends. Open grey colour show current density and solid black colour represents the luminance…………………………………….…..53

3.6 a) EL spectrum for neat and CBP blend devices, b) a close up of the working device, c) the overlapped CIE co-ordinates of both devices……………………………………………….……54

3.7 EQE values for neat and CBP blend devices……………………………………………………54

3.8 Power efficiency for both neat and CBP blend devices……………………………………...55

3.2 Refractive index and extinction coefficient for neat (dot line) and CBP blend (solid line) of G1 Ir(ppy)$_3$…………………………………………………………………………………...57

3.10 Experimental data (circles) and fitting (dash line) for angle dependent PL spectrum measurement…………………………………………………………………………………...58

3.3 Refractive index and extinction coefficient for PEDOT:PSS…………………………………..58

4.1 Chemical structures of, a) singly-dendronised dendrimers D1 and, b) singly-dendronised poly (denrimers) P1, with $\bar{M}$w of 160 kDa and a polydispersity (PDI) of 1.3…………………………...64

4.2 a) Device structure, b) energy level diagram for different layers……………………………….65

4.1 Normalized absorption (black) and PL (blue) spectra of singly-dendronised dendrimers D1 and poly (dendrimers) P1 for solution (solid line), neat film (dash line), and CBP blend film (dotted line)……………………………………………………………………………………………66

4.4 Lifetime measurements (TCSPC) for: a) singly-dendronised dendrimer (D1) and b) poly(dendrimers) (P1) in degassed solution, neat film, and CBP blend film. Comparing the solid state neat film of both compounds, it can be noted that the bi-exponential PL decay moving toward the mono-exponential decay. The samples were excited by a 372 nm LED and the emission was detected at the peak of PL spectra (520nm- 525nm)……………………………………………..67

4. 5 Current density and luminance characteristics in neat (square) and CBP blend (circle) devices for singly-dendronised: a) dendrimer (D1), and b) poly (dendrimers) (P1)………………………..70

4.7 Efficiency of devices are presented for both compounds in different units: a) EQE and b) power efficiency (left axis) and luminous efficiency (right axis)…………………………………………72

4.2 Variable angle spectroscopic ellipsometry (a and c) and angle dependent PL results (b and d) for singly-dendronised compounds D1 and P1 respectively……………………………………….74

4.3 Chemical structures of, a) doubly-dendronised dendrimer, D2, b) doubly-dendronised poly(dendrimer), P2 with a $\bar{M}_{\mathrm{w}}$ of 68 kDa and a PDI of 2.4…………………………………...…76

4.4 Energy level diagram for doubly-dendronised compounds……………………………………..76

4.5 Normalized absorption (black) and PL (blue) spectra for doubly-dendronised dendrimer, D2, and poly(dendrimer), P2, for solution (solid line), neat film (dash line), CBP blend film (dotted line), PL absorption of singly-dendronised compounds are also plotted in orange dash line for comparison…………………………………………………………………………………….……77

4.6 TCSPC measurements for a) doubly-dendronised dendrimer (D2) and b) doubly-dendronised poly(dendrimer) (P2) in degassed solution and solid states. The PL decay measurements of singly-dendronised compounds (D1 and P1) in neat film solid state are plotted as a reference in orange color. The samples were excited by a 372 nm LED and the emission was detected at the peak of PL spectra (540 nm- 545 nm)…………………………………………………………………..…79

4.7 Electrical characteristics in neat (square) and CBP blend (circle) devices for doubly-dendronised :a) dendrimer D2, and b)poly(dendrimer) P2…………………………………………………......81

4.8 Electroluminescent spectrum for doubly-dendronised compounds in neat (solid line), and CBP blend (dotted line) devices: a) D2, b) P2, The EL spectra of their singly-dendronised counterparts are plotted in orange colour as reference, c) CIE co-ordinates, and d) close up of actual performing device………………………………………………………………………………………..82

4.9 Efficiency of devices are presented for D2 and P2 in different units: a) EQE and b) power efficiency (left axis) and luminous efficiency (right axis)……………………………….…………83

5.1 Chemical structures of a) block co-polymer (B), b) random co-polymer (R). the hole transport dendron (carbazole) are attached to iridium core and electron transport moieties (oxadiazole) are presented in pink…………………………………………………………………………………….90

5.2 a) device structure, b) energy diagram for different layers. The cathode and transport materials were selected to match the HOMO/LUMO levels of the copolymers. The HOMO and LUMO of TPBi and CBP were taken from literature respectively [16, 17]. The work function for metals was taken from original material sheet provided by CSIRO, the energy level of co-polymers were obtained from PESA measurements as explained in Chapter 2……………………………………91

5.3 normalized absorption and PL spectra for a)block co-polyumer (B), b) random co-polymer (R), c)a zoom in for part of PL spectra of block co-polymer (B), for solution (solid line), neat (dash line), and CBP blend films (dot line) d) a schematic diagram for block and random co-polymers. The pink and black circles are representative for electron (oxadiazole) - and hole-transporting (Ir-carbazole dendrimer) moieties respectively.,……………………………………………………….92

5.1 Lifetime measurements (TSPC) for a) block co-polymer (B), and b) random co-polymer (R) in degassed solution, neat, and CBP blend………………………………………………….………93

5.5 Current density and luminance characteristics for a) block co-polymer (B) with separate distribution of electron- and hole-transporting moieties, b) random co-polymer (R) with random distribution of oxadiazole group to polymer back bone…………………………………………....95

5.2 a) Electroluminescent for three compounds in blends, b) CIE co-ordinates for both co-polymers……………………………………………………………………………………….96

5.7 a) EQE values for block co-polymer (square) and random co-polymer (circle) in neat (black colour) and blend (grey colour), b) power efficiency and luminous efficiency for both compounds97

6.1 a) Schematic LEFET device architecture using asymmetric source and drain contacts; b) Chemical structure for DPP-DTT; c) chemical structure of Super Yellow; d) asymmetric shadow masks inside holder which used for contact deposition……………………………………..102

6.2 a) cryostat set up; b) encapsulated sample on chip with all electrical connections; c) optical images of LEFETs with different channel widths on one substrate……………………….…………103

6.3 Schematic diagram of extraction the contact resistance from devices with different channel lengths…………………………………………………………………………………...104

6.4 Electrical and optical characteristics of a typical LEFET at room temperature: a) source-drain current and brightness for p-mode, VDS was kept constant at -100 V; b) source-drain current in n-mode, VDS was kept constant at +100 V; c) and d) output characteristics for p and n modes, respectively. In all cases the channel length and channel width were 50 um and 16 mm, respectively…………………………………………………………..……………………106

6.5 Operation mechanisms and energy level diagrams for the LEFETs: a) p-mode operation; b) injection for p-mode; c) n-mode operation; d) injection for n-mode……………………..…….107

6.6 Output characteristics at 135 K for (a) Hole; (b) Electron accumulation modes. Channel length and width were 50 µm and 16 mm, respectively……………………………………………..108

6.7 a) Source–drain current at different temperatures for p-mode at VDS=-100 V; b) Source-drain current at different temperatures while VDS was constant at +100 V…………………….…………109

6.8 hole mobility as a function of temperature and gate voltage, and activation energy as a function of gate voltage (channel length and width were 50 um and 16 mm, respectively)………………..110

6.9 a) Contact resistance and channel resistance as a function of gate voltage at two different temperatures; b) intrinsic hole mobility as a function of temperature; c) contact and channel resistances as function of gate voltage for two different temperatures; d) ratio of contact and channel resistances for different gate voltages and temperatures. All plots are for electron accumulation mode. In all cases channel length and width were 50 µm and 16 mm, respectively.111

6.1 Brightness at different temperatures for a) *p*-mode operation; b) *n*-mode operation; EQE at different temperatures for c) *p*-mode operation; d) *n*-mode operation. Note that devices had channel lengths and widths of 50 µm and 16 mm, respectively……………………………………………113

6.2 Photoluminescence Quantum Yield of a thin film of Super Yellow (emissive layer) on fused silica substrates as function of temperature…………………………………………….…………….114

List of Tables

3.1 Summary of PLQY and PL decay values for G1 Ir(ppy)3 in solution, neat film, and CBP blend……………………………………………………………………………………………...52

3.2 A summary of device performance parameters for neat and CBP blend emissive layers……....56

4.1 A summary of PLQY and PL decay values for singly-dendronised compounds in degassed solution, solid state neat and, blend………………………………………………………………68

4.2 A summary of electrical characterization and out-coupling calculations for carbazole dendrimers and poly (dendrimers) in neat and blended devices…………………………………………..…73

4.3 A summary of PLQY and PL decay values for doubly-dendronised compounds in degassed solution and solid states……………………………………………………………………………..78

4.4 A summary of electrical characterization and outcoupling calculations from doubly-dendronised dendrimer and poly(dendrimer) in devices…………………………………………….……………84

5.1 A summary of the photo-physical characteristics for the co-polymer family in solution, neat films, and CBP blends…………………………………………………..……………………..94

5.2 A summary of device performance (left side) and out-coupling values (right side) for devices of both compounds………………………………………………………………………………..98

List of Abbreviations and Symbols

Si	Silicon
Ge	Germanium
CRT	Cathode ray tube
FPD	Flat panel display
LCD	Liquid crystal display
LED	Light emitting diode
FET	Field effect transistor
LEFET	Light emitting field effect transistor
IP	Ionisation potential
EA	Electron affinity
HOMO	Highest occupied molecular orbital
LUMO	Lowest unoccupied molecular orbital
k	Total decay rate
k_R	Radiative decay rate
k_{NR}	Non-radiative decay rate
$I(t)$	Time resolved photoluminescence intensity
I_0	Initial luminescence
EML	Emissive layer
A^+	Hole (cation)
A^-	Electron (anion)
A_0	Ground state
A^*	Product of Coulombically bound electron and hole
HTM	Hole-transporting material
ETM	Electron-transporting material
HTL	Hole-transporting layer
ETL	Electron-transporting layer
EQE	External quantum efficiency
CIE	Commission Internationale de I’Eclairage
NTSC	National television standard committee
HIL	Hole injection layer
EIL	Electron injection layer
HBL	Hole blocking layer

EBL	Electron blocking layer
HIM	Hole injection material
EIM	Electron injection material
PEDOT	Poly(3,4-ethylenedioxythiphene)
ϕ_{EQE}	External quantum efficiency
ϕ_{escape}	Amount of generated photons escaping from the device
$\phi_{capture}$	Fraction of electrons and holes that recombine to form excitons
ϕ_{spin}	Spin statistics
ϕ_{PLQY}	Photoluminescence quantum yield
ITO	Indium tin oxide
SPP	Surface plasmon polariton
p_x	Dipole in x axis
p_y	Dipole in y axis
p_z	Dipole in z axis
OFET	Organic field-effect transistor
L	Channel length
W	Channel width
V_G	Gate voltage
V_{DS}	Source-drain voltage
I_{DS}	Source-drain current
μ	Mobility
c	Dielectric capacitance
V_t	Threshold voltage
μ_D	Drift mobility
μ_0	Trap free mobility
E_t	Activation energy
K_B	Boltzmann’s constant
T	Temperature
PLQY	Photoluminescence quantum yield
COPE	Centre for organic photonics and electronics
DPP-DTT	Diketopyrrolopyrrole–dithienothiophene
CBP	4,4’-N,N’-dicarbazolyl-biphenyl
TPBi	2,2',2''-(1,3,5-Benzinetriyl)-tris(1-phenyl-1-H-benzimidazole)
SY	phenyl-substituted poly(p-phenylenevinylene), super yellow
PL	Photoluminensce
A	Absorbance

PMT	Photomultiplier tube
Q_S	PLQY value of sample
Q_R	PLQY value for reference
A_S	Absorbance of sample
A_R	Absorbance of reference
n_S	Refractive index of sample
n_R	Refractive index of reference
D_S	Sums of corrected photoluminensce for sample
D_R	Sums of corrected photoluminensce for reference
X_{laser}	Intensity of the excitation laser
X_{sample}	Intensity of total emission from sample
X_{sphere}	Photodiode intensity for integrated sphere
R	Reflected excitation power
η	PLQY value
TCSPC	Time correlated single photon counting
VASE	Variable angle spectroscopic ellipsometry
S	Orientation order parameter
K_e	Extraordinary extinction coefficient
K_o	Ordinary extinction coefficient
TM	Transverse magnetic
PEDOT:PSS	Poly(3,4-ethylenedioxythiophene) polystyrene sulfonate
ϕ_{lum}	Luminous flux
$EL(\lambda)$	Radiation intensity
$ER(\lambda)$	Eye response
P_{out}	Optical power
n_{ph}	Number of photons
n_e	Number of electrons
X	Tristimulus x value
Y	Tristimulus y value
Z	Tristimulus z value
$x(\lambda)$	Colour matching function representing red light
$y(\lambda)$	Colour matching function representing green light
$z(\lambda)$	Colour matching function representing blue light
J	Current density
η^*	Power efficiency
MLCT	Metal to ligand charge transfer

EL	Electroluminescence
ROMP	Ring opening metathesis polymerisation
SCLC	Space charge limited current
Photo-CELIV	Photo-charge extraction in linearly increasing voltage
LPCVD	Low pressure physical vapor deposition
PMMA	Poly (methylmethacrylate)
R_t	Total resistance
R_{ch}	Channel resistance
R_c	Contact resistance

Chapter 1
Introduction

1.1 Motivation

Over the last seventy years, an inorganic family of semiconductors, mainly consisting of silicon (Si) and germanium (Ge) has revolutionized all aspects of our lives through electronics. Products of a multi-billion US dollar industry have filled our everyday life: from personal mobile phones and computers, to satellites, solar energy panels, and the worldwide internet. A key part of this industry is transmitting the electronic information to human visual understanding through “display technology”. This sector of technology is likely to be the most rapidly expanding market in coming years as it has so many use in different electronic devices [1].

Cathode ray tube (CRT) displays dominated the market for a long time and employ the thermionic emission principle, which required use of high voltages and vacuum. CRT displays were therefore heavy and bulky because of weight and size of the required components. In spite of a number of effective and innovative changes in CRTs, they have been replaced by flat-panel displays (FPDs) such as liquid crystal displays (LCDs) and plasma displays. Plasma displays on the other hand provide high quality pictures over wide viewing angles. However in comparison with CRT and LCD displays they have shorter display lifetimes [2].

Light emitting diodes (LEDs) are another member of the flat-panel display family, which operate by direct conversion of electrical energy to visible light in semiconductors. LEDs normally have long operational lifetimes due to utilising solid state semiconductors, which are electrochemically more stable.

Lately, more research has focused on LEDs manufactured from organic semiconductors called OLEDs. Organic semiconductors exhibit many novel physical, electrical and optical properties. These properties include the potential for large-area solution processing, compact size of the functional layers, flexibility, and almost unlimited possibilities with respect to molecular design, that are not typically available to conventional inorganic semiconductors (e.g Ge, Si). These novel properties of organic semiconductors have generated new opportunities not only for display technology but solar cells, sensors, detectors, and field effect transistors (FETs).

Figure 1.1 A next generation iWatch, which will have a 1.3-1.5 inch flexible OLED-display [3]

OLEDs provide colour vibrancy, high colour contrast ratio, excellent power efficiency and a range of fabrication conditions making them suitable for flexible substrates, ultrathin displays, and smartphones (see Figure 1.1) [4-6]. Beyond these applications, white light emitting OLEDs are attracting attention in the lighting market due to their higher efficiency and performance in comparison with their inorganic counterparts and fluorescent tubes [7, 8], and new product design and lighting opportunities due to the unique processability of organic semiconductors [9].

OLED displays still require transistor-based backplane circuits to switch their elements. The cost of this FET panel circuitry is more expensive than the OLED itself. However, The electroluminescence properties of OLEDs can be combined with the switching properties of transistors in a single architecture to produce a class of devices called light emitting field effect transistors (LEFETs) [10]. The dual functionality of LEFETs provides the potential for new applications such as simplified pixels for flat panel displays [11], LEFETs can tolerate higher current densities than OLEDs and also in some cases can transfer the emission zone from underneath the metal electrodes [12, 13]. Furthermore, LEFETs are convenient tools for studying fundamental charge transport and photo-physical processes in organic semiconducting materials and this will be explored in the work presented in this thesis.

Although remarkable steps have so far been taken towards understanding the behaviour of organic semiconductors, a number of fundamental issues remain unknown. Also, some additional device and manufacturing related challenges are: avoiding complex device structure with more than three layers; solution processibility; host free materials with high photoluminescence suitable for single layer devices; low operation voltage; and increasing out-coupling using novel concepts such as molecular alignment. Therefore, progress in the OLED industry demands new material developments and device architectures with promising photo-physical and electrical properties. However, controlling the charge transport and emissive properties of OLED materials remains a key research area due to the complicated nature of their disordered structure, which also can be affected by processing condition [14-22]. All of these considerations motivated the work that is described in this thesis, which focuses on the understanding of phosphorescent OLED materials.

1.2 Properties of organic semiconductors

Organic semiconductors are based on carbon chains. Isolated carbon atoms have a ground state electronic configuration of $1s^2 2s^2 2p^2$ and they can act as conductive materials through orbital hybridisation in the bonding configuration. Organic semiconductors have a conjugated π-electron system formed by overlapping P orbitals of sp^2-hybridised carbon atoms within the molecules [23]. In this configuration each carbon atom has three sp^2 orbitals, two bonded to the neighbouring carbon atoms in the carbon chain and the third to a hydrogen atom or another carbon atom. The fourth valence electron resides in a p-orbital and may become delocalised along the carbon chain by overlap of p-orbitals to form a chain of π-orbitals. The p-orbitals can overlap either in phase or out of phase to form bonding (π) or antibonding (π*) molecular orbitals respectively [24]. The π-bonding is weaker than the σ-bonding framework forming the backbone of the molecule due to poorer orbital overlap. Therefore, the π-π^* transitions in conjugated molecules are typically the lowest energy electronic excitation with energy gaps of between 1.5 and 3 eV. This allows absorption and emission of light in the visible spectral range (see Figure 1.2) and the energy gap can be controlled by the degree of conjugation in the organic semiconductor. Therefore the optoelectronic properties can be tuned by molecular engineering [25].

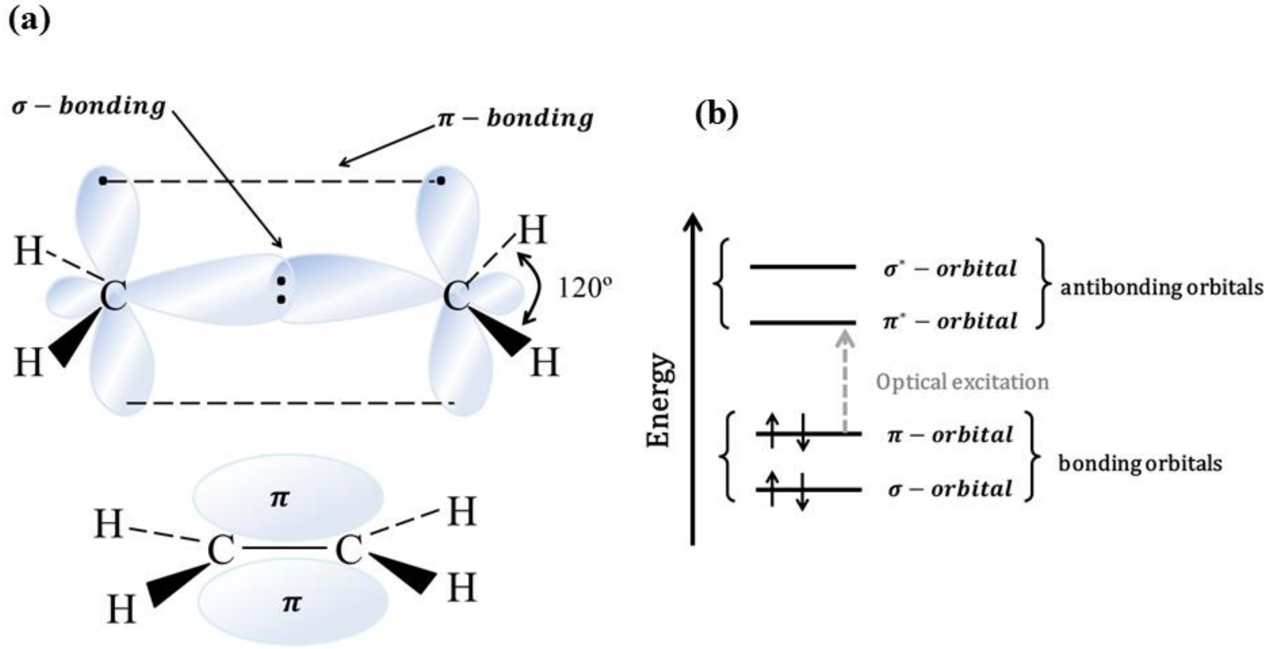

Figure 1.2 a) The bonding system of ethene showing the σ- and π-bonds, b) the corresponding energy level diagram of ethene. The lowest energy electronic excitation shown is between the bonding π-orbital and the antibonding π*-orbital, adapted from [25].

1.2.1 Energy levels and nomenclature

When an electron is removed from a molecule, it creates an ionised molecule with a new set of energy levels. The energy difference between the original molecule and its ionised state is known as the ionisation potential (IP). Conversely, when an electron is added, a new molecule with an additional electron results. The energy difference between the original molecule and the one with an extra electron is called the electron affinity (EA). In the organic semiconductor research field the IP and EA are often used interchangeably with highest occupied molecular orbitals (HOMO) and lowest unoccupied molecular orbitals (LUMO), respectively. This is not a completely accurate nomenclature but justified with certain assumptions. The electrons reside in the molecular orbitals in order of increasing energy. HOMO refers to the orbital containing the highest energy electrons and LUMO is the lowest energy unoccupied orbital. The HOMO and the LUMO are analogous to the valance band and the conduction bands in inorganic semiconductors, respectively. The charge transport properties of a neutral molecule depend on the electron density distribution in these orbitals. For efficient *p*-type charge transport, holes are injected into the HOMO and it is desirable for the HOMO to be delocalised. The case is similar for *n*-type charge transport where electrons are injected into the LUMO. Nevertheless, lack of orbital overlap with neighbouring molecules generates a potential barrier between molecules, which leads to charge carriers being trapped on a molecule and poorer charge transport overall.

1.3 Dendrimers

Traditionally, organic semiconductors have been divided to the two main classes of small molecules and polymers. Small molecules are attractive due to their simple, well-defined molecular structure and their mono-dispersity. However, not all of them are soluble and are typically deposited through high vacuum and thermal evaporation techniques [26-30]. On the other hand, polymers are generally processed from solution via spin-coating and inkjet printing. This is a promising feature for fast, large area, and low temperature mass production in display technology. Although solution processing of polymers is less wasteful than evaporation with patterning, the reproducibility of polymer synthesis in terms of the polydispersity (a measure of the distribution of molecular mass in a given polymer sample), molecular weight, and backbone defects is difficult to control [31-34].

The work presented in this thesis is mainly focused on an emerging class of organic semiconductor materials known as dendrimers. These are branched macromolecules consisting of three components as shown in Figure 1.3: a core, branching units known as dendrons, and surface groups [31-36]. The core is usually the chromophore unit responsible for optical properties such as the colour of the emitted light, and it also contributes to the three dimensional structure of dendrimer. The dendrons control the intermolecular interactions between the cores, they can be either electroactive [37, 38] or electrically insulating, and play a role in determining the molecular structure [39]. Branching dendrons play a similar role as the host material in a blended system which will be discussed later in this chapter. The surface groups control the interaction with the environment surrounding the dendrimer and thereby the solubility of the dendrimer.

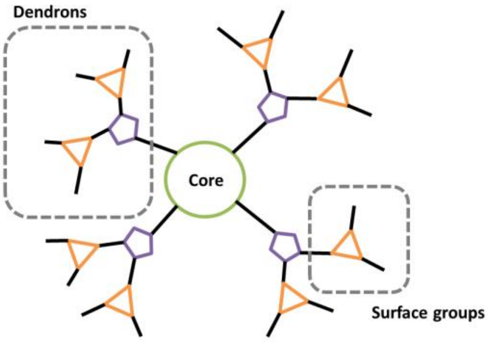

Figure 1.3 A schematic diagram of the first generation of a dendritic structure consisting of a core, branching units and surface groups.

A particular advantage of dendrimer molecules is that the dendron and the core can be made electrically independent, meaning that the type of dendron attached to the core will have no effect on the electronic properties of the core. Consequently, the electronic properties of dendrimers can be defined in three different ways by dendrons [40]; the type and the number of the dendrons attached; and the number of branching levels from the core known as the dendrimer generation. Therefore, careful dendrimer design of the dendrons can yield efficient charge transport with no influence on the other properties such as emission colour and solubility [21, 41]. Dendrimers can therefore be designed to be ink-jet or screen printed by choosing appropriate surface groups [42].

Dendrimers are seen as promising candidates for OLED technology as they incorporate the advantages of small molecules and conjugated polymers. A new promising approach for OLED materials are poly(dendrimer)s. Polymers with pendant side-chain chromophore cores encapsulated by dendrons, which combine the advantages of dendrimers in reducing the quenching of the emitter with the viscosities of polymers.

1.4 Luminescence and electroluminescence

When a photon is absorbed by any organic materials, an electron is promoted from the ground state (S_0) to a higher energy level represented by S_1 and S_2 in Figure 1.4. The excited state will then decay back to ground state either directly by emitting a photon or through vibrational relaxation after internal conversion. Internal conversion is the non-radiative transfer of energy between excited states occurring on the order of femtoseconds (fs) [43-45].

An exciton is formed from the excitation of an electron to a higher energy level as organic semiconductors typically have low dielectric constants at room temperature. The exciton is a Coulombically bound state of the electron and the hole with binding energies of 0.5-1.0 eV in the ground state [58-61]. The bound electron and hole can have four possible permutations of their spin states; one is anti-symmetric with a total spin of 0 called the singlet state, and the other three orientations have a total spin of 1 and are called triplet states (see Figure 1.4). Singlet-singlet and triplet-triplet transitions occur by spin conservation. Since the ground state typically has filled energy levels, the molecules typically have singlet ground states, and therefore excitation to the triplet state is not allowed according to spin selection rules. Fluorescence occurs when singlet excitons relax back to a singlet ground state and these transitions occur very quickly with typical lifetimes of less than 1 ns [46].

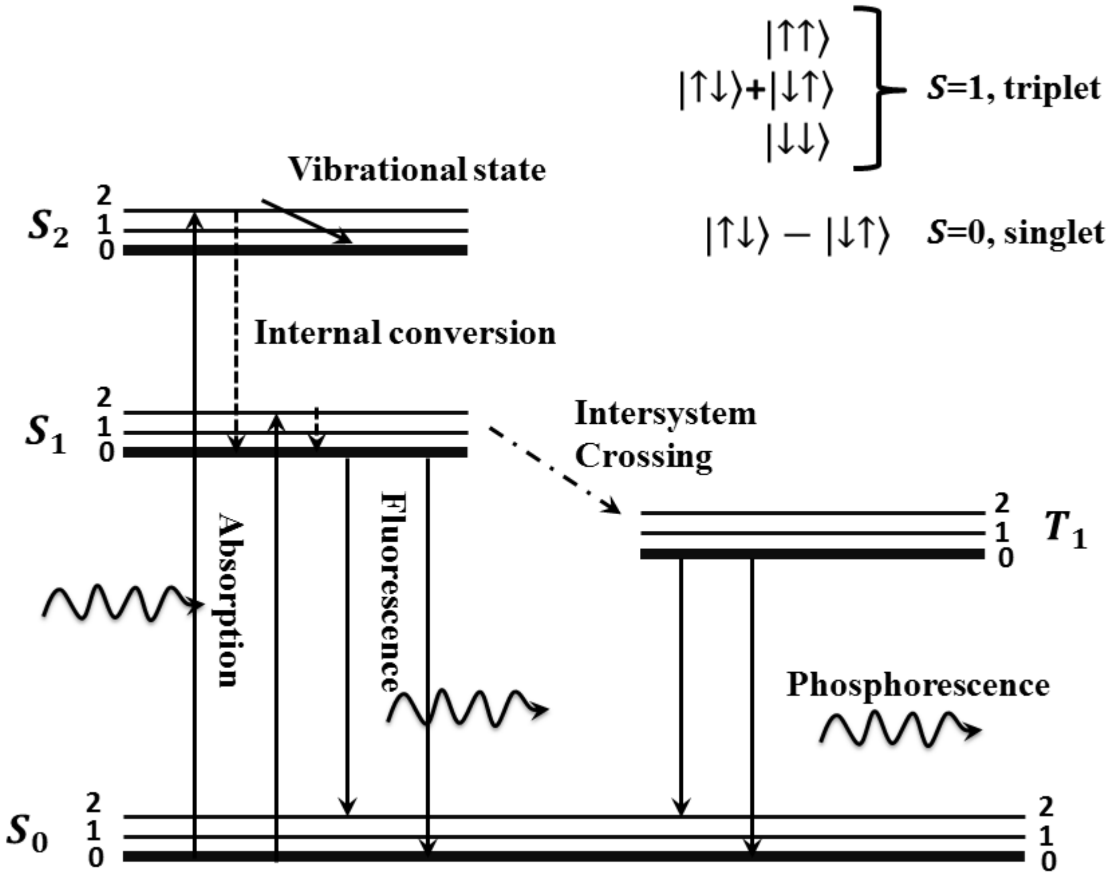

Figure 1.4 A Jablonski diagram illustrating the possible relaxation pathways in the singlet and triplet manifolds.

Triplet states may be occupied as a result of non-radiative intersystem crossing from excited singlet states. Since the radiative decay from the triplet state to the singlet ground state is spin forbidden, the triplet states are long lived. However, the probability of intersystem crossing can be boosted by mixing of the triplet state with the singlet state prior to the emission by the addition of the heavy atom effect [47-49]. Heavy metals such as iridium and platinum induce strong-spin orbit coupling, which allows the triplet state to decay radiatively to the singlet ground state. Such emission from the triplet states is known as phosphorescence which has a lifetime on the order of μs-ms [50-53].

In electroluminescence, electrons and holes are directly injected into a luminescent organic semiconductor, which create excitons as per the description above. In this case, for every three triplet excitons, only one singlet exciton is generated, meaning that the internal quantum efficiency of fluorescent materials will be limited to 25% [54-57]. However, phosphorescent materials benefit from being able to harvest both singlet and triplet excitons, which allows internal quantum efficiencies of 100% [58, 59].

For any luminescent material, the total decay rate $k$is equal to:

$$k = k_R + k_{NR} \tag{1.1}$$

Where k_R is the radiative decay rate and k_{NR} is the non-radiative decay rate. The total decay rate k can be measured from time-resolved measurements of the photoluminescence by fitting the exponential decay with

$$I(t) = I_0 e^{-kt} \tag{1.2}$$

Where $I(t)$ is the time resolved photoluminescence intensity, I_0 is the initial photoluminescence intensity. The radiative rates are much faster in fluorescent materials due to their faster photoluminescence (PL) decay. To be able to distinguish the distribution of radiative and non-radiative decay rates, it is necessary to measure the photoluminescence quantum yield (PLQY) of a material [46, 60]. This is obtained by measuring the ratio of the number of photons emitted to the number of photons absorbed, which is related to the non-radiative k_{NR} and radiative k_R rates by [61]

$$PLQY = \frac{photons\ emitted}{photons\ absorbed} = \frac{k_R}{k_R + k_{NR}} \tag{1.3}$$

1.5 Organic light emitting diodes

An OLED is an electronic device that emits light in response to an applied potential [62]. OLED devices consist of a substrate and either an emissive layer (EML), or more complex (EML, electron-transporting, and hole-transporting) layered stacks of organic materials sandwiched between two electrodes (see Figure 1.5. a).

1.5.1 Operating mechanism, parameters, and performance metrics

Electrons and holes are injected into the organic layer from cathode and anode, respectively, when a potential is applied [62]. Under the influence of the applied electric field [26, 63], opposite charges can move toward each other leading to possible recombination (see Figure 1. 5. b) which is describe by:

$$A^+ + A^- = A_0 + A^* \tag{1.4}$$

Where A^{+} and A^{-} indicate holes (cations) and electrons (anions), respectively, A_0 represents the ground state, and A^{*} is a molecule in an excited state. While A^{+} and A^{-} can be from different materials A^{*} is the product of a Coulombically bound electron and a hole, which can radiatively decay back to the ground state by emitting light or through non-radiative intersystem crossing to another excited state [62]. Therefore, the process of light emission in OLEDs can be summarised in four key steps: charge injection, charge transport, recombination, and radiative decay.

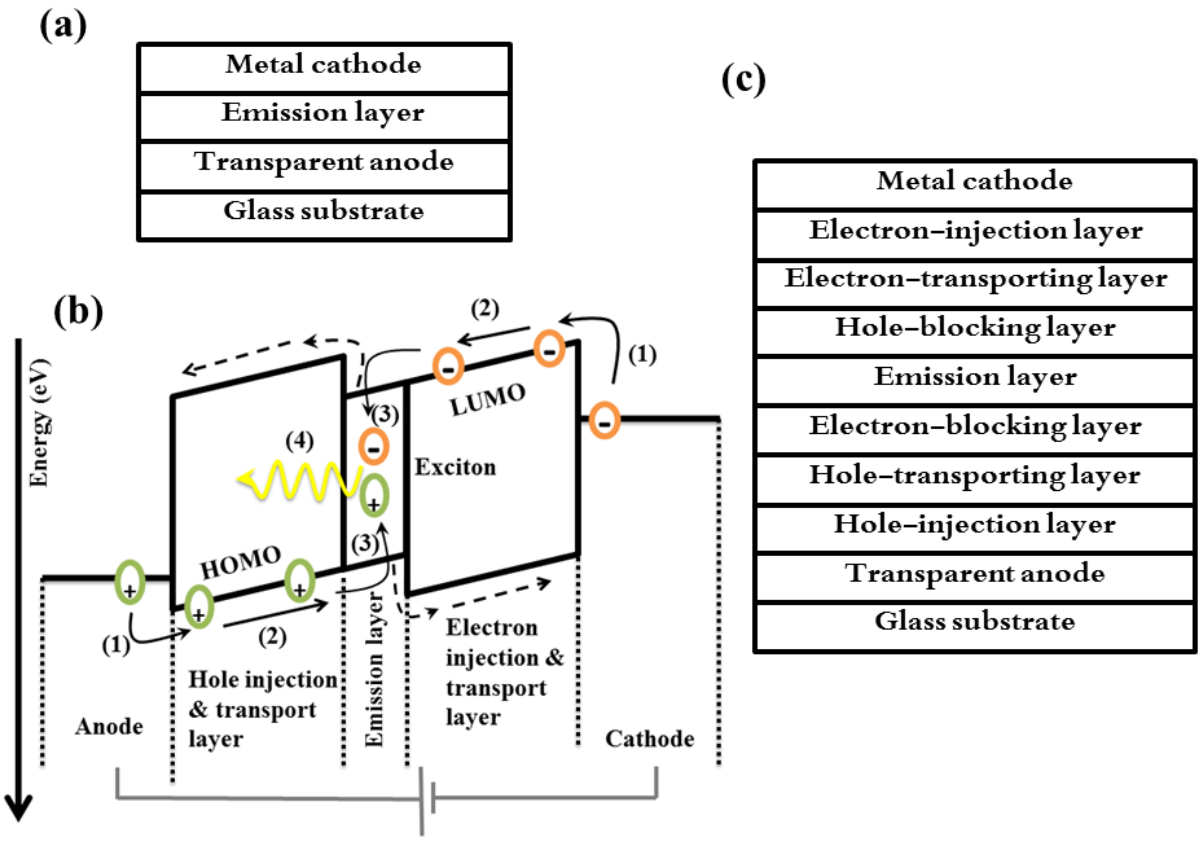

Figure 1.5 OLED device structure, a) an OLED comprising a single active layer, b) a schematic mechanism of OLED operation illustrating the basic processes of electroluminescence. Holes are injected from the anode into the HOMO of the hole injection layer and pass to the hole transport layer. Electrons are injected from the cathode into the LUMO of the electron injection layer EIL and pass to the electron transport layer. Excitons are formed in the emissive layer and emission will occur, c) a multilayer OLED.

Hole-transporting materials (HTMs) have relatively low ionization potentials (IPs) [64], which is the energy required to remove an electron from the HOMO. IPs can be obtained from electrochemical oxidation potentials in solution or measured by photoelectron spectroscopy. Moreover, it is beneficial for HTMs to have sufficiently high hole drift mobility [62]. Likewise electron-transporting materials (ETMs) should have high electron drift mobility and a suitable EA.

The EA is the negative of the energy released when an atom or a molecule (X) acquires an electron to form the negative ion (X^-) [62]. EAs can be obtained from the correlation of laser photo-electron spectroscopy results with the LUMO energy levels.

The performance of OLED devices is typically described by four metrics: drive voltage, efficiency, lifetime, and colour [62], which are defined as follows:

Drive voltage – also referred to as the turn on voltage, is the voltage that must be applied in order to have an emission intensity of 1 cd/m^2. This voltage is affected by a variety of factors: the built in potential between electrodes; energetic barriers to charge injection; and the electric field which is required for migration of charge carriers through the device [62]. Therefore, in a well-optimised device, the turn on voltage will approach the energy of the emitted photons [65]. Moreover, the turn on voltage can be reduced by careful selection of the EML, electron transport layer (ETL), and hole transport layer (HTL) materials so that the energy barriers for charge injection from the transport layer into the EML are minimised [62].

Efficiency – is defined as the ratio of output light energy to the energy input or electrical energy expended [66]. This can be represented by a variety of metrics: external quantum efficiency (EQE), current efficiency (cd/A), and power efficiency (lm/W), which will be described in the next chapter.

Lifetime – sometimes referred to as potential stability, is defined as the number of hours required for the photo-intensity of the device to drop to half of its initial value at a given current density. Device failure occurs for several reasons: the degradation of the interface between the metallic electrodes and the organic layers; chemical reactions from current flow; internal heating of device at high current densities; and changes in the film morphology of the organic layers [62]. Testing current densities are typically around 80 mA/cm^2 or the current required to generate 1000 cd/m^2 photo-intensity. Lifetime and current density are related with an inverse exponential, therefore doubling current density leads to a drop factor of 3-4 in lifetime [62].

Colour – is defined according to the 1931 International Commission for Illumination (Commission Internationale de I'Eclairage) $CIE_{x,y}$ values [67]. The entire emission spectrum of a device is reduced to two numbers which describe the colour as perceived by the human eye. According to the National Television Standard Committee (NTSC), the CIE co-ordinates are (0.14, 0.08) for blue, (0.21, 0.71) for green, (0.67, 0.33) for red, and approximately (0.33, 0.33) for white [62].

There are other additional performance metrics that can affect one or more of the parameters above such as increasing drive voltage, power consumption, and change in emission colour with age of the device. Different techniques to optimize the performance metrics of devices include [62]:

- Introducing additional functional layers to the device (see Figure 1.5. c) such as: hole injection layers (HILs); electron injection layers (EILs); hole blocking layers (HBLs); and electron blocking layers (EBLs). HIL and EIL improve the injection of holes and electrons, respectively, into the transporting layers. The blocking layers can also provide more efficient recombination by confining the electrons and holes in the EML.
- Introducing an ETL comprising multiple layers with different LUMO levels to decrease the drive voltage, and increase the lifetime and efficiency [68].
- Increasing the work function of indium tin oxide (ITO), the most commonly used transparent anode, in order to reduce the injection barrier and consequently the drive voltage. Various surface treatments produce this effect such as oxygen (O_2) plasma treatment [69], UV/ozone treatment [70], CF_4/O_2 plasma treatment [71], and treatment with polymerization of CHF_3 [72].
- Device stability and efficiency can be improved by the introduction of various hole injection materials (HIMs) between anode and HTL [73-75]. This would ease the injection of holes into the HTL. The most common HIM is poly(3,4-ethylenedioxythiphene) (PEDOT) [76], which is used in the work presented in this thesis.
- Charge injection from reactive cathodes such as aluminium to the ETL can be improved by utilising reactive low work function electron injection materials (EIMs) such as lithium fluoride and lithium oxide [72, 77].
- Introducing host materials into the EML to provide higher recombination rates and reduce the quenching rate by the dopant (guest) molecules. Host materials need to meet several requirements such as lower barriers for charge injection, good transport for both electrons and holes, a wider gap between their HOMO and LUMO than the dopant, and slower non-radiative decay rates than the time required for energy transfer to the dopant. In order to meet all of these requirements multiple materials may be used as a mixed host.

The performance metrics of OLED devices such as drive voltage, lifetime, efficiency, and colour are controlled by complex interactions between different layers in a device. Whilst the development of new materials for each of these layers is therefore crucial, the interplay between the properties of these new materials that leads to efficient devices should be borne in mind.

1.5.2 Loss mechanism and dipole orientation in OLEDs

The external quantum efficiency of an OLED is given by

$$\phi_{\mathrm{EQE}} = \phi_{\mathrm{escape}} \times \phi_{\mathrm{capture}} \times \phi_{\mathrm{spin}} \times \phi_{\mathrm{PLQY}} * 100\% \qquad (1.5)$$

where ϕ_{spin} is related to the spin statistics for the formation of singlet or triplet excitons, ϕ_{PLQY} is the photoluminescence quantum yield as defined in equation 1.3, $\phi_{capture}$ is the fraction of electrons and holes that recombine to form excitons, and ϕ_{escape} is the amount of the generated photons that escape from the device. The EQE can be improved by influencing any of these parameters. Utilising phosphorescent heavy metal complexes like iridium, which provide harvesting from both singlet and triplet states leads to ϕ_{PLQY} and ϕ_{spin} values near unity [48, 49, 78]. Moreover introducing charge injection and blocking layers can confine the recombination zone to a narrow layer and this increases $\phi_{capture}$ by promoting the recombination of all charge carriers [79].

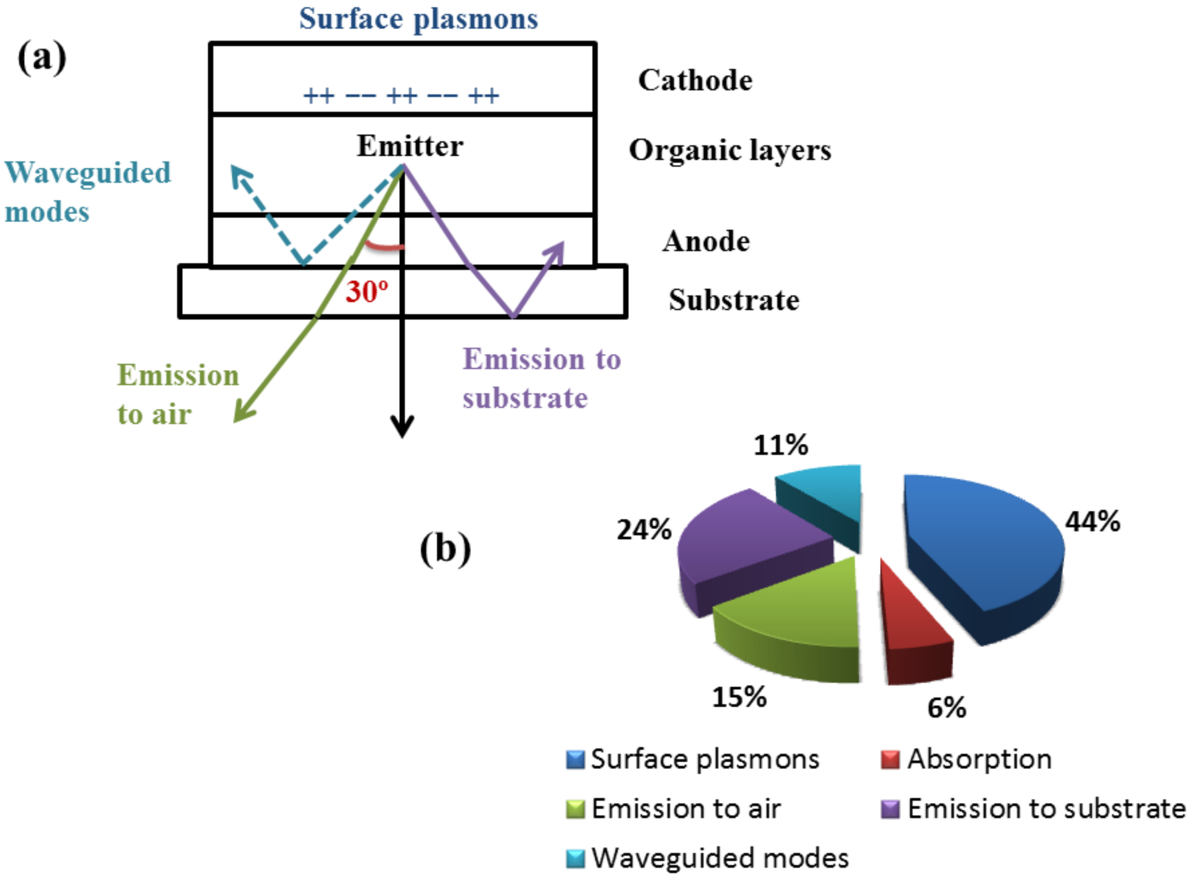

Figure 1.6. a) Schematic illustration of loss mechanisms in an OLED. With no out-coupling enhancement only a small amount of emission escapes to be observed, b) the distribution of different optical losses for a comparable fluorescent or phosphorescent emitters with similar stack layer thickness, refractive indices and emission spectra.

However, only a relatively small proportion of the light generated escapes from the OLED stack. The light generated inside such a thin film structure can couple to different optical channels (see Figure 1.6. a). The light escape cone has a 30° opening with respect to the surface normal, as viewed from the emitter position, and this typically contains only 20% of the total number of photons [80, 81]. At higher emission angles, the light cannot even reach the glass substrate as it will be reflected back by the other organic layers and the transparent ITO electrode before finally being lost by re-absorption or emission at the edge of the device [81]. The light generated can also couple to surface plasmon polaritons (SPPs), infrared- or visible-frequency electromagnetic waves traveling along a metal-dielectric or metal-air interface. *The term "surface plasmon polariton" explains that the wave involves both charge motion in the metal ("surface plasmon") and electromagnetic waves in the air or dielectric ("polariton")* [82, 83]. In typical planar OLED stacks around 60% of the light is trapped in plasmon and waveguided modes within the device [84-86]. Figure 1.6 b) shows the contribution of different optical losses for the fluorescent emitter Alq_3 and these losses would be similar for any fluorescent or phosphorescent emitter with comparable stack layer thicknesses, refractive indices and emission spectra [81].

Different approaches to improve out-coupling have been reported including high refractive index substrates [8, 88], grating-assisted out-coupling [89-91] and many others [81, 92]. An alternative strategy is to intrinsically increase the out-coupling by controlling the direction of light emission. This utilises the fact that light is emitted perpendicular to the dipole transition moment vector of the organometallic molecules at the centre of these devices [93, 94]. Orientation of the transition dipoles parallel to the substrate eliminates the need for gratings, micro-lens arrays, or any other physical methods used to enhance out-coupling [4, 8, 88, 93, 95, 96]. Moreover, this strategy avoids the excitation of surface plasmons even when the emitter is close to the metallic electrode [81].

To have horizontally oriented dipoles, the emitter molecules must have anisotropic orientations. Some materials have intrinsically rod-like chromophores with large shape anisotropy [97]. This effect has been well known for polymeric OLEDs [98, 99], fluorescent emitters [97, 100], and even phosphorescent emitters doped in isotropic materials [101]. The orientation depends on the anisotropic property of the host or dopant in an emissive layer and also the packing within such host-guest systems [102-104].

Amorphous organic semiconductor films cannot be analysed by X-ray diffraction measurements as they do not have a long-range periodic structure. However, there are some methods which quantitatively estimate the degree of molecular orientation in amorphous organic films including: variable angle spectroscopic ellipsometry [93]; absorption spectra from randomization of molecular orientation induced by heating [105]; and angular dependent PL spectrum measurements [81, 106, 107]. The last method was used in the work presented in this thesis.

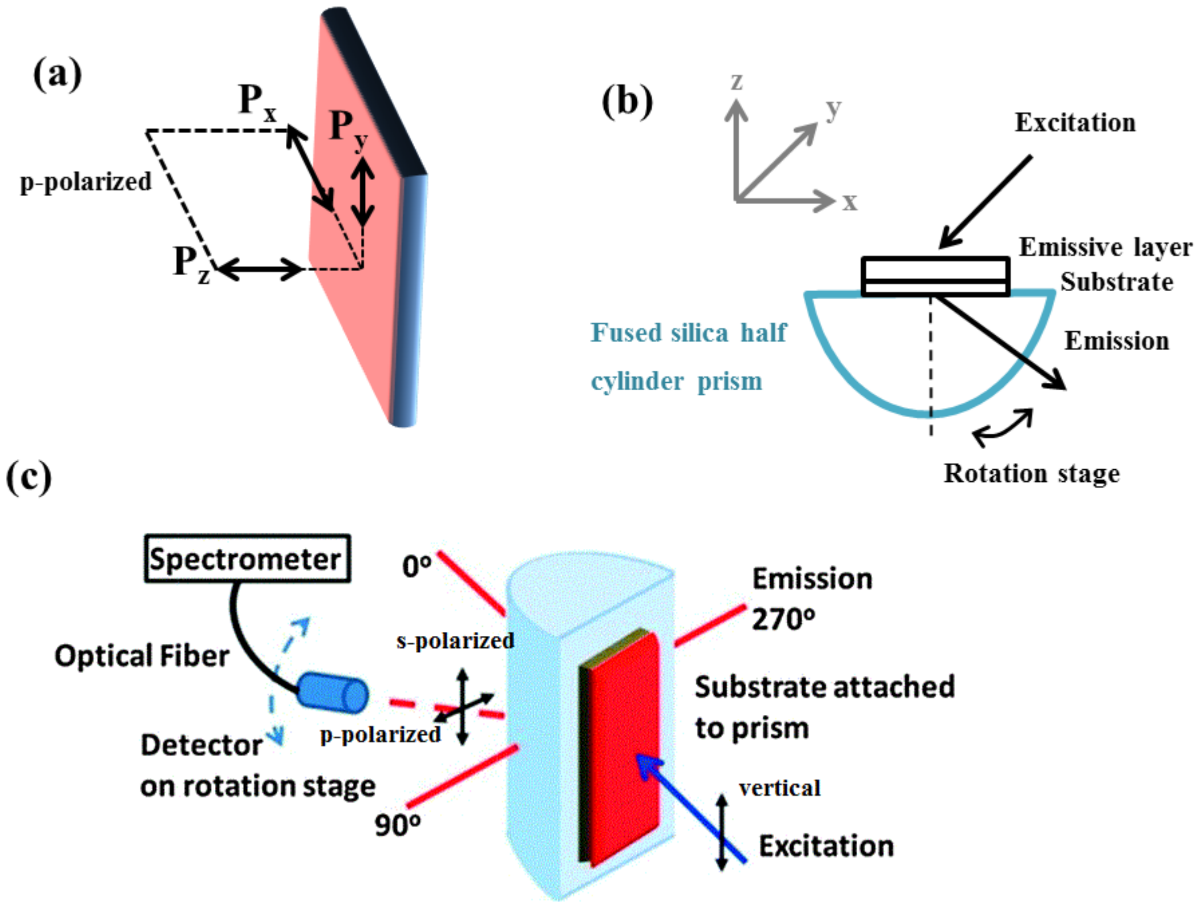

Figure 1. 7 a) The conventional definition for dipole orientation, b) A cross-sectional schematic view of the angular dependent PL spectrum set up , c) A schematic diagram of the experimental setup with angle notations and emission polarizer orientations for recording s- and p- polarized emission, adapted from [87].

Figures 1.7 a) and b) illustrate the co-ordinate system and an outline of the angle dependent PL measurement apparatus. Isotropic materials with random transition dipole orientations are treated as a superposition of p_x-, p_y-, and p_z- dipoles with each contributing a third of the emitted intensity. For a perfectly isotropic material the ratio of perpendicular (p_z) and parallel (p_x- and p_y-) polarised waves is therefore 33:67, while the horizontally oriented dipoles consist of equal proportions of p_x- and p_y-dipoles [107]. Given that the dipoles radiate strongest perpendicular to their oscillation direction, the p_z-dipoles emit mainly at large angles between 0° to 180° (see Figure 1.7 c). Emission from p_z-dipoles leads to loss in plasmons and waveguided modes, therefore out coupling efficiency can be increased by converting vertical dipoles to horizontal dipoles. To obtain information about the ratio of horizontal and vertical dipoles the p-polarized emission in the x-z plane is measured. The *p*-polarized plane is parallel to the detector (or incident) plane, which is perpendicular to the substrate. The p_y-dipoles have no component in the *p*-polarized emission due to the fact that they are vertical in the detector plane. Taking into account that p_x-dipoles emit between 90° to 270° in the detector plane, measuring the p-polarized emission consequently yields information about the existence of vertical emission. The experimental technique of angular dependent PL spectrum measurements will be detailed in the next chapter.

1.6 Organic light emitting field effect transistors

An organic field-effect transistor is a three terminal device with switching properties comprising gate, source and drain electrodes, with dielectric and semiconductor layers sandwiched in between. When the switching properties of an OFET were combined with the electroluminescent properties of an OLED in a single device architecture, a new family of devices was established called light emitting field effect transistors [10]. The structure of a LEFET is the same as an OFET except that the semiconductor layer is electroluminescent. This can be achieved by using either a single layer, or multi-layer LEFET architectures with more than one semiconductor layer (see Figure 1.8).

1.6.1 Operating mechanism, parameters, and performance metrices

The two important architectural parameters in a LEFET are the channel length (L, the distance between source and drain electrodes) and the channel width (W, the length of the source or drain electrodes). LEFETs can be operated in three different modes depending on the type of charge transport occurring in the device: i) unipolar *p*-type in which transport is dominated by holes; ii) unipolar *n*-type in which transport is dominated by electrons; and iii) ambipolar mode in which both electrons and holes can accumulate and be transported within the semiconducting channel of the device [108].

The basic operating mechanism of LEFETs is based on that of OFETs, where charges are accumulated at the semiconductor/dielectric interface in order to switch the device ON. This is referred to as accumulation mode because most organic semiconductors are intrinsically undoped in contrast to inorganic semiconductors that can be extrinsically doped [23].

In the case of the unipolar *p*-type mode (see Figure 1.7. a), the application of negative gate voltage (V_G) polarises the dielectric, which builds a capacitance and leads to the accumulation of positive charge carriers (holes) at the semiconductor/dielectric interface. The application of a negative voltage between the source and drain electrodes (V_{DS}) injects electrons and more holes into the LUMO and HOMO of the semiconductor layer, respectively. The injected holes accumulate at the interface between the semiconductor and dielectric and the increase in positive charge carriers increases the charge carrier density at the interface to produce a conducting channel inside the semiconductor.

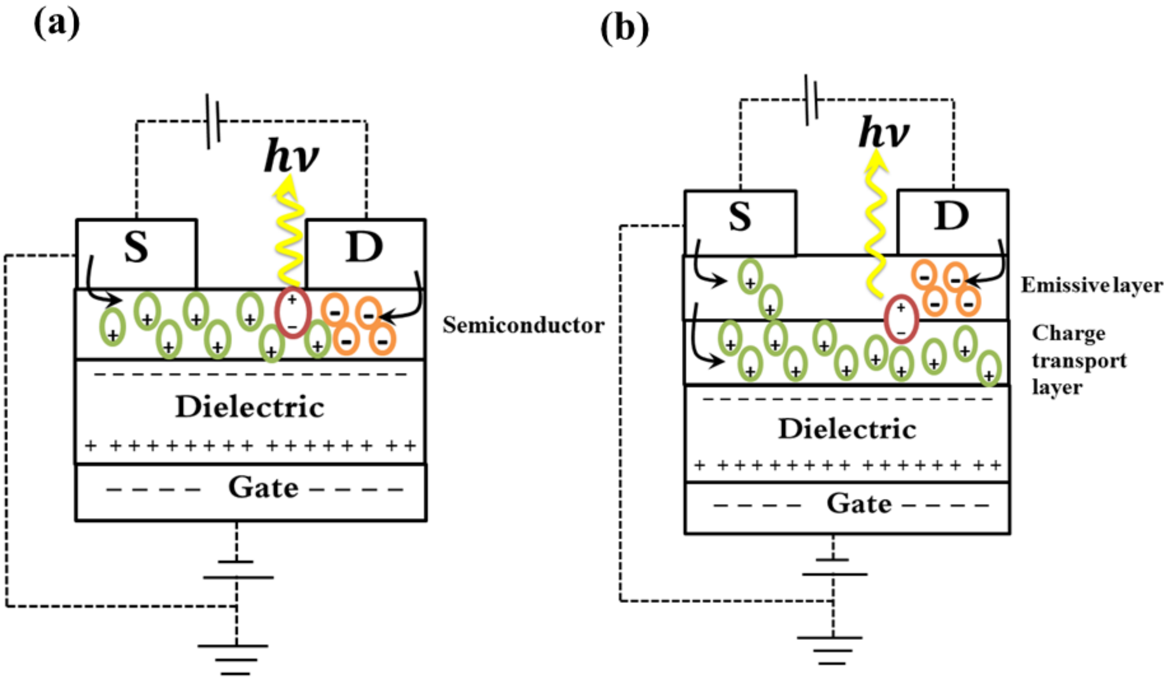

Figure 1.8 Schematic diagrams including the p-type operating mechanisms of a) a single layer LEFET and b) a multi-layer LEFET.

The current between the source and drain electrodes (I_{DS}) increases when the transistor is switched ON. Holes and electrons that are injected by the source and drain electrodes can recombine during device operation and light is consequently emitted from the channel. Although in a unipolar LEFET just one type of charge carrier accumulates within the channel, both charge carriers need to be injected in order for light emission to occur. These criteria can be achieved using either a single layer, where charge transport and recombination occur in the same layer, or multi-layer LEFET architectures, in which charge transport and recombination occur in separate layers (see Figure 1.8 b). Operation in an *n*-type LEFET is the same as in a *p*-type LEFET except that the applied voltages are positive and electrons are the dominant charge carriers.

In case of an ambipolar LEFET, both charge carriers can be transported in the channel depending on the polarity of the applied voltage [109]. The source and drain electrodes can be symmetric or asymmetric (comprised of high and low work function electrodes) depending on the semiconductor layer. There are also different operating regimes of a single layer ambipolar LEFET, which are detailed as follows:

- ***Electron-dominated regime*** – electrons are the dominant charge transport carrier within the transistor channel with a large positive applied gate voltage. Holes are injected into the semiconductor layer and remain in the vicinity of the hole-injecting contact. As more electrons accumulate at the interface, they recombine with holes near the hole-injecting contact to emit light [110]. The source-drain current and consequently the brightness of the device are consequently high.
- ***Ambipolar regime*** – as the gate voltage approaches zero and toward negative direction, the accumulation of electrons decreases and begins to be replaced partly by the holes. Holes and electrons are therefore both accumulated throughout the channel and their currents are more balanced. Light emission will occur in the middle of the transistor channel and with lower intensity than in the single-charge dominated regimes [23, 111].
- ***Hole-dominated regime*** – when the gate voltage becomes large and negative, holes accumulate the channel. At the same time electrons are injected into device and remain in the vicinity of the electron-injecting contact. Holes recombine with electrons close to the electron-injecting contact and produce a high brightness as was the case in the electron-dominated regime [110].

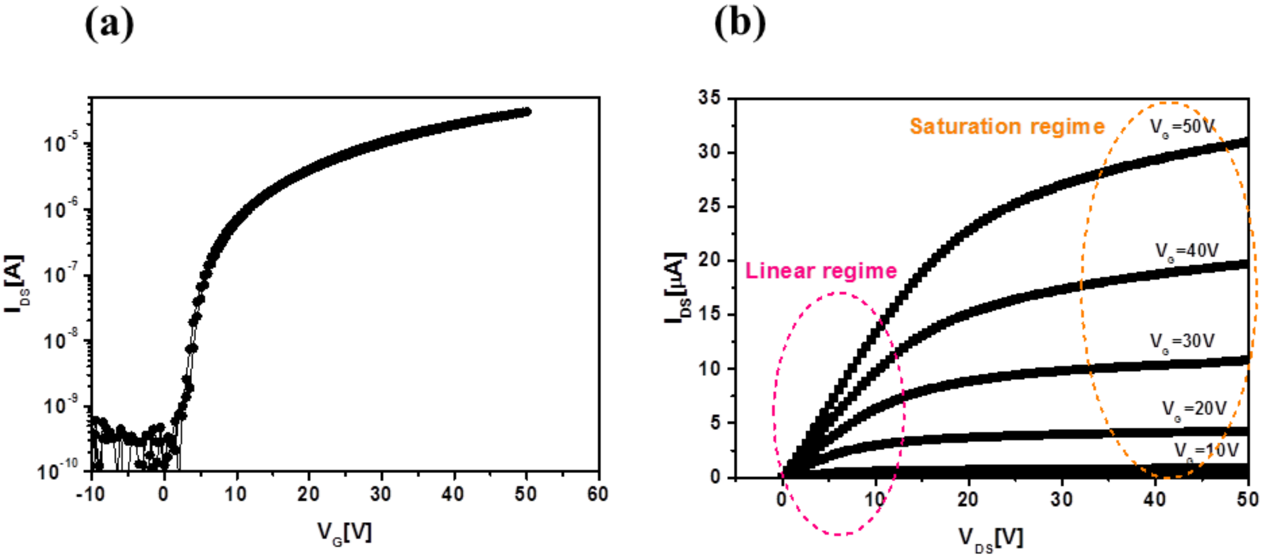

Figure 1.9 a) Transfer characteristics of a *n*-type LEFET showing the source-drain current (I_{DS}) as a function of the applied gate voltage (V_G) with a fixed source-drain voltage (V_{DS}). b) The output characteristics of the LEFET showing the I_{DS} as a function of V_{DS} for different values of V_G.

The transfer characteristics of a LEFET device are represented by the source-drain current (I_{DS}) as a function of the applied gate voltage (V_G) while the source-drain voltage (V_{DS}) is fixed (see Figure 1.9. a). The output characteristics of the transistor are given by the I_{DS} as a function of the V_{DS} at a constant V_G. The output characteristics comprise linear and saturation regimes (see Figure 1.9. b). The source-drain current of transfer characteristics in the saturation regime is

$$I_{DS} = \frac{W}{L}\frac{\mu C}{2}(V_G - V_t)^2 \tag{1.6}$$

Where μ is the field-effect mobility, W and L are the width and length of the channel respectively, C is the capacitance of the dielectric layer, V_G is the gate voltage, V_t is the threshold voltage, and V_{DS} is the source-drain voltage. In the saturation regime the current remains constant across the semiconducting channel and this is usually defined by $V_{DS} \geq V_G - V_t$ for an *n*-type device, while the linear regime is typically defined within the range of $V_{DS} < V_G - V_t$.

$$I_{DS} = \frac{W}{L}\mu c[(V_G - V_t)V_{DS} - \frac{{V_{DS}}^2}{2}] \tag{1.7}$$

These equations have the same form for *p*-type devices with sign differences taking into account the opposite polarity of the applied voltages [108]. The field-effect mobility (μ), and threshold voltage (V_t, the minimum gate voltage that must be applied to switch the device ON), can be calculated by measuring the output and transfer characteristics of a LEFET [108]. Furthermore, LEFETs have some common performance metrics with OLEDs such as brightness and EQE, the determination of which will be detailed in next chapter.

1.6.2 Temperature-dependent measurements

While charge transport in inorganic semiconductors is well understood, the same physics in organic semiconductors is a matter of some controversy. One of the main methods used to study charge transport in any semiconductor is measuring the electrical characteristics of the devices as a function of temperature. The results of these measurements for inorganic semiconductors where charge transport occurs *via* electronic band structures shows that the mobility increases at lower temperatures due to a decrease in lattice vibrations and electron-phonon interactions [112]. However, in case of their organic counterparts, one observes a decrease in mobility in most of the cases. There is a general agreement that charge transport in organic semiconductors occurs *via* hopping between localized states and there are several flavours of hopping transport that are subtly different and depend upon phenomena such as local disorder and trap density. There is no universal description of charge transport in OFETs, which appears to be carrier density and material specific [112].

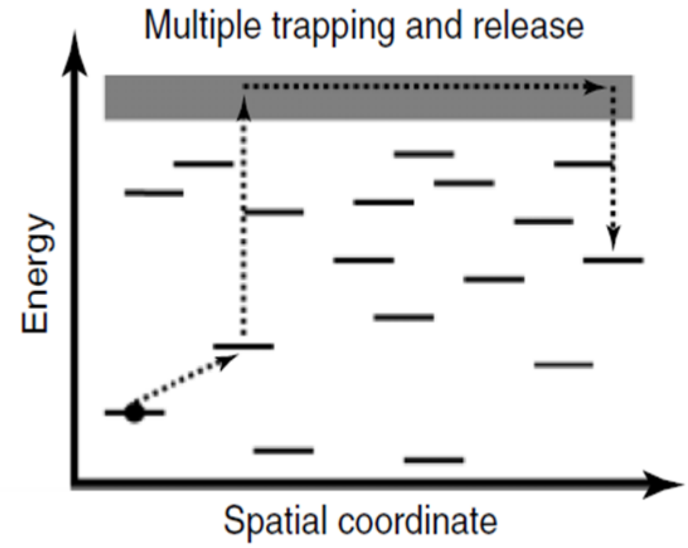

Figure 1.10 A schematic of the Multiple Trapping and Release Model adopted from [113].

To date, many models and studies have been reported for charge transport in organic semiconductors via temperature dependent measurements. The one which has been applied widely is the Multiple Trapping and Release Model [113]. According to this model there is a narrow delocalized band associated with a high concentration of localized levels that act as traps (see Figure 1.10) and traps are associated with lattice defects and impurities. Charge carriers therefore have a high probability of being trapped in localized states and subsequently released through thermally-activated processes. This form of transport depends on the energy of the trap states relative to the delocalised band, the temperature and the applied gate voltage [114]. The mobility of the semiconductor can be calculated by

$$\mu_D \propto \mu_0 exp\left[\frac{-E_t}{K_B T}\right] \tag{1.8}$$

where μ_D is the drift mobility, μ_0 is the trap free mobility representing the mobility in the delocalized band, E_t is the activation energy which is representing the energy difference between the transport band edge and the trap level, K_B is Boltzmann's constant and T is temperature.

Several other models such as the Polaron Model [115], the Gaussian Density of States Model [116], the Disorder-induced Localized State Model [117], and the Meyer-Neldel Rule [118] have been reported. All of these models rely on hopping transport but with slight differences in the details used to describe the behaviour of specific organic semiconductors, carrier densities and disorder-related phenomena. In some cases it has been shown that even for the same material different morphologies lead to different charge transport behaviour. As an example, the charge transport mechanism in pentacene has been explored using the transistor structure. Vapour deposited pentacene films displayed mobilities that were nearly independent of temperature [119] whereas solution-processed pentacene films show a strong dependence of the mobility on temperature [120]. These results highlight the challenges in studying the transport physics of organic semiconductors. All of the reports of temperature dependent measurements on organic semiconductors were performed using OFET structures. However, there are as yet no reports of combined studies into charge transport and recombination simultaneously in LEFET structures and this motivated the work presented in Chapter 6 of this thesis.

1.7 Aims of this project

Although organic light emitting devices have found their way into the display industry there is still a need for higher efficiency and easier mass production methods and great steps have been taken towards fully understanding organic semiconductors, which can pave the way to these goals. However, there are still significant opportunities for better understanding the structure-property relationships in organic semiconductors as they relate to OLEDs and LEFETs. This knowledge can lead to new chemical structure design of materials that provide better photo-physical and electrical properties. The invention of new classes of organic emissive semiconductors termed dendrimers provides better independent control over luminescent and transport properties. The three dimensional tree-like shapes of these materials can provide engineering of their branches responsible for molecular interaction, solubility, and viscosity which are useful tuning parameters for mass production techniques. Furthermore, desirable packing of molecules within the emissive layer may provide intentional orientation of dipoles which directly enhances the out-coupling in devices. The aims of this project are therefore three fold:

1. To study the photo-physics and dipole orientation in light emitting dendrimers and poly-dendrimers.
2. To develop an understanding of radiative recombination processes with molecular structure in dendrimers and poly(dendrimers) OLEDs.
3. To investigate the charge transport, charge injection and recombination physics in LEFET devices.

Chapter 2 will outline the systematic characterisation techniques of the materials to be tested, followed by fabrication and characterisation techniques for the OLED and LEFET devices used throughout the work presented in this thesis. *Chapter 3* details an introduction and overview of devices incorporating solution-processable dendrimers. This was the first time that an OLED device with neat emissive layer was demonstrated with a similar EQE to blended counterparts. The photo-physical and device characterisations are further investigated in chemically modified versions of the parent material these results are described in *Chapters 4* and *5*. In *Chapter 4* the fundamental benefits of the dendrimer system are described and the effects of dendrimer generation and type of dendron are presented. Furthermore, the effect of polymerisation of the dendrimers to form poly(dendrimer)s, promising materials for inkjet printing, will be outlined. The introduction of both electron- and hole-transporting moieties to form ambipolar co-polymers will also be discussed along with their photo-physical and electrical properties in *Chapter 5*. The work presented in this thesis culminates in *Chapter 6*, which describes temperature dependent measurement on LEFETs. Finally, *Chapter 7* summarises the findings of the work presented in this thesis, and the potential future for light emitting devices.

References

[1] http://www.digitaltrends.com/home-theater/the-future-of-seen-rollable-oled-displays/.

[2] S.G. Stevenson, Dendrimer light-emitting diodes, in, University of St Andrews, 2008.

[3] http://raqwe.blogspot.com.au/2013/10/iwatch-will-have-flexible-oled-display.html.

[4] S.R. Forrest, The path to ubiquitous and low-cost organic electronic appliances on plastic, Nature, 428 (2004) 911-918.

[5] A. Smith, Properties of Materials for Organic Light Emitting Diodes, (2011).

[6] R.M. News Samsung, 2011, http://www.samsung.com/us/news/newsRead.do?news_seq=19806.

[7] J. Kido, M. Kimura, K. Nagai, Multilayer white light-emitting organic electroluminescent device, Science, 267 (1995) 1332-1334.

[8] S. Reineke, F. Lindner, G. Schwartz, N. Seidler, K. Walzer, B. Lüssem, K. Leo, White organic light-emitting diodes with fluorescent tube efficiency, Nature, 459 (2009) 234-238.

[9] M.C. Gather, A. Köhnen, K. Meerholz, White Organic Light‐Emitting Diodes, Advanced Materials, 23 (2011) 233-248.

[10] E.B. Namdas, J.S. Swensen, P. Ledochowitsch, J.D. Yuen, D. Moses, A.J. Heeger, Gate‐Controlled Light Emitting Diodes, Advanced Materials, 20 (2008) 1321-1324.

[11] K. Nakamura, T. Hata, A. Yoshizawa, K. Obata, H. Endo, K. Kudo, Improvement of metal–insulator–semiconductor-type organic light-emitting transistors, Japanese Journal of Applied Physics, 47 (2008) 1889.

[12] E.B. Namdas, M. Tong, P. Ledochowitsch, S.R. Mednick, J.D. Yuen, D. Moses, A.J. Heeger, Low thresholds in polymer lasers on conductive substrates by distributed feedback nanoimprinting: progress toward electrically pumped plastic lasers, Advanced materials, 21 (2009) 799-802.

[13] M.C. Gwinner, S. Khodabakhsh, M.H. Song, H. Schweizer, H. Giessen, H. Sirringhaus, Integration of a Rib Waveguide Distributed Feedback Structure into a Light‐Emitting Polymer Field‐Effect Transistor, Advanced Functional Materials, 19 (2009) 1360-1370.

[14] T. Matsushita, T. Asada, S. Koseki, Relativistic study on emission mechanism in tris (2-phenylpyridine) iridium, The Journal of Physical Chemistry C, 111 (2007) 6897-6903.

[15] F. De Angelis, S. Fantacci, N. Evans, C. Klein, S.M. Zakeeruddin, J.-E. Moser, K. Kalyanasundaram, H.J. Bolink, M. Grätzel, M.K. Nazeeruddin, Controlling phosphorescence color and quantum yields in cationic iridium complexes: a combined experimental and theoretical study, Inorganic chemistry, 46 (2007) 5989-6001.

[16] K. Nozaki, Theoretical Studies on Photophysical Properties and Mechanism of Phosphorescence in [fac‐Ir (2‐phenylpyridine) 3], Journal of the Chinese Chemical Society, 53 (2006) 101-112.

[17] K. Nozaki, K. Takamori, Y. Nakatsugawa, T. Ohno, Theoretical studies of phosphorescence spectra of tris (2, 2'-bipyridine) transition metal compounds, Inorganic chemistry, 45 (2006) 6161-6178.

[18] S. Obara, M. Itabashi, F. Okuda, S. Tamaki, Y. Tanabe, Y. Ishii, K. Nozaki, M.-a. Haga, Highly phosphorescent iridium complexes containing both tridentate bis (benzimidazolyl)-benzene or-pyridine and bidentate phenylpyridine: Synthesis, photophysical properties, and theoretical study of Ir-bis (benzimidazolyl) benzene complex, Inorganic chemistry, 45 (2006) 8907-8921.

[19] T. Yutaka, S. Obara, S. Ogawa, K. Nozaki, N. Ikeda, T. Ohno, Y. Ishii, K. Sakai, M.-a. Haga, Syntheses and properties of emissive iridium (III) complexes with tridentate benzimidazole derivatives, Inorganic chemistry, 44 (2005) 4737-4746.

[20] T.D. Anthopoulos, M.J. Frampton, E.B. Namdas, P.L. Burn, I.D. Samuel, Solution‐Processable Red Phosphorescent Dendrimers for Light‐Emitting Device Applications, Advanced Materials, 16 (2004) 557-560.

[21] S.-C. Lo, E. Namdas, P. Burn, I. Samuel, Synthesis and properties of highly efficient electroluminescent green phosphorescent iridium cored dendrimers, Macromolecules, 36 (2003) 9721-9730.
[22] S.-C. Lo, C.P. Shipley, R.N. Bera, R.E. Harding, A.R. Cowley, P.L. Burn, I.D. Samuel, Blue phosphorescence from iridium (III) complexes at room temperature, Chemistry of materials, 18 (2006) 5119-5129.
[23] A.J. Heeger, N.S. Sariciftci, E.B. Namdas, Semiconducting and metallic polymers, Oxford University Press, 2010.
[24] K.E. Mutkins, Organic field-effect transistors based on dendrimers and small molecules, (2012).
[25] W. Brütting, Physics of organic semiconductors, John Wiley & Sons, 2006.
[26] C.W. Tang, S.A. VanSlyke, Organic electroluminescent diodes, Applied physics letters, 51 (1987) 913-915.
[27] M. Baldo, M. Thompson, S. Forrest, High-efficiency fluorescent organic light-emitting devices using a phosphorescent sensitizer, Nature, 403 (2000) 750-753.
[28] M. Baldo, M. Deutsch, P. Burrows, H. Gossenberger, M. Gerstenberg, V. Ban, S. Forrest, Organic vapor phase deposition, Advanced Materials, 10 (1998) 1505-1514.
[29] M. Shtein, P. Peumans, J.B. Benziger, S.R. Forrest, Direct mask-free patterning of molecular organic semiconductors using organic vapor jet printing, Journal of applied physics, 96 (2004) 4500-4507.
[30] Y. Sun, M. Shtein, S.R. Forrest, Direct patterning of organic light-emitting devices by organic-vapor jet printing, Applied Physics Letters, 86 (2005) 113504.
[31] M. Halim, I. Samuel, J. Pillow, A. Monkman, P. Burn, Control of colour and charge injection in conjugated dendrimer/polypyridine bilayer LEDs, Synthetic metals, 102 (1999) 1571-1574.
[32] M. Halim, J.N. Pillow, I.D. Samuel, P.L. Burn, Conjugated Dendrimers for Light‐Emitting Diodes: Effect of Generation, Advanced Materials, 11 (1999) 371-374.
[33] M. Halim, J. Pillow, I. Samuel, P. Burn, The effect of dendrimer generation on LED efficiency, Synthetic metals, 102 (1999) 922-923.
[34] M. Halim, I. Samuel, J. Pillow, P. Burn, Conjugated dendrimers for LEDs: Control of colour, Synthetic metals, 102 (1999) 1113-1114.
[35] J. Pillow, P. Burn, I. Samuel, M. Halim, Synthetic routes to phenylene vinylene dendrimers, Synthetic metals, 102 (1999) 1468-1469.
[36] J.N. Pillow, M. Halim, J.M. Lupton, P.L. Burn, I.D. Samuel, A facile iterative procedure for the preparation of dendrimers containing luminescent cores and stilbene dendrons, Macromolecules, 32 (1999) 5985-5993.
[37] K.A. Knights, S.G. Stevenson, C.P. Shipley, S.-C. Lo, S. Olsen, R.E. Harding, S. Gambino, P.L. Burn, I.D. Samuel, A rapid route to carbazole containing dendrons and phosphorescent dendrimers, Journal of Materials Chemistry, 18 (2008) 2121-2130.
[38] S. Gambino, S.G. Stevenson, K.A. Knights, P.L. Burn, I.D. Samuel, Control of Charge Transport in Iridium (III) Complex‐Cored Carbazole Dendrimers by Generation and Structural Modification, Advanced Functional Materials, 19 (2009) 317-323.
[39] J. Lupton, I.D. Samuel, R. Beavington, P.L. Burn, H. Bässler, Control of Charge Transport and Intermolecular Interaction in Organic Light‐Emitting Diodes by Dendrimer Generation, Advanced Materials, 13 (2001) 258-261.
[40] M.J. Frampton, S.W. Magennis, J.N. Pillow, P.L. Burn, I.D. Samuel, The effect of intermolecular interactions on the electro-optical properties of porphyrin dendrimers with conjugated dendrons, Journal of Materials Chemistry, 13 (2003) 235-242.
[41] J. Lupton, I. Samuel, R. Beavington, M. Frampton, P. Burn, H. Bässler, Control of mobility in molecular organic semiconductors by dendrimer generation, Physical Review B, 63 (2001) 155206.

[42] T.D. Anthopoulos, J.P. Markham, E.B. Namdas, J.R. Lawrence, I.D. Samuel, S.-C. Lo, P.L. Burn, Influence of molecular structure on the properties of dendrimer light-emitting diodes, Organic electronics, 4 (2003) 71-76.
[43] G. Hayes, I. Samuel, R. Phillips, Ultrafast dynamics of photoexcitations in conjugated polymers, Synthetic metals, 84 (1997) 889-890.
[44] G. Lanzani, G. Cerullo, C. Brabec, N. Sariciftci, Time domain investigation of the intrachain vibrational dynamics of a prototypical light-emitting conjugated polymer, Physical review letters, 90 (2003) 047402.
[45] J.-P.R. Wells, D.G. Lidzey, P.J. Phillips, D.A. Carder, A.M. Fox, Ultrafast measurements of vibrational relaxation in the conjugated polymer poly (9, 9-dioctylfluorene), Applied physics letters, 85 (2004) 3080-3082.
[46] N. Greenham, I. Samuel, G. Hayes, R. Phillips, Y. Kessener, S. Moratti, A. Holmes, R. Friend, Measurement of absolute photoluminescence quantum efficiencies in conjugated polymers, Chemical physics letters, 241 (1995) 89-96.
[47] K.-C. Tang, K.L. Liu, I.-C. Chen, Rapid intersystem crossing in highly phosphorescent iridium complexes, Chemical physics letters, 386 (2004) 437-441.
[48] M.A. Baldo, D. O'brien, Y. You, A. Shoustikov, S. Sibley, M. Thompson, S. Forrest, Highly efficient phosphorescent emission from organic electroluminescent devices, Nature, 395 (1998) 151-154.
[49] M. Baldo, S. Lamansky, P. Burrows, M. Thompson, S. Forrest, Very high-efficiency green organic light-emitting devices based on electrophosphorescence, Applied Physics Letters, 75 (1999) 4.
[50] A. Hayer, A.L. Khan, R.H. Friend, A. Köhler, Morphology dependence of the triplet excited state formation and absorption in polyfluorene, Physical Review B, 71 (2005) 241302.
[51] O. Korovyanko, R. Österbacka, X.M. Jiang, Z.V. Vardeny, R. Janssen, Photoexcitation dynamics in regioregular and regiorandom polythiophene films, Physical Review B, 64 (2001) 235122.
[52] B. Kraabel, V. Klimov, R. Kohlman, S. Xu, H. Wang, D. McBranch, Unified picture of the photoexcitations in phenylene-based conjugated polymers: Universal spectral and dynamical features in subpicosecond transient absorption, Physical review B, 61 (2000) 8501.
[53] R. Joseph, Lakowicz. Principles of fluorescence spectroscopy, in, Springer, 2006.
[54] M. Baldo, D. O’brien, M. Thompson, S. Forrest, Excitonic singlet-triplet ratio in a semiconducting organic thin film, Physical Review B, 60 (1999) 14422.
[55] R. Friend, R. Gymer, A. Holmes, J. Burroughes, R. Marks, C. Taliani, D. Bradley, D. Dos Santos, J. Bredas, M. Lögdlund, Electroluminescence in conjugated polymers, Nature, 397 (1999) 121-128.
[56] J. Wilson, A. Dhoot, A. Seeley, M. Khan, A. Köhler, R. Friend, Spin-dependent exciton formation in π-conjugated compounds, Nature, 413 (2001) 828-831.
[57] M. Segal, M. Baldo, R. Holmes, S. Forrest, Z. Soos, Excitonic singlet-triplet ratios in molecular and polymeric organic materials, Physical Review B, 68 (2003) 075211.
[58] C. Adachi, M.A. Baldo, M.E. Thompson, S.R. Forrest, Nearly 100% internal phosphorescence efficiency in an organic light-emitting device, Journal of Applied Physics, 90 (2001) 5048-5051.
[59] Y. Kawamura, K. Goushi, J. Brooks, J.J. Brown, H. Sasabe, C. Adachi, 100% phosphorescence quantum efficiency of Ir (III) complexes in organic semiconductor films, Applied Physics Letters, 86 (2005) 71104-71104.
[60] G.A. Crosby, J.N. Demas, Measurement of photoluminescence quantum yields. Review, The Journal of Physical Chemistry, 75 (1971) 991-1024.
[61] P.E. Shaw, Measurements of exciton diffusion in conjugated polymers, in, University of St Andrews, 2009.
[62] F. So, Organic electronics: materials, processing, devices and applications, CRC press, 2009.

[63] C. Tang, S. VanSlyke, C. Chen, Electroluminescence of doped organic thin films, Journal of Applied Physics, 65 (1989) 3610-3616.
[64] Y. Shirota, H. Kageyama, Charge carrier transporting molecular materials and their applications in devices, Chemical reviews, 107 (2007) 953-1010.
[65] V.V. Jarikov, D.Y. Kondakov, C.T. Brown, Efficient and extremely long-lived organic light-emitting diodes based on dinaphthylperylene, Journal of Applied Physics, 102 (2007) 104908.
[66] S.R. Forrest, D.D. Bradley, M.E. Thompson, Measuring the Efficiency of Organic Light ‐ Emitting Devices, Advanced Materials, 15 (2003) 1043-1048.
[67] T. Smith, J. Guild, The CIE colorimetric standards and their use, Transactions of the Optical Society, 33 (1931) 73.
[68] W.J. Begley, T.K. Hatwar, 36.2: High ‐ Performing Organic Electron ‐ Injecting and Transporting Layers for Red, Green, Blue, and White OLED Devices, in: SID Symposium Digest of Technical Papers, Wiley Online Library, 2007, pp. 1286-1289.
[69] C. Wu, C. Wu, J. Sturm, A. Kahn, Surface modification of indium tin oxide by plasma treatment: An effective method to improve the efficiency, brightness, and reliability of organic light emitting devices, Applied Physics Letters, 70 (1997) 1348-1350.
[70] M. Mason, L.S. Hung, C. Tang, S. Lee, K. Wong, M. Wang, Characterization of treated indium–tin–oxide surfaces used in electroluminescent devices, Journal of applied physics, 86 (1999) 1688-1692.
[71] I.-M. Chan, F.C.-N. Hong, Plasma treatments of indium tin oxide anodes in carbon tetrafluorinde (CF 4)/oxygen (O 2) to improve the performance of organic light-emitting diodes, Thin Solid Films, 444 (2003) 254-259.
[72] L. Hung, L. Zheng, M. Mason, Anode modification in organic light-emitting diodes by low-frequency plasma polymerization of CHF3, Applied Physics Letters, 78 (2001) 673.
[73] X. Wang, P. Rundle, M. Bale, A. Mosley, Improved operating lifetime of phosphorescent OLED by novel anode coating, Synthetic metals, 137 (2003) 1051-1052.
[74] T.P. Saragi, T. Spehr, A. Siebert, T. Fuhrmann-Lieker, J. Salbeck, Spiro compounds for organic optoelectronics, Chemical reviews, 107 (2007) 1011-1065.
[75] S. Van Slyke, C. Chen, C. Tang, Organic electroluminescent devices with improved stability, Applied physics letters, 69 (1996) 2160-2162.
[76] J. Kim, M. Granström, R. Friend, N. Johansson, W. Salaneck, R. Daik, W. Feast, F. Cacialli, Indium–tin oxide treatments for single-and double-layer polymeric light-emitting diodes: The relation between the anode physical, chemical, and morphological properties and the device performance, Journal of applied physics, 84 (1998) 6859-6870.
[77] L. Hung, C. Tang, M. Mason, P. Raychaudhuri, J. Madathil, Application of an ultrathin LiF/Al bilayer in organic surface-emitting diodes, Applied Physics Letters, 78 (2001) 544-546.
[78] H. Yersin, Highly efficient OLEDs with phosphorescent materials, John Wiley & Sons, 2008.
[79] M. Pfeiffer, K. Leo, X. Zhou, J. Huang, M. Hofmann, A. Werner, J. Blochwitz-Nimoth, Doped organic semiconductors: Physics and application in light emitting diodes, Organic Electronics, 4 (2003) 89-103.
[80] K.A. Neyts, Simulation of light emission from thin-film microcavities, JOSA A, 15 (1998) 962-971.
[81] W. Brütting, J. Frischeisen, T.D. Schmidt, B.J. Scholz, C. Mayr, Device efficiency of organic light ‐ emitting diodes: Progress by improved light outcoupling, physica status solidi (a), 210 (2013) 44-65.
[82] S. Zeng, D. Baillargeat, H.-P. Ho, K.-T. Yong, Nanomaterials enhanced surface plasmon resonance for biological and chemical sensing applications, Chemical Society Reviews, 43 (2014) 3426-3452.
[83] https://en.wikipedia.org/wiki/Surface_plasmon_polariton#cite_note-1.

[84] S. Nowy, B.C. Krummacher, J. Frischeisen, N.A. Reinke, W. Brütting, Light extraction and optical loss mechanisms in organic light-emitting diodes: Influence of the emitter quantum efficiency, Journal of Applied Physics, 104 (2008) 123109.

[85] L.H. Smith, J.A. Wasey, I.D. Samuel, W.L. Barnes, Light Out‐Coupling Efficiencies of Organic Light‐Emitting Diode Structures and the Effect of Photoluminescence Quantum Yield, Advanced Functional Materials, 15 (2005) 1839-1844.

[86] S. Nowy, J. Frischeisen, W. Brütting, Simulation based optimization of light-outcoupling in organic light-emitting diodes, in: SPIE Photonic Devices+ Applications, International Society for Optics and Photonics, 2009, pp. 74151C-74151C-74159.

[87] S.D. Choudhury, R. Badugu, K. Ray, J.R. Lakowicz, Surface-plasmon induced polarized emission from Eu (iii)–a class of luminescent lanthanide ions, Chemical Communications, 50 (2014) 9010-9013.

[88] S. Mladenovski, K. Neyts, D. Pavicic, A. Werner, C. Rothe, Exceptionally efficient organic light emitting devices using high refractive index substrates, Optics Express, 17 (2009) 7562-7570.

[89] W.H. Koo, S.M. Jeong, F. Araoka, K. Ishikawa, S. Nishimura, T. Toyooka, H. Takezoe, Light extraction from organic light-emitting diodes enhanced by spontaneously formed buckles, Nature Photonics, 4 (2010) 222-226.

[90] M.K. Callens, H. Marsman, L. Penninck, P. Peeters, H. de Groot, J.M. ter Meulen, K. Neyts, RCWA and FDTD modeling of light emission from internally structured OLEDs, Optics express, 22 (2014) A589-A600.

[91] C. Fuchs, T. Schwab, T. Roch, S. Eckardt, A. Lasagni, S. Hofmann, B. Lüssem, L. Müller-Meskamp, K. Leo, M. Gather, Quantitative allocation of Bragg scattering effects in highly efficient OLEDs fabricated on periodically corrugated substrates, Optics express, 21 (2013) 16319-16330.

[92] K. Saxena, V. Jain, D.S. Mehta, A review on the light extraction techniques in organic electroluminescent devices, Optical Materials, 32 (2009) 221-233.

[93] D. Yokoyama, Molecular orientation in small-molecule organic light-emitting diodes, Journal of Materials Chemistry, 21 (2011) 19187-19202.

[94] T.D. Schmidt, D.S. Setz, M. Flämmich, J. Frischeisen, D. Michaelis, B.C. Krummacher, N. Danz, W. Brütting, Evidence for non-isotropic emitter orientation in a red phosphorescent organic light-emitting diode and its implications for determining the emitter's radiative quantum efficiency, Applied Physics Letters, 99 (2011) 163302.

[95] H. Sasabe, J. Kido, Development of high performance OLEDs for general lighting, Journal of Materials Chemistry C, 1 (2013) 1699-1707.

[96] H. Sasabe, J. Kido, Recent Progress in Phosphorescent Organic Light‐Emitting Devices, European Journal of Organic Chemistry, 2013 (2013) 7653-7663.

[97] D. Yokoyama, A. Sakaguchi, M. Suzuki, C. Adachi, Horizontal orientation of linear-shaped organic molecules having bulky substituents in neat and doped vacuum-deposited amorphous films, Organic Electronics, 10 (2009) 127-137.

[98] J. Wasey, A. Safonov, I. Samuel, W. Barnes, Effects of dipole orientation and birefringence on the optical emission from thin films, Optics communications, 183 (2000) 109-121.

[99] M. Flämmich, M.C. Gather, N. Danz, D. Michaelis, A.H. Bräuer, K. Meerholz, A. Tünnermann, Orientation of emissive dipoles in OLEDs: Quantitative in situ analysis, Organic Electronics, 11 (2010) 1039-1046.

[100] J. Frischeisen, D. Yokoyama, A. Endo, C. Adachi, W. Brütting, Increased light outcoupling efficiency in dye-doped small molecule organic light-emitting diodes with horizontally oriented emitters, Organic Electronics, 12 (2011) 809-817.

[101] M. Flämmich, J. Frischeisen, D.S. Setz, D. Michaelis, B.C. Krummacher, T.D. Schmidt, W. Brütting, N. Danz, Oriented phosphorescent emitters boost OLED efficiency, Organic Electronics, 12 (2011) 1663-1668.

[102] K.-H. Kim, S. Lee, C.-K. Moon, S.-Y. Kim, Y.-S. Park, J.-H. Lee, J.W. Lee, J. Huh, Y. You, J.-J. Kim, Phosphorescent dye-based supramolecules for high-efficiency organic light-emitting diodes, Nature communications, 5 (2014).
[103] M.J. Jurow, C. Mayr, T.D. Schmidt, T. Lampe, P.I. Djurovich, W. Brütting, M.E. Thompson, Understanding and predicting the orientation of heteroleptic phosphors in organic light-emitting materials, Nature materials, (2015).
[104] C.-K. Moon, K.-H. Kim, J.W. Lee, J.-J. Kim, Influence of host molecules on emitting dipole orientation of phosphorescent iridium complexes, Chemistry of Materials, 27 (2015) 2767-2769.
[105] Y. Sakai, M. Shibata, D. Yokoyama, Simple model-free estimation of orientation order parameters of vacuum-deposited and spin-coated amorphous films used in organic light-emitting diodes, Applied Physics Express, 8 (2015) 096601.
[106] S.Y. Kim, W.I. Jeong, C. Mayr, Y.S. Park, K.H. Kim, J.H. Lee, C.K. Moon, W. Brütting, J.J. Kim, Organic Light‐Emitting Diodes with 30% External Quantum Efficiency Based on a Horizontally Oriented Emitter, Advanced Functional Materials, 23 (2013) 3896-3900.
[107] J. Frischeisen, D. Yokoyama, C. Adachi, W. Brütting, Determination of molecular dipole orientation in doped fluorescent organic thin films by photoluminescence measurements, Applied Physics Letters, 96 (2010) 073302.
[108] Z. Bao, J. Locklin, Organic field-effect transistors, CRC press, 2007.
[109] H. Klauk, Organic electronics II: more materials and applications, John Wiley & Sons, 2012.
[110] J.S. Swensen, J. Yuen, D. Gargas, S.K. Buratto, A.J. Heeger, Light emission from an ambipolar semiconducting polymer field effect transistor: Analysis of the device physics, Journal of applied physics, 102 (2007) 013103.
[111] K. Tandy, Active channel field-effect transistors: Towards high performance light emitting transistors, (2014).
[112] G. Horowitz, Organic field-effect transistors, Advanced Materials, 10 (1998) 365-377.
[113] R. Noriega, A. Salleo, Charge transport theories in organic semiconductors, Organic Electronics II: More Materials and Applications, 2 (2012).
[114] G. Horowitz, R. Hajlaoui, P. Delannoy, Temperature dependence of the field-effect mobility of sexithiophene. Determination of the density of traps, Journal de Physique III, 5 (1995) 355-371.
[115] I. Hulea, S. Fratini, H. Xie, C. Mulder, N. Iossad, G. Rastelli, S. Ciuchi, A. Morpurgo, Tunable Fröhlich polarons in organic single-crystal transistors, Nature Materials, 5 (2006) 982-986.
[116] H. Bässler, Charge transport in disordered organic photoconductors, phys. status solidi b, 175 (1993) 15-56.
[117] N. Mott, E. Davis, Electronic processes in non-crystalline solids, Clarendon, Oxford, (1979) 465.
[118] M. Ullah, PhD dissertation , Johannes Kepler University, Linz (2011).
[119] S. Nelson, Y.-Y. Lin, D. Gundlach, T. Jackson, Temperature-independent transport in high-mobility pentacene transistors, Applied physics letters, 72 (1998) 1854-1856.
[120] A. Brown, C. Jarrett, D. De Leeuw, M. Matters, Field-effect transistors made from solution-processed organic semiconductors, Synthetic metals, 88 (1997) 37-55.

Chapter 2

Experimental Methods and Equipment

2.1 Introduction

This chapter focuses on describing the characterisation and fabrication techniques for organic light emitting materials and devices utilised in the research. The first Section of this chapter details the systematic photo-physical characterisation of organic materials utilizing techniques including UV-Vis absorption, photo luminescence quantum yield, photo luminescence decay life time, ellipsometry and dipole orientation measurements. The results of such studies provide better understanding to optimize device fabrication activities which are described in the next Section of this chapter. After a brief overview of the primary procedures, device fabrication details will be given for two different configurations of organic light emitting diodes and light emitting field effect transistors. Finally, the standard optical and electrical methodologies for characterising light emitting devices will be described, noting that experiment-specific details will also be provided in subsequent chapters where relevant.

2.2 Materials

Different classes of material were used in the work described in this thesis including dendrimers, polymers and small molecules. All dendrimers were synthesised at the centre for organic photonics and electronics (COPE). These dendrimers were used in OLED devices. The diketopyrrolopyrrole–dithienothiophene (DPP–DTT) co-polymer was synthesised as described in reference [1] and used in the LEFET architecture. The commercial small molecules used in the work described in this thesis were restricted to a choice of 4,4’-N,N’-dicarbazolyl-biphenyl (CBP), 2,2',2"-(1,3,5-Benzinetriyl)-tris(1-phenyl-1-H-benzimidazole) (TPBi) purchased from Lumtec and co-polymer phenyl-substituted poly(p-phenylenevinylene) knows as Super Yellow (SY) from Merck. Chemical structures of these materials will be given in relevant chapters.

2.3 Material characteristics

2.3.1 Energy level estimation

Ionisation potentials were measured by photoelectron spectroscopy in air (PESA) in order to estimate the energy levels (HOMOs) for synthesised materials. Measurements were performed using Riken Keiki AC-2 spectrometer using 5nW power intensity.

In order to estimate the LUMO energy, optical gaps were appraised from the intersection of the normalised absorption and solid-state photoluminescent spectra plotted in units of energy (eV). The optical gaps were then added to the HOMO energies to determine the LUMOs [2]. HOMO and LUMO then considered in order choosing the best match for host materials and contacts.

2.3.2 Absorption

The results of absorption measurements presented in this thesis were all obtained using a Cary 5000 UV-Vis spectrophotometer either as in optically dilute solutions in spectroscopic grade solvent or a thin film on quartz. This equipment was capable of measuring intensity of absorption in the wavelength range of 800 nm to 200 nm. The instrument contains two channels for reference and sample. The reference was designed in order to account for any absorption by the solvent or quartz (in the case of spin-coated films) or cuvette (for solution). Absorbance was calculated through comparison of transmission (T) of the sample and reference while both illuminated with the same intensity [2]. Absorbance (A) is then given by the relation

$$A = -\log(T) \tag{2.1}$$

2.3.3 Photoluminescence

The photoluminescence spectra of the compounds were measured by a Jobin-Yvon Fluoromax 4 fluorimeter where a range of excitation wavelengths was provided by a xenon lamp coupled through a monochromator. Samples were excited at the peak of the absorbance at an angle of 45 degree and emission was collected for a specific range of wavelengths by a photomultiplier tube (PMT). PL spectra were then determined after correction for the quantum efficiency of the PMT by the instrumental software.

Solution samples were made using spectroscopic grade solvent Toluene and were degassed by three freeze-pump-thaw cycles before measurements [3]. Solid-state neat films were made by spin coating from spectroscopic grade chlorobenzene solution onto glass substrates at a concentration of 20 mg/ml giving thickness about 50-80 nm. Blend films were spin coated from a 20 mg/ml solution of 20 wt% dopant with 4,4'- bis(N-carbazole)biphenyl (CBP).

2.3.4 Photoluminescence quantum yield

An excited state is formed in any semiconductor material when light of the appropriate energy is absorbed. In an organic semiconductor photoexcitation is excitonic in nature as described in [2]. This excited state decays to the ground state either radiatively or non-radiatively. The photoluminescence quantum yield is the ratio of the number of photons emitted to the number of photons absorbed. This vital parameter quantifies how luminescent a material is. PLQY measurements described in this thesis were performed either for optically dilute solutions or solid-state film.

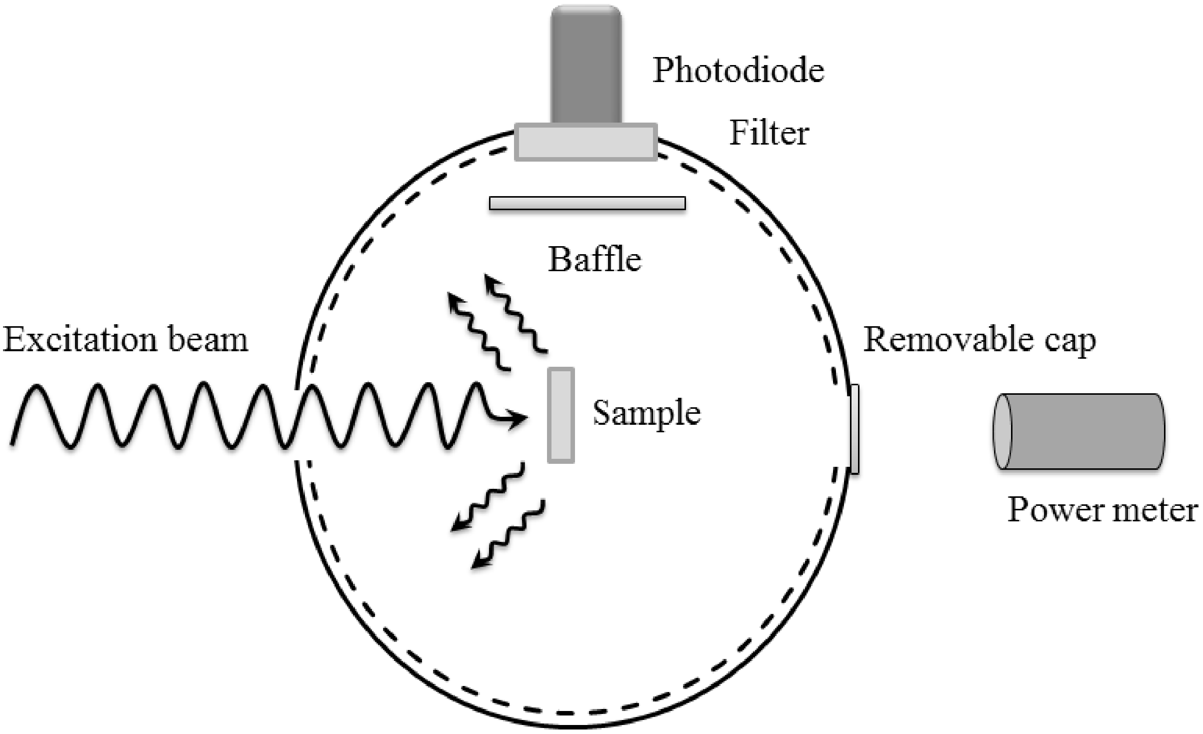

Figure 2. 1 Schematic diagram of the experimental set up of PLQY measurement of organic thin films.

The solution PLQY measurements were performed by comparing emission spectra of the degassed solutions to a standard solution with a known quantum yield. Quinine sulphate in 0.5 M H_2SO_4 was used as the standard solution with a PLQY equal to 55% [2] when excited at 360 nm. Both reference and sample solutions were prepared with an optical density of 0.1 and as explained in previous Section, the PLQY was calculated as:

$$Q_S = Q_R * \left(\frac{A_R}{A_S}\right) * \left(\frac{n_S^2}{n_R^2}\right) * \left(\frac{D_S}{D_R}\right) \tag{2.2}$$

When Q_S and Q_R are PLQY values for sample and reference respectively, A_R and A_S are absorbance values at 360 nm, n_S and n_R are refractive indexes of sample and reference, and D_S and D_R are sums of corrected PL values. Corrected PL values for sample and reference are calculated from

$$corrected\ PL = PL\ * 10^{\frac{absorbance}{2}} \tag{2.3}$$

Film PLQY measurements are problematic due to the complicated angular distribution of emission [4]. Total internal reflection and wave guiding are two parameters which make emission of a film non-isotropic; therefore the detector would measure different intensities, depending on its orientation relative to the sample. This complication is resolved with the use of an integrating sphere to collect total emission from the sample. The integrated sphere is a hollow sphere in which the interior surface is coated with a diffusely scattering layer in order to distribute the emission uniformly.

A schematic diagram of the experimental set up is shown in Figure 2.1. The sphere is designed to have a small entrance at one side to illuminate the sample placed at the centre of the sphere. Another aperture is opened on the opposite side of the sphere to measure the transmitted laser beam by a power meter located outside sphere. A further hole is located on the other side as shown in Figure 2.1 where a photodiode is attached to measure the resulting luminescence. The baffle in front of photodiode prevents the sample’s emission from directly irradiating the photo diode and also a long pass filter to block any residual laser excitation. In order to decrease the rate of photo degradation, the sample is measured under flowing nitrogen. The experimental parameters are measured as follows:

1. X_{laser}: The intensity of the excitation laser which measured with the photodiode without the long pass filter and the sample.
2. X_{sample}: The intensity of total emission with the sample became incident with the laser and the filter back to block the laser beam.
3. T: The transmitted excitation power was measured with a power meter with the cap removed from the aperture.
4. X_{sphere} : The photodiode intensity was measured again while the sample was removed from the beam path which corresponds to the sample emission due to secondary excitation from the scattered excitation.

5. R : The reflected excitation power from the sample was measured outside sphere with the power meter.

The PLQY, η was calculated from:

$$\eta = \frac{x}{y} \tag{2.4}$$

Where x and y are given by:

$$x = \frac{X_{sample} - (R+T)X_{sphere}}{(1-R-T)X_{laser}} \tag{2.5}$$

$$y = \int S_{sphere}(\lambda)L(\lambda)G(\lambda)F(\lambda)d\lambda \times \left(S_{sphere}(\lambda_{ex})G(\lambda_{ex}) \int L(\lambda)d\lambda\right)^{-1} \tag{2.6}$$

Where S_{sphere} is the integrating sphere spectral response, L is the emission spectrum from the sample, G is the spectral response of photodiode, F is the long pass filter transmission spectrum and λ_{ex} is the excitation wavelength. In order to avoid introducing large error into measurement, it is important to have a strongly absorbent film at the excitation wavelength with an absorbance above 0.3 [5].

2.3.5 Photoluminescence decay lifetime

Time correlated single photon counting (TCSPC) can provide information about radiative and non-radiative rates when combined with PLQY results. It is the probability distribution for the emission of a single exciton after an excitation event which corresponds to emission intensity versus time. This distribution can be determined by sampling the emission of single photons following a large number of low intensity excitation events.

All time-resolved photoluminescence spectroscopy described in this thesis were performed using a Fluorolog 4 with TCSPC capability. A pulsed LED emitting at 372 nm was used to photoexcite the samples. Solution samples were prepared and degassed as explained previously in this chapter. Film samples were kept in a vacuum of $< 10^{-3}$ mbar during measurements. All measurements were conducted at room temperature with the excitation repetition rate of 100 kHz with 5 ns delay. The subsequent emitted photon was then detected perpendicular to the excitation beam. The PL decay data points were fitted by a sum of exponential functions as given by;

$$I(t) = I_0 \sum_i A_i e^{-\frac{t}{\tau_i}} \tag{2.7}$$

Where $\sum_i A_i = 1$, A and τ represent the pre-exponential factors and time constants respectively [2].

2.3.6 Ellipsometry

To understand and simulate emission out coupling of OLED devices, optical constants (n and k) of emissive layer were needed. To achieve this, variable angle spectroscopic ellipsometry (VASE) was performed on a J. A. Woollam VUV-VASE ellipsometer to extract the thickness and optical constants. In this technique, a sample is targeted with linearly polarised white light and the subsequent reflections are detected at the angle ϕ.The reflected light becomes elliptically polarised due to phase change from interaction of light with the sample. Optical constants are then determined by measuring the relative phase change and intensity of the reflected beam as a function of angle and wavelength. These parameters are then used in an isotropic optical model or a uniaxial model for amorphous or crystalline materials respectively to obtain optical constants [6].

2.3.7 Dipole orientation measurement

Orientation of the transition dipole moments of an emitter is a crucial factor affecting the quantum efficiency and out coupling efficiency in OLEDs. Increasing horizontal dipole orientation in the emissive layer leads to higher out coupling efficiency than isotropic or vertically oriented dipoles. In the work described in this thesis two methods were performed to estimate dipole orientation in emissive materials.

In the first method, optical constants obtained from ellipsometry measurements were used to calculate the orientation order parameter S, which is defined as

$$S = \frac{3\langle \cos^2 \theta \rangle - 1}{2} = \frac{K_e^{max} - K_o^{max}}{K_e^{max} + 2K_o^{max}} \tag{2.8}$$

Where θ is the angle between the axis of the transition dipole moment and the direction vertical to the substrate surface as shown in Figure 2.2, $\langle \cos^2 \theta \rangle$ indicates the ensemble average, and K_o^{max} and K_e^{max} are the ordinary and extraordinary extinction coefficients at the peak of the band attributed to the transition dipole moment, respectively.

As a result, $S = -0.5$ $(\theta = 90°)$ if the transition dipole moments are perfectly oriented horizontally to the substrate surface, $S = 0$ if they are randomly oriented, and $S = 1(\theta = 0°)$ if the molecules are totally orientated vertically to the substrate surface [7].

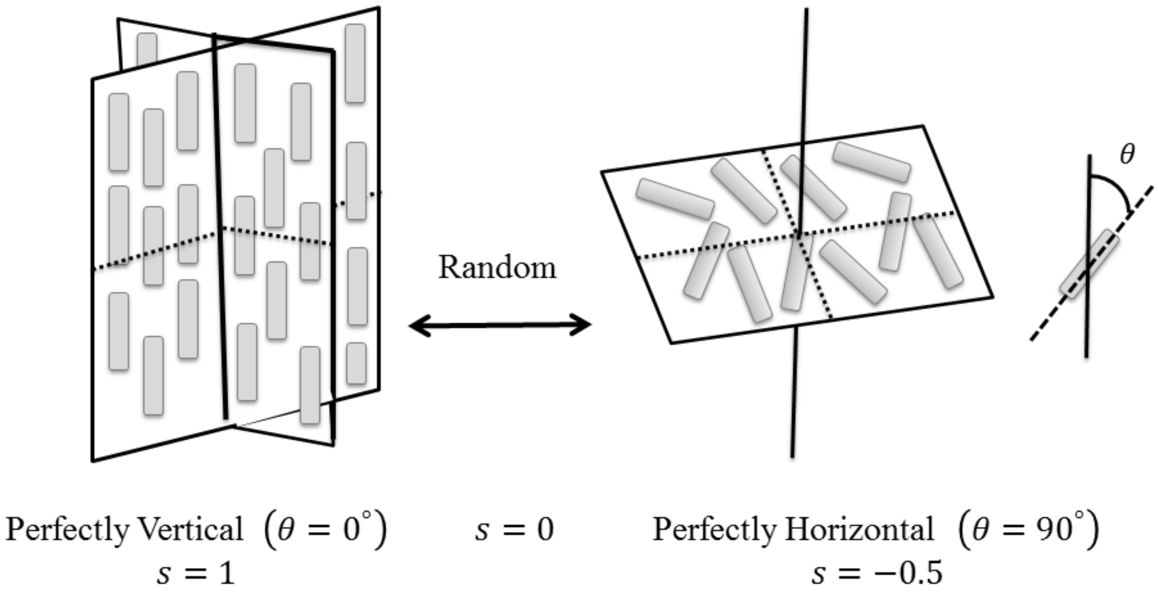

Figure 2. 2 Relationship between the optical anisotropy in films and molecular orientation.

The second method utilised was to measure the light emission intensity in a transverse magnetic (TM) mode on the emission angle (angle dependent PL measurements) [8-11]. A 15nm thick film was prepared on a cleaned fused silica substrate or glass followed by encapsulation. The sample was then attached to a half cylinder fused silica prism via matching oil, with the film surface precisely at the centre of a manual rotational stage from Thorlab (see Figure 2.3). Photoexcitation of the sample was performed using a circularly polarized He-Ca laser beam at 325 nm wavelength with less than 0.2 mW power. Measurements were performed at a fixed incident angle of 45° while nitrogen was flowing on the sample to avoid the photo degradation. The emission from the sample at different angles from 0° to 90° were collected by a fibre coupled Ocean Optics USB2000 spectrometer through a polariser (TM mode) and a long pass filter with a cut-off wavelength of 400 nm. A second laser beam was coincident with the centre of the rotational stage to adjust the optical axis of the setup in order to have precise measurements.

To estimate dipole orientation, far-field emission intensity as a function of angle was simulated using commercial software Setfos 4, Fluxim Co with the known optical constants and thickness of the film provided by VASE measurements.

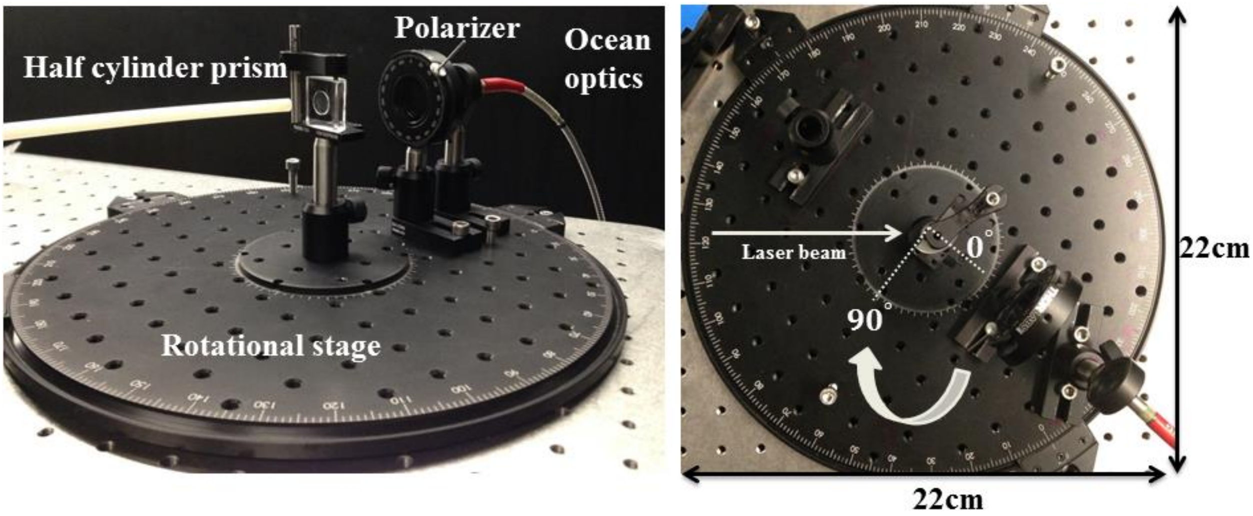

Figure 2. 3 Close up of the angle dependent PL spectrum setup from two directions.

2.4 Device fabrication

In the work detailed in this thesis, two device architectures were utilised, namely vertical structure OLED and planer LEFET. Both devices were fabricated and tested in class 1000 cleanrooms. The two device configurations which will be discussed in this thesis are as follows (see Figure 2.4):

- OLEDs consisting of glass substrate with pre-patterned ITO as the anode, poly(3,4-ethylenedioxythiophene) polystyrene sulfonate (PEDOT:PSS) a hole transport layer (HTL), an organic emissive layer, an electron transport layer (ETL), and a cathode electrode.
- LEFETs consisting of Si substrates as the gate electrode, SiNx as the inorganic dielectric layer, an organic dielectric layer as the passivation layer, an organic charge transport layer, an organic emissive layer, and the source and drain contacts.

Some common techniques are present in all device fabrications which will be discussed in this Section. Details specific to each experiment will be then given in relevant chapters.

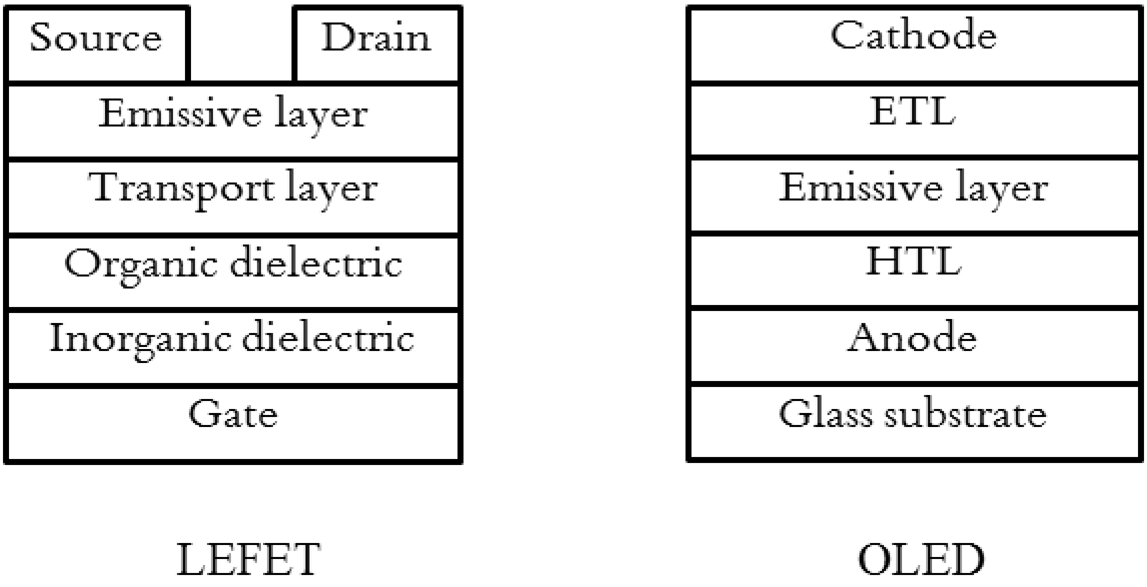

Figure 2. 4 Schematic device structure for OLED and LEFET.

2.4.1 Substrate preparation

Substrates were first rinsed with acetone and wiped with an acetone-wet swab before ultra-sonication in acetone for 15 mins. The substrates were rinsed with 2-propanol followed by ultra-sonication in 2-propanol for 15 min. Substrates were dried under nitrogen flow.

The substrates were then transferred to a glove box for deposition of subsequent layers (for LEFETs) or to be treated by UV ozone for 15min (for OLEDs). The glove box was maintained with a positive pressure nitrogen atmosphere, and oxygen and water levels are maintained at less than 0.1 ppm.

2.4.2 Thin film deposition

Films were deposited by spin-coating if the materials were able to be solution processed. The spin-coating speed and time depended on the concentration and thickness calibration. In cases where a material was not suitable for solution process deposition, organic layers were deposited via thermal evaporation under vacuum of $1-5\times10^{-6}$ mbar and oxygen and water levels less than $1-5\times10^{-9}$ ppm.

2.4.3 Film thickness determination

Film thickness is an important matter in organic electronics as it has a crucial effect on device performance and optimization of external efficiency. Thickness calibration was performed via a Dektak 150 profilometer. To do so, film thicknesses were measured at relevant spots on the substrate for five spots. Numbers were then averaged and used for calibration. In the case of thermal deposition, a quartz crystal monitor was used during evaporation and then thickness was verified using the Dektak profilometer.

2.4.4 Contact deposition

Cathode electrodes (in OLEDs) and source, drain electrodes (in LEFETs) were deposited via shadow masks. Shadow masks were made from steel using laser cutting. Contacts were then deposited through the shadow masks by thermal evaporation under a vacuum of $1 - 5 \times 10^{-6}$ mbar.

2.5 Device characterisation

2.5.1 Standard measurements for light emission

For light emitting devices (OLEDs and LEFETs), the brightness and external quantum efficiency must be determined in order to evaluate device performance. Since light emitting devices are used mainly in display technology viewed by humans a measure of the human eye response should be taken into account when describing their performances. Therefore, photometric units are used to characterise light accounting for the sensitivity of the human eye [12]. However, physical quantities of light such as number of photons, photon energy, or optical power are needed to be able to determine EQE values. These quantities are radiometric units. Formal definitions of some of the important photometric parameters for characterising light emitting devices are as follows:

Luminous intensity –light intensity of an optical source as observed by the human eye [12] with unit measurements of candelas (cd). Candela is the light intensity of 1 standardised candle.

Candela –*the candela is the luminous intensity, in a given direction, of a source that emits monochromatic radiation of frequency* 540×10^{12} *Hz and that has a radiant intensity in that direction of 1/683 watt per steradian* [13].

Luminance or brightness –the ratio of luminous intensity emitted in specific direction divided by the observed surface area in that direction, giving that light emitted in a solid angle from the source, brightness is measured in cd/m^2.

Luminous flux –the light power perceived by human eye from a source measured by unit lumen (lm) [12].

Lumen – *a monochromatic light source emitting an optical power of 1/683 watt at 555 nm has a luminous flux of 1 lumen (lm)* [12].

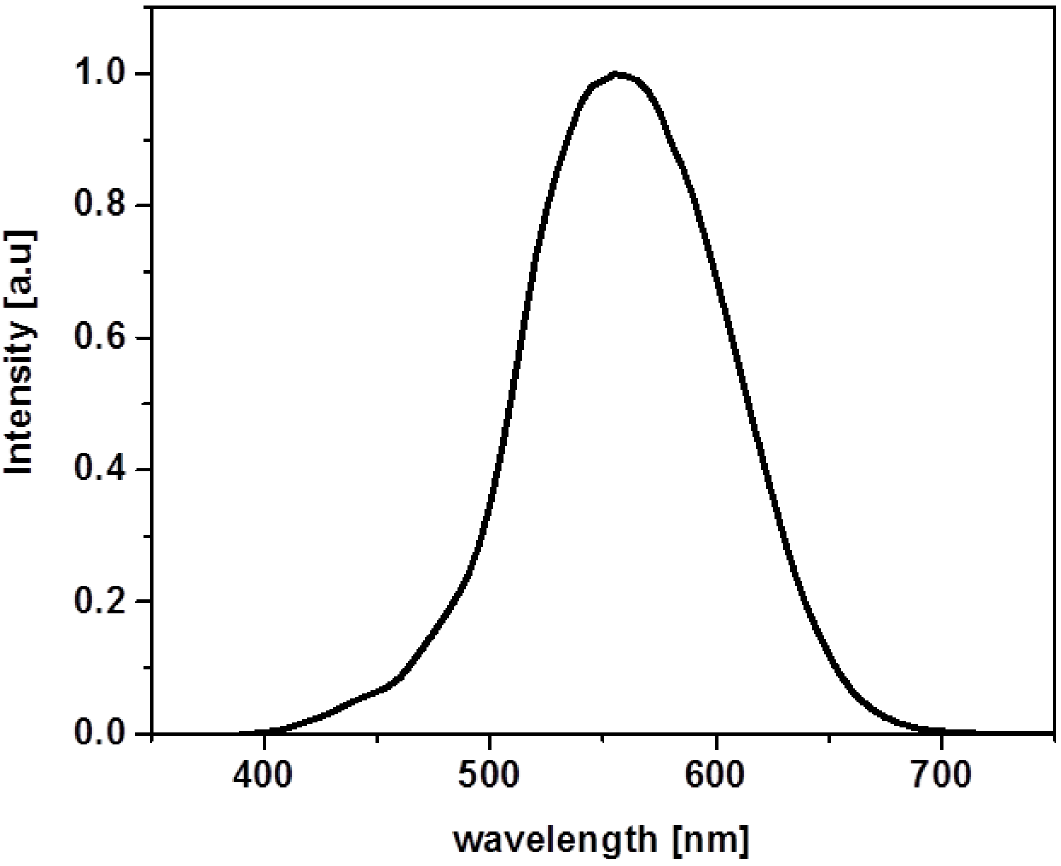

Figure 2. 5 Normalized CIE 1931 eye response curve as a function of wavelength.

The optical power, P_{out}, (a radiometric unit) and the luminous flux, ϕ_{lum}, (a photometric unit) needs to be related by a conversion factor in order to calculate the number of photons emitted by a light emitting device. The luminous flux ϕ_{lum} , is related to the optical power by [12]

$$\phi_{lum} = 683\frac{lm}{watt}\int ER(\lambda) * EL(\lambda)d\lambda \tag{2.9}$$

Where $EL(\lambda)$ is the electroluminescence spectral power (or radiant intensity), 683 $\frac{lm}{watt}$ is a normalization factor and $ER(\lambda)$ is the eye response curve. The photopic eye sensitivity function, $ER(\lambda)$, was introduced by the International Commission for Illumination (Commission Internationale de I'Eclairage, CIE), for point like sources with the viewing angle of 2° in 1931 (see Figure 2.5). The human eye cannot detect all the wavelengths equally: for example UV and infrared are invisible to the eye. This function demonstrates how well the human eye can capture emitted radiation. Therefore, for a corrected luminous flux, the overlap of the spectrum emitted by the source with the eye response curve should be taken to describe how the source appears to the eye.

The total luminous flux ϕ_{lum} leaving the device without being waveguided is given by Greenham et.al [14]

$$\phi_{lum} = \int_{0}^{\frac{\pi}{2}} 2\pi L\, cos\theta sin\theta d\theta \tag{2.10}$$

Where L is the flux per unit solid angle and θ is the angle from the normal which the light is detected. Applying the trigonometric identity $cos\theta sin\theta = \frac{1}{2}\sin 2\theta$, Equation 2.10 becomes

$$\phi_{lum} = \int_{0}^{\frac{\pi}{2}} 2\pi L \frac{1}{2} sin2\theta d\theta$$

$$\phi_{lum} = \pi L \left[-\frac{1}{2}\cos 2\theta\right]_{0}^{\frac{\pi}{2}}$$

$$\phi_{lum} = \pi L \tag{2.11}$$

If L is in cdm^{-2} unit, then

$$\phi_{lum} = \pi L \times A_{emission} \tag{2.12}$$

Where $A_{emission}$, is the area of light emission source, therefore ϕ_{lum} will be in lumens (lm). For a light emitting device, the luminous flux is given by Equation 2.9 while the optical power, P_{out} , emitted by a light source is given by an integration over all wavelengths by

$$P_{out} = \int EL(\lambda) d\lambda \tag{2.13}$$

The issue here is not having an absolute measurement of the radiant intensity. Available data is a relative measurement of normalized EL. However, the ratio of Equations 2.9 and 2.13 are valid and is yield:

$$\frac{\phi_{lum}}{P_{out}} = 683 \frac{lm}{watt} \frac{\int ER(\lambda) * EL(\lambda) d\lambda}{\int EL(\lambda) d\lambda} \tag{2.14}$$

Using the Equation 2.12 , the optical power , P_{out}, is given by;

$$P_{out} = \frac{L * \pi * A_{emission}}{683 \frac{lm}{watt}} * \frac{\int EL(\lambda) d\lambda}{\int ER(\lambda) * EL(\lambda) d\lambda} \tag{2.15}$$

The number of photons emitted by device is related to optical power by;

$$P_{out} = n_{ph} h\upsilon = \frac{n_{ph} hc}{\lambda} \tag{2.16}$$

Where h is Plank's constant, υ is the frequency, n_{ph} is the number of photons per unit time, c is the speed of light and λ is the wavelength. Instead of having a single wavelength, there are a range of wavelengths for recorded radiant intensity. Therefore an average wavelength is needed as follows:

$$\lambda_{av} = \frac{\int EL(\lambda)\lambda d\lambda}{\int EL(\lambda) d\lambda} \tag{2.17}$$

Substituting Equations 2.15 and 2.17 in 2.16 and rearranging:

$$n_{ph} = \frac{L * \pi * A_{emission}}{683 \frac{lm}{watt}} * \frac{\int EL(\lambda)\lambda d\lambda}{\int ER(\lambda) * EL(\lambda) d\lambda} \tag{2.18}$$

The number of electrons per second injected into the device, n_e is given by:

$$n_e = \frac{I}{e} \tag{2.19}$$

Where e is charge for an electron $1.6 \times 10^{-19}\ c$ and I is current (A). The EQE can then be found as the ratio of photons per second emitted by device in the viewing direction to the number of injected electrons per second to the device:

$$EQE = \frac{n_{ph}}{n_e} \tag{2.20}$$

2.5.2 Colourimetry

The emitted "colour" of our devices is described by colour-matching functions and a chromaticity diagram by the CIE. Figure 2.6.a shows the three colour-matching functions, $\bar{x}(\lambda)$, $\bar{y}(\lambda)$, and $\bar{z}(\lambda)$ which represent red, green and blue light respectively. These functions are dimensionless and result from the colour of light being described using these three variables. For a given colour spectral density, $P_{spectrum}(\lambda)$, the overlap of the spectral density with each of the colour-matching functions gives the degree of each function required to match the colour of the spectrum as follows:

$$X = \int \bar{x}(\lambda)\, P_{spectrum}(\lambda) d\lambda \tag{2.21}$$

$$Y = \int \bar{y}(\lambda)\, P_{spectrum}(\lambda) d\lambda \tag{2.22}$$

$$Z = \int \bar{z}(\lambda)\, P_{spectrum}(\lambda) d\lambda \tag{2.23}$$

Where X, Y, and Z are known as the tristimulus values which give the stimulation of power of each of the three primary colours red, green and blue needed to match the colour of $P_{spectrum}(\lambda)$.

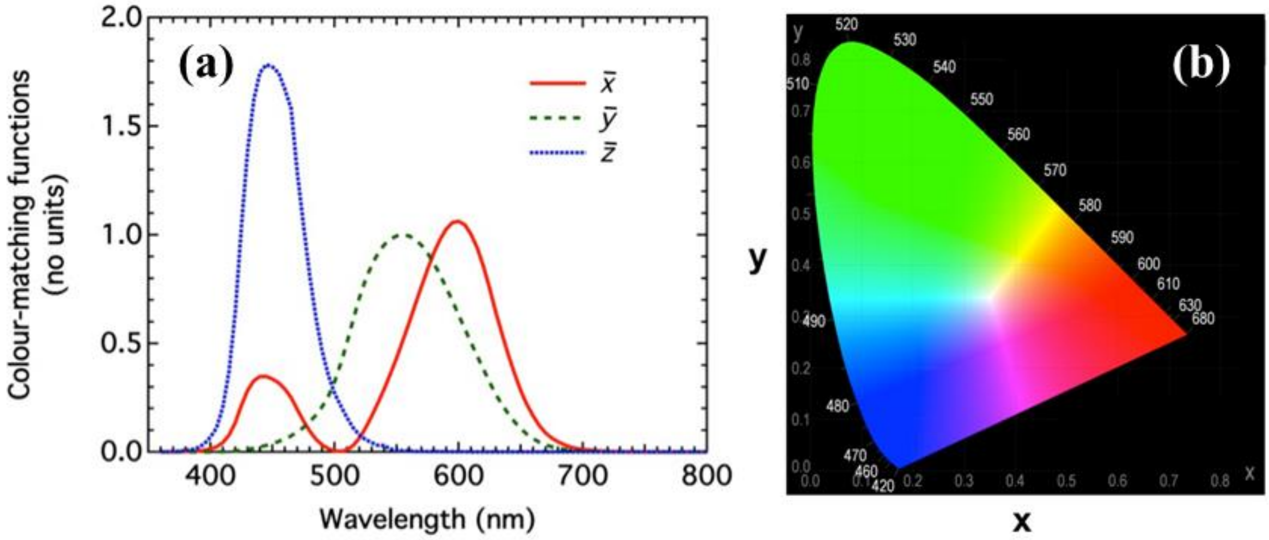

Figure 2. 6 a) CIE 1931 colour-matching functions $\bar{x}(\lambda)$, $\bar{y}(\lambda)$, and $\bar{z}(\lambda)$ which represent red, green , blue light respectively as a function of wavelength, note that the green colour-matching function $\bar{y}(\lambda)$, is identical to the eye response curve [15]. b) chromaticity diagram representing the possible colours the human eye can perceive with x and y co-ordinates [15].

The light source colour can also be represented as co-ordinates on a chromaticity diagram which shows the spectrum of colours visible by the human eye. The chromaticity co-ordinates are given from three tristimulus values as follows

$$x = \frac{X}{X + Y + Z} \tag{2.24}$$

$$y = \frac{Y}{X + Y + Z} \tag{2.25}$$

$$\begin{gathered} z = \frac{Z}{X + Y + Z} \\ z = 1 - x - y \end{gathered} \tag{2.26}$$

The x and y co-ordinates can then be displayed on a chromaticity diagram (see Figure 2.6.b) and they are normally referred to as the “CIE co-ordinates”. In the work described in this thesis, CIE co-ordinates are given by the standard Luminance Colorimeter camera [12].

2.5.3 Standard OLED characterisation

Completed devices were encapsulated in a glovebox with water and oxygen concentration levels < 0.1 ppm, with a glass cover using UV cured epoxy resin and an adhesive desiccant. For electrical connection, the entire substrate was held securely with the six cathodes connected via a clamp with ribbon cables (see Figure 2.7). Voltage-current-luminance (V-I-L) was performed using a Keithley 2400 source meter by applying a voltage (V) on the pixel under test and measure the corresponding current (I) through that device. Simultaneously, the light emitted by the pixel was collected by a Topcon Luminance Colorimeter BM-7A, with standard industry calibration. The applied voltage and measurements were controlled by a fully automated process using a computer and Labview software programing. Alternatively the Luminance Colorimeter camera was replaced by an ASEQ LR1 mini-spectrometer to measure the EL spectra of each pixel.

EQE and colourimetry are two important parameters for OLEDs which were explained in Section 2.5.2. However there are some other parameters which calculated from current (I) and brightness (L) as follows

- Current density (J) – current (I) per unit area of emission (A) which normally calculated in unit mAcm^{-2}.
- Current efficiency (LJ^{-1}) –amount of brightness (L) per unit current density (J). It is given by dividing brightness (cdm^{-2}) by current density (Am^{-2}). Therefore the current will be cdA^{-1}.
- Power efficiency (η^*) –the ratio of luminous flux (ϕ_{lum}) divided by optical power P_{out} . Presented in lmwatt^{-1}.

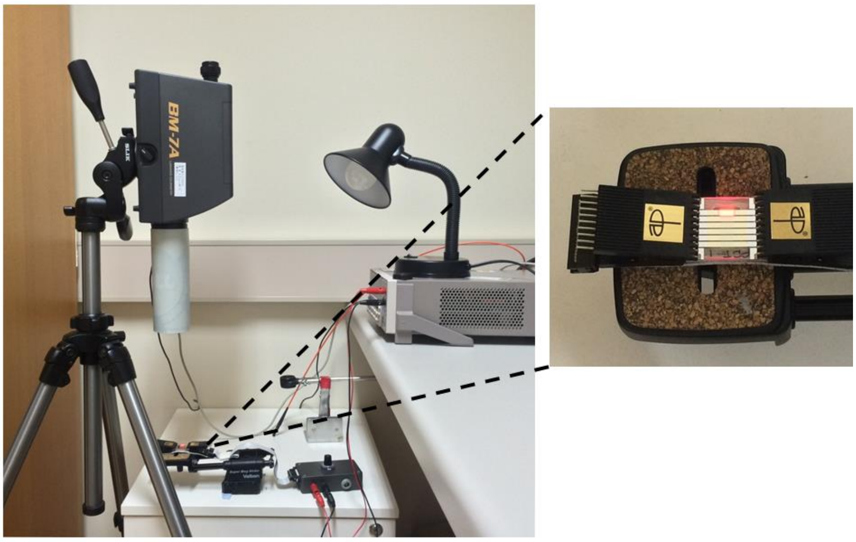

Figure 2.7 Two photographs showing the experimental set-up for OLED testing utilised at the CSIRO test facility.

2.5.4 Standard LEFET characterisation

Completed LEFET devices were encapsulated with a thick layer of Cytop, CTL-809 M (solvent: CTSolv.180) from Asahi Glass Japan. They were then transferred to the testing glove box where electrical and optical characterisation was performed using an Agilent B1500A Semiconductor Analyser on a SA-6 Semi-Automatic Probe Station. The light output from devices was simultaneously measured during operation by a calibrated photomultiplier tube (PMT), a Hamamatsu H10721-20, positioned directly over the device with a fixed distance (see Figure 2.8). The PMT and the three probes were individually connected electrically to the Agilent which was positioned outside the glove box. The source-drain current of the LEFET and photocurrent from PMT were recorded for electrical and optical characterisation.

2.5.4.1 Optical characterisation

In order to convert the PMT photocurrent to brightness the PMT was calibrated using an OLED fabricated by commercially available emissive layer super yellow. The reason for choosing an OLED is the easier encapsulation process and possibility for brightness measurements with luminance meter outside the glove box. The performance of the encapsulate OLED was then measured at different applied voltages once with luminance meter (Konica Minolta LS100) and again with PMT fixed for certain distance and gain. The PMT photocurrent as a function of brightness were then plotted in order to calibrate the PMT. The slope of the calibration curve was then used to find the brightness of a device with known PMT current. At fixed gain of 0.4 and for OLED area of 0.92 mm^2 the slope of the calibration is $69.0\ nA\ cd\ m^{-2}$ and so;

$$1 cd\ m^{-2} \approx 69.0\ nA \tag{2.27}$$

The calibration can be adjusted for the difference in emission area of the LEFET and OLED as;

$$1 cd\ m^{-2} \approx 69.0\ nA \times \frac{Area_{emission}(LEFET)}{Area_{emission}(OLED)} \tag{2.28}$$

The conversion between PMT current in nA and brightness (L) in $cd\ m^{-2}$ is then;

$$L\ (cd\ m^{-2}) = PMT\ current\ (nA) \times \frac{Area_{emission}(LEFET)}{Area_{emission}(OLED)} \times \frac{1}{69.0\ nA\ cd\ m^{-2}} \tag{2.29}$$

The EQE can then be determined as explained in Section 2.5.1.

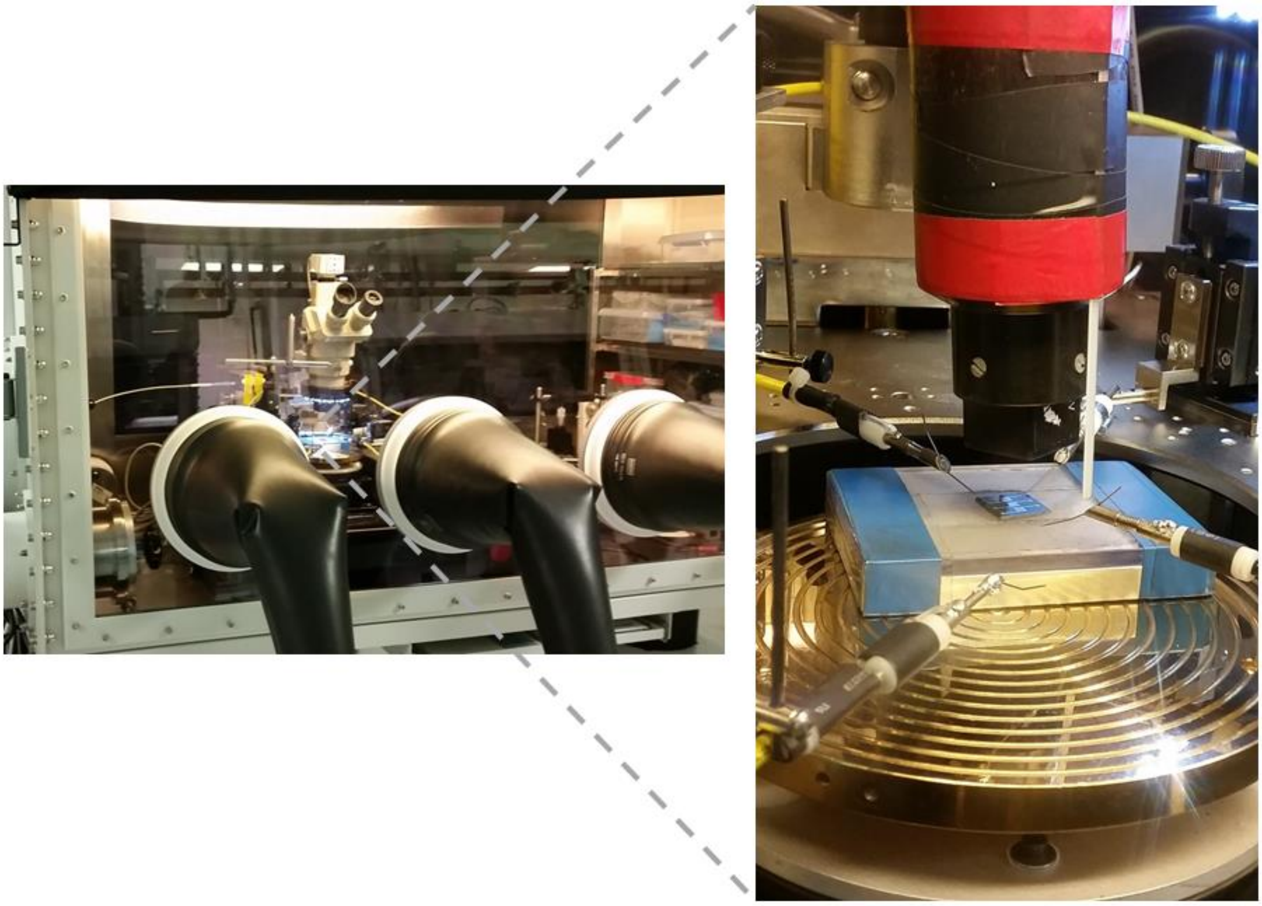

Figure 2.8 Photographs showing the experimental setup for LEFET testing utilised at the COPE test facility.

2.5.4.2 Electrical characterisation

LEFETs were modelled using standard MOSFET (metal-oxide-semiconductor field effect transistor) equations which were originally developed for their inorganic counterparts [16]. The equations originated by taking into account the applied fields within the device. The model is applicable for organic devices as well as inorganic devices since it does not take into account any microstructural details. There are important device parameters of interest such as majority carrier mobility, μ, the ON/OFF ratio and threshold voltage, V_t, which will be explained below.

There are two different operation regimes for LEFETs. For an n-type device operating in the linear regime, $V_{DS} < V_G - V_t$ [16],

$$I_{DS} = \frac{W}{L}\mu C[(V_G - V_t)V_{DS} - \frac{{V_{DS}}^2}{2}] \tag{2.30}$$

where I_{DS} is the source-drain current, W and L are the length and width of the transistor channel respectively and C is the capacitance of the dielectric layer which can be determined by a series of organic and inorganic dielectric layers. In the saturation regime, where $V_{DS} \geq V_G - V_t$ [16],

$$I_{DS} = \frac{W}{L}\frac{\mu C}{2}(V_G - V_t)^2 \tag{2.31}$$

These equations can be used for p-type devices with a sign difference respective of the opposite polarity of the applied voltages. In the work details in this thesis, the LEFET mobility was determined from the transfer characteristics in the saturation regime. In a small threshold voltage, the mobility in the saturation regime is given by

$$\mu = \frac{2L}{WC}\left(\frac{\sqrt{\partial I_{DS}}}{\partial V_G}\right)^2 \tag{2.32}$$

The threshold voltage, which is the minimum gate voltage that must be applied to switch the device ON, can be determined by finding the x intercept of the $\sqrt{I_{DS}}$ vs V_G plot.

The ON/OFF ratio is a parameter which shows the switching capability of a LEFET. It is the ratio between the maximum current measured when the device is switched ON and the minimum current of the transfer characteristics.

In this chapter, the methodologies and basic principles for characterising OLED and LEFET materials and devices were described. In particular, dendritic phosphorescent materials suitable for OLEDs, where appropriate additional experimental and theoretical details will be provided in subsequent Sections. In the next chapter, the first of the results will be described concerning a systematic study of a basic dendritic dendrimer structure consisting of Iridium complex with biphenyl dendron.

References

[1] J. Li, Y. Zhao, H.S. Tan, Y. Guo, C.-A. Di, G. Yu, Y. Liu, M. Lin, S.H. Lim, Y. Zhou, A stable solution-processed polymer semiconductor with record high-mobility for printed transistors, Scientific reports, 2 (2012).
[2] R. Joseph, Lakowicz. Principles of fluorescence spectroscopy, in, Springer, 2006.
[3] G.A. Crosby, J.N. Demas, Measurement of photoluminescence quantum yields. Review, The Journal of Physical Chemistry, 75 (1971) 991-1024.
[4] N. Greenham, I. Samuel, G. Hayes, R. Phillips, Y. Kessener, S. Moratti, A. Holmes, R. Friend, Measurement of absolute photoluminescence quantum efficiencies in conjugated polymers, Chemical physics letters, 241 (1995) 89-96.
[5] P.E. Shaw, Measurements of exciton diffusion in conjugated polymers, in, University of St Andrews, 2009.
[6] J. Woollam, Guide to using WVASE32 JA Woollam co, in, Inc, 2002.
[7] D. Yokoyama, Molecular orientation in small-molecule organic light-emitting diodes, Journal of Materials Chemistry, 21 (2011) 19187-19202.
[8] W. Brütting, J. Frischeisen, T.D. Schmidt, B.J. Scholz, C. Mayr, Device efficiency of organic light-emitting diodes: Progress by improved light outcoupling, physica status solidi (a), 210 (2013) 44-65.
[9] K.H. Kim, C.K. Moon, J.H. Lee, S.Y. Kim, J.J. Kim, Highly Efficient Organic Light-Emitting Diodes with Phosphorescent Emitters Having High Quantum Yield and Horizontal Orientation of Transition Dipole Moments, Advanced Materials, 26 (2014) 3844-3847.
[10] L. Zhao, T. Komino, M. Inoue, J.-H. Kim, J.C. Ribierre, C. Adachi, Horizontal molecular orientation in solution-processed organic light-emitting diodes, Applied Physics Letters, 106 (2015) 063301.
[11] M.J. Jurow, C. Mayr, T.D. Schmidt, T. Lampe, P.I. Djurovich, W. Brütting, M.E. Thompson, Understanding and predicting the orientation of heteroleptic phosphors in organic light-emitting materials, Nature materials, (2015).
[12] E.F. Schubert, Light-Emitting Diodes (2006), E. Fred Schubert, 2006.
[13] Bureau International des Poids et Mesures. The International System of Units (SI), 8thEdition (Organisation Intergouvernementale de la Convention du Mètre, 2006), in.
[14] N.C. Greenham, R.H. Friend, D.D. Bradley, Angular Dependence of the Emission from a Conjugated Polymer Light-Emitting Diode: Implications for efficiency calculations, Advanced Materials, 6 (1994) 491-494.
[15] K. Tandy, Active channel field-effect transistors: Towards high performance light emitting transistors, (2014).
[16] Z. Bao, J. Locklin, Organic field-effect transistors, CRC press, 2007.

Chapter 3

Highly Efficient Solution-Processable Dendrimer OLEDs

3.1 Introduction

The development of organic semiconductors in last three decades is widely viewed as the next technology wave in optoelectronics, and it is one of the most exciting fields of research not only in science but also industry. The ability of organic semiconductors to combine tunable optoelectronic properties with the desire for much simpler processing compared to their inorganic counterparts has made them formidable competitors in the market. Over the past decade, organic light emitting diodes became a promising candidate for flat panel display technology due to their high efficiency, low driving voltage, light weight, and low cost of both materials and processing. Among all materials investigated in OLEDs, phosphorescent materials have gained specific attention due to their potential for 100% internal quantum efficiency by harvesting both singlet and triplet excitons [1-3]. So far, iridium (III) complexes have been the most promising candidates, offering high efficiency, relatively short excited state lifetimes, and colour tunability [4-9]. Iridium (III) complexes have been demonstrated in the three different categories of small molecules [10, 11], polymers [12-14] and dendritic architectures [15-18]. Devices based on small molecules have shown less potential due to the need for high temperature high vacuum deposition techniques. Although polymers are promising with highly cost effective processing techniques such as spin coating and inkjet printing [19], any attempts to tune processing often leads to undesirable changes in the electronic and emissive properties of the resultant devices. Using dendritic structures allows independent control over intermolecular interactions as well as emissive properties. There have been several reports on phosphorescent dendrimer OLEDs in the last decade [15-18, 20-23]. It is important to simplify fabrication, in line with the desire for mass production large area displays. Previous attempts to make efficient OLEDs out of neat film Ir(III) core complexes have shown poor efficiencies due to the strong interaction between chromophores which led to quenching the luminescence [24].

This Chapter describes the full characterisation of a simple dendritic Ir (III) complex and the work towards improving the performance of single layer host free OLEDs formed by spin-coating. The results are shown to be comparable with those of devices making use of the same material in a guest-host system. The definition of the guest-host system has previously been provided in Chapter 1.

3.2 Material design and experimental methods

Materials used in the work presented in this Chapter are shown in Figure 3.1. The first generation dendrimer (G1 Ir(ppy)$_3$) contains a fac tris(2-phenylpyridine) iridium core, phyenyl based dendrons and 2-ethylhexyloxy surface groups (see Figure 3.1.a) and was used as a dopant. In addition, two small molecules commercially available from Lumtec, 4,4’-N,N’-dicarbazolyl-biphenyl (CBP) and 2,2',2"-(1,3,5-Benzinetriyl)-tris(1-phenyl-1-H-benzimidazole) (TPBi) were used as host and electron transport materials, respectively (see Figure 3.1.b and c).

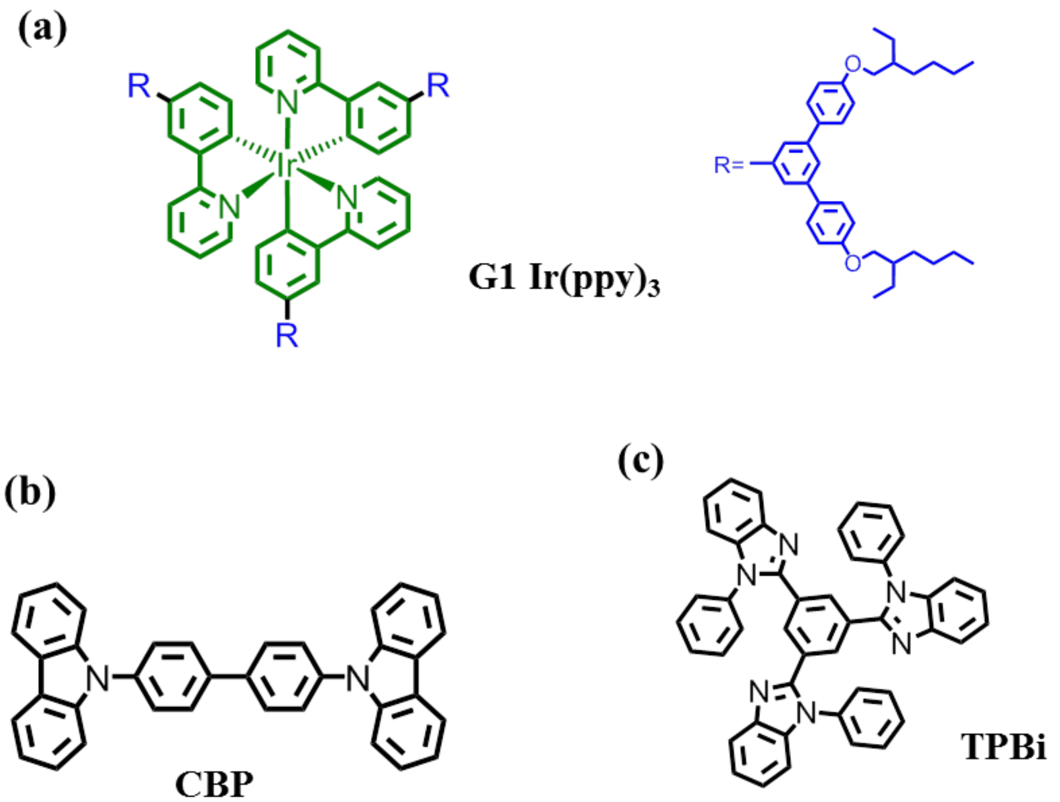

Figure 3.1 The chemical structures of a) G1 Ir(ppy)$_3$, b) CBP, and c) TPBi.

The dopant shown in Fig 3.1 was subject to a comprehensive set of photo-physical measurements which were performed as detailed in Chapter 2 where films were spin cast from 20 mg/ml concentration with a 20 wt% dopant ratio in blends. The 20 wt% fraction was chosen because it is equivalent to 6 wt% Ir(ppy)$_3$ which has been shown to be optimal in evaporated OLEDs using a CBP host [2]. The photo-physical measurements included: absorption and PL spectra; PLQY values; and Lifetime values.

The device structure used to test the dendritic dopant is shown in Figure 3.2.a and had pre-patterned indium- tin oxide (ITO(10 Ω/sq)) (170 nm). Substrates were pre-cleaned with isopropanol and water and then treated with UV-ozone for 15 minutes at 25° C immediately prior to use. PEDOT: PSS then was spin coated onto the substrates to a thickness of 30 nm and annealed for 15 min at 150° C. The PEDOT: PSS was used to enhance hole injection into the device, better matching the energy levels of emissive layer (see Figure 3.2.b). Devices were then transferred into a glovebox where the emissive layers (neat or blend) were deposited on the substrates by spin-coating. For the neat films, the solvent used was chlorobenzene, and chloroform was used for the blends at a concentration of 20 mg/ml with a dopant concentration of 20 wt%. Chlorobenzene is more suitable as a solvent for these materials since chloroform causes quenching of the luminance due to chemical degradation. For the blends, however, there was no option since CBP has a better solubility in chloroform. The thicknesses of the emissive layers were kept consistent in all devices.

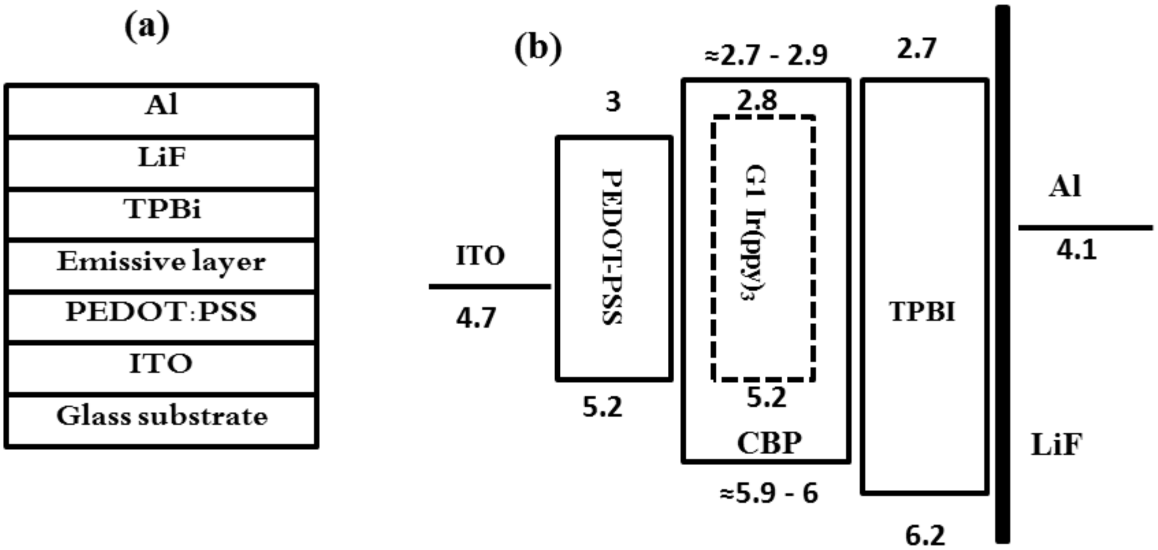

Figure 3.2. a) Device structure, b) energy diagram for different layers. The HOMO and LUMO of TPBi and CBP were taken from literature respectively [25, 26]. The work function for metals were taken from original material sheets provided by CSIRO, the energy level of G1 Ir(ppy)$_3$ were obtained from PESA measurements as explained in Chapter 2.

The devices were completed with the thermal evaporation of the cathode using shadow masks to deposit successive layers of TPBi, LiF, and Al in a vacuum chamber with a base pressure of approximately 5×10^{-6} mbar. The deposition rate for the TPBi layer was maintained at approximately 1 Å/s. After the organic layer was deposited, the cathode layers, LiF (1 nm) and Al (100 nm), were deposited using a second shadow mask without breaking the vacuum. Cathode layers were also selected according to the appropriate energy level off-sets of the materials in the device. The thicknesses of layers were measured using a Dektak confirming 50nm for the emissive layer. Completed devices were transferred under an inert atmosphere from the vacuum chamber to a glovebox (water and oxygen concentration levels < 0.1 ppm) for encapsulation with a glass cover using UV cured epoxy resin and an adhesive desiccant. Encapsulated devices were then transferred outside the glovebox for characterisation as detailed in Chapter 2.

3.3 Photo-physical properties

The UV-visible absorption spectra of G1 $Ir(ppy)_3$ were measured in solution (solid line), in neat films (dash line), and in CBP blend films (dotted line) as it shown in Figure 3.3. In all cases intense absorption was observed in the range of 250-320 nm, which is due to the singlet-singlet $\pi - \pi^*$ transition of the ligand. The weaker absorption extends from 330 nm to 500 nm which is due to metal to ligand charge transfer (MLCT) transitions. It has been reported that the relative intensity of the absorption between 250-320 nm in first generation of $Ir(ppy)_3$ is approximately twice as a large as $Ir(ppy)_3$ because of the additional contribution to the absorption from the biphenyl dendrons [27].

The photoluminescence (PL) spectrum of G1 $Ir(ppy)_3$ was then measured for degassed solutions, neat film, and films with the CBP blend (see Figure 3.3). Although the shape of PL spectra are almost identical, the red shifted maximum peak, broader emission, and the less pronounced shoulder were noted moving from solutions to the blends and then neat films respectively. This can be attributed to a decrease in the conformational freedom in the solid-state. To probe the role of inter-chromophore interactions (both intra-and-interchain), and photophysical properties more closely, the PLQY and PL decay (see Figure 3.4) were measured for these samples as detailed in Chapter 2. The PLQY value in degassed solution was 81% and the PL decay lifetime was mono exponential (see Figure 3.4). This evidence supports the idea that there are no strong interchain interchromophore interactions that lead to substantial photoluminescence quenching in solution.

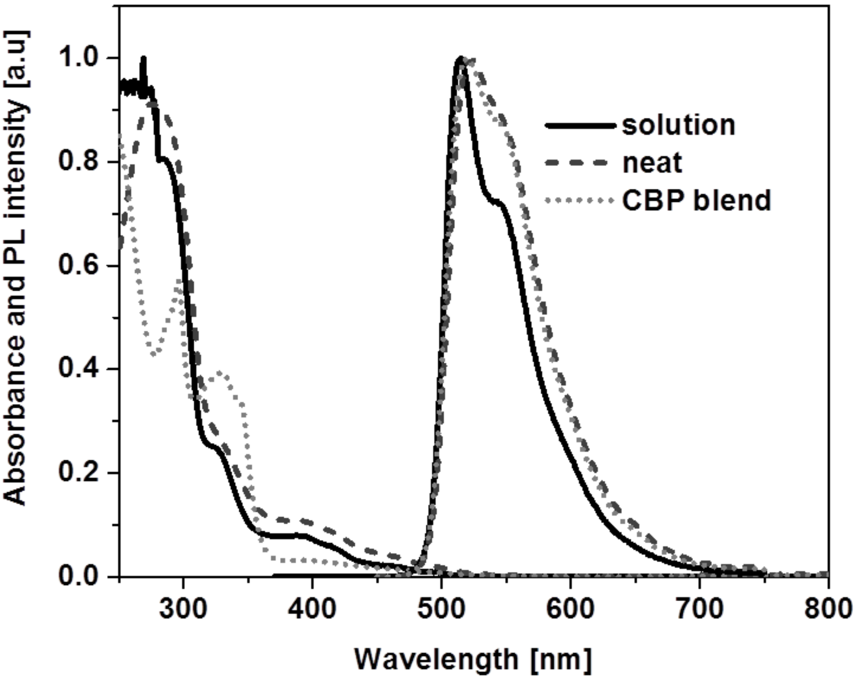

Figure 3.3 Absorption and PL spectrum for G1 Ir(ppy)$_3$ in solution (solid line), in neat film (dash line), and in CBP blend film (dot line), the samples were excited at a wavelength of325 nm for PL measurements.

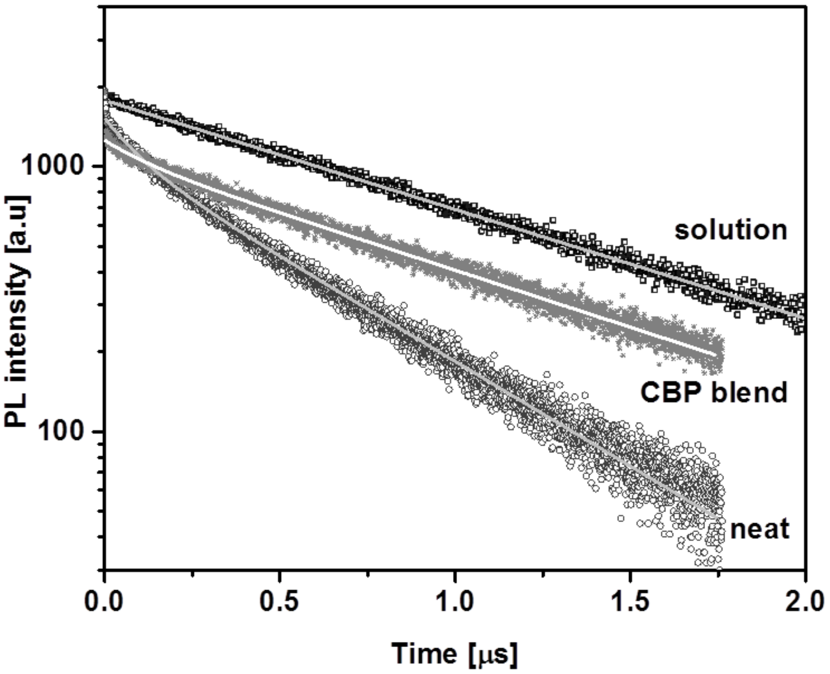

Figure 3.4 Photoluminescence lifetime measurement (TCSPC) for G1 Ir(ppy)$_3$ in a degassed solution (square), in neat film (circle), and in CBP blend (star). The samples were excited by a 372 nm LED and the emission was detected at 515 nm (peak).

In moving from solution to the solid-state there was a decrease in PLQY from 81% to 50%. Moreover the biexponential decay (see Figure 3.4) indicated that there was more than one emissive species present in the complex. The biexponential decay amplitudes for the neat film were significantly lower than in solution, implying that intermolecular interactions were responsible for the quenching and also the slight red shift of PL spectrum. The PL decay in the neat film was much faster than in solution, which indicated that additional non-radiative decay of the emissive triplet state prevailed in the neat film.

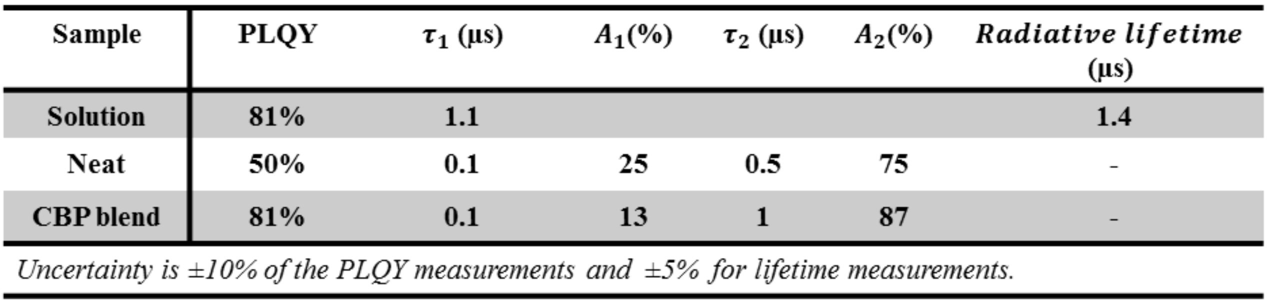

Sample	PLQY	τ_1 (μs)	A_1(%)	τ_2 (μs)	A_2(%)	$Radiative\ lifetime$ (μs)
Solution	81%	1.1				1.4
Neat	50%	0.1	25	0.5	75	-
CBP blend	81%	0.1	13	1	87	-

Uncertainty is ±10% of the PLQY measurements and ±5% for lifetime measurements.

Table 3.1 Summary of PLQY and PL decay values for G1 $Ir(ppy)_3$ in solution, neat film, and CBP blend.

The film PLQY of the CBP blend increased and was similar to the solution PLQY. Moreover, lifetime decay measurements showed a higher ratio of slower components with relatively similar lifetimes to the mono-exponential component in solution. Both these values were consistent with reduced quenching due to the expected introduction of space between chromophores in comparison with the neat film. However the fast decay component of 0.1 μs (with a relative amplitude of 13%) was still observed along with a dominant lifetime of 1 μs (with a relative amplitude of 87%), which suggested that there were still interchromophore interactions that had not been completely controlled. All the PLQY and PL decay parameters are summarized in Table 3.1. The radiative lifetime for optically dilute solutions was calculated according to Equation 1.3 and was of the order of microseconds, confirming the emission from a triplet state. These values are in agreement with the previous study [27].

3.4 Device performance

Figure 3.5 shows typical electrical characteristics of devices using neat and blend emissive layers (henceforth referred to as “neat devices” and “blend devices” respectively). Neat devices showed improved injection, which is noticeable from the abrupt increase in current density in comparison with the blended devices. Another difference between these two devices was the turn on voltages which were 3 V and 4.8 V for neat and blend respectively. This confirmed improved charge injection in the neat devices which could be attributed to better energy level matching between PEDOT:PSS and Ir (ppy)$_3$. However the blended device was superior as the blends provided extra space between chromophore cores which could lead to less interaction and quenching. Nevertheless, using a host material like CBP would be predicted to have a negative impact on the charge transport properties of the emissive layer which is evident in these results with an order of magnitude lower current density in blend devices.

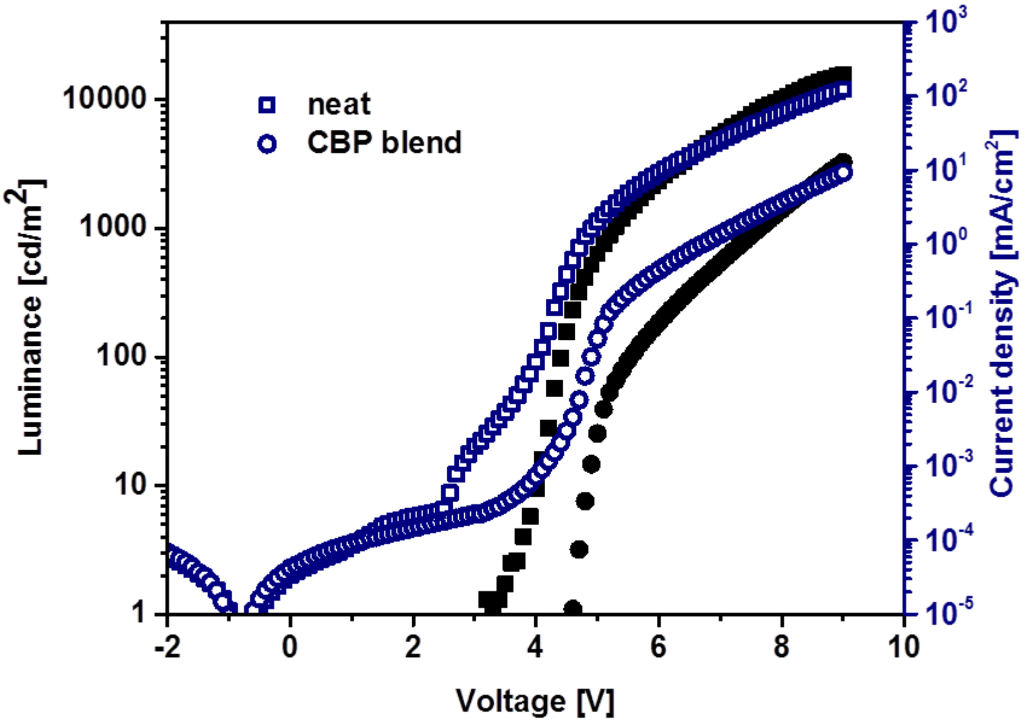

Figure 3.5 Current density and luminance characteristics for neat and CBP blend devices. The square represents the neat films while the circle represents the blends. Open grey colour show current density and solid black colour represents the luminance.

The electroluminescence (EL) spectra of both devices are shown in Figure 3.6.a. The higher wavelength shoulder in the neat devices is less pronounced which suggests less freedom in comparison with blended devices or potentially different morphology in neat and blend films. An image of a working device and CIE co-ordinates are shown in Figure 3.6.b and c respectively. The CIE co-ordinates for neat and blended devices overlapped as clearly shown in Figure 3.6.c (0.340, 0.630) confirming the green emission which was evident in the EL spectrum.

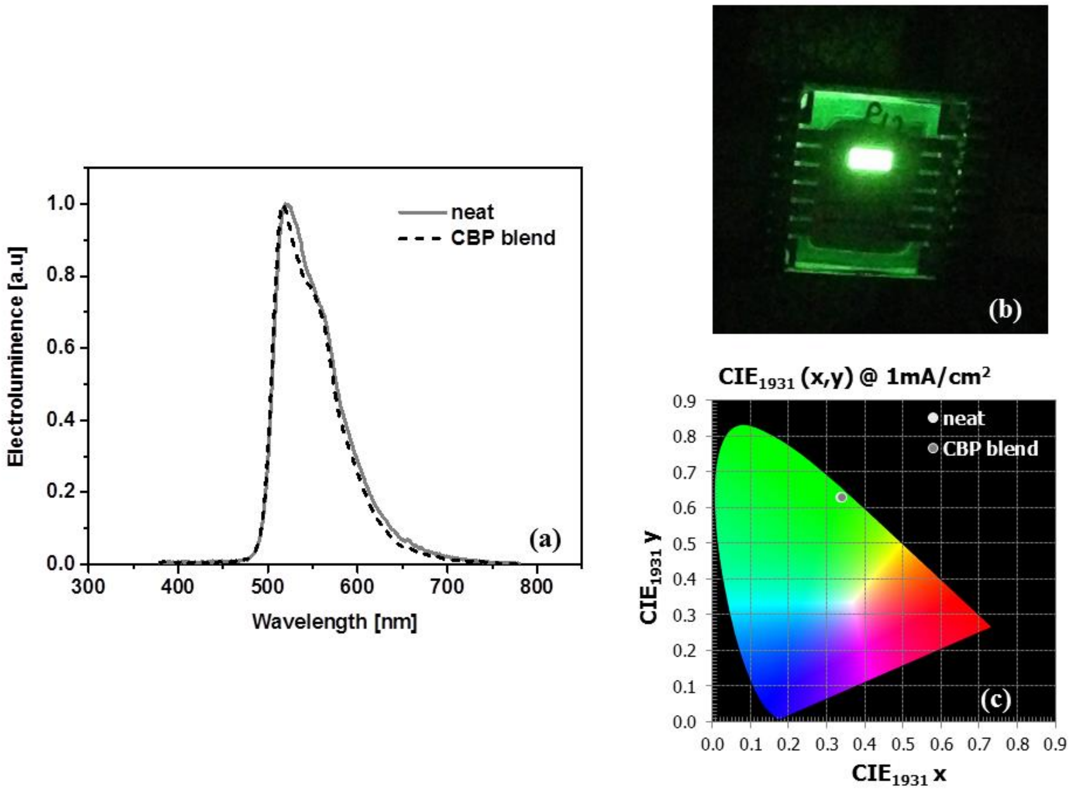

Figure 3.6. a) EL spectrum for neat and CBP blend devices, b) a close up of the working device, c) the overlapped CIE co-ordinates of both devices.

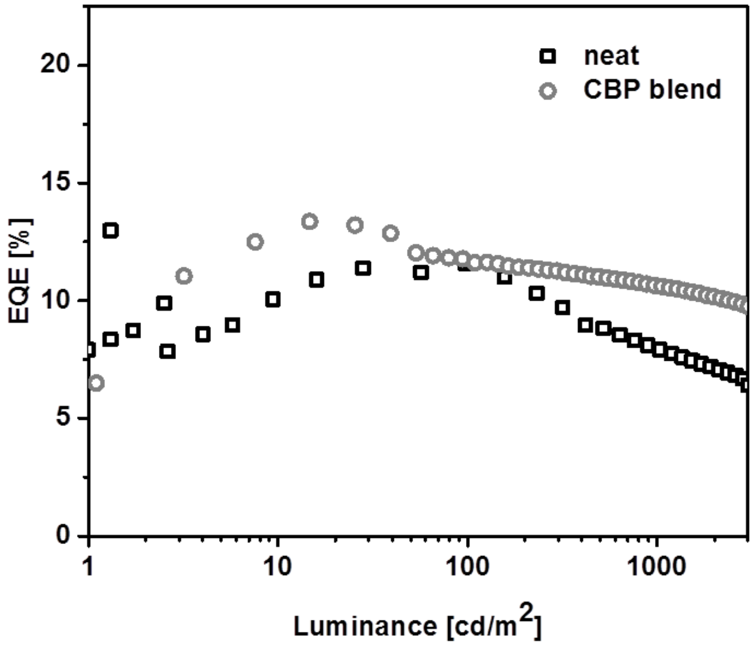

Figure 3.7 EQE values for neat and CBP blend devices.

The slightly improved performance of neat devices is likely due to their morphology and packing since CBP generally lacks good film forming qualities. The external quantum efficiencies for both devices were calculated as explained in Chapter 2, and are shown in Figure 3.7. Both devices reached similar EQEs with the blend devices showing a slightly higher EQE for luminance values below 100 cd/m2. Similar work has been reported by Markham et al [24] without an electron transport layer for neat films of the material and demonstrated much lower EQEs of about 0.1%. One of the reasons for the improved performance of neat devices in this study could be the role of TPBi not only as an ETL, but also as a hole blocking layer which would lead to better balance between charge carriers leading to higher recombination rate. The EQEs for both devices were ~12% at 100 cd/m2 brightness. However, the EQE of neat devices decreased abruptly due to triplet-triplet annihilation in comparison with the blend devices where the interaction between cores was suppressed.

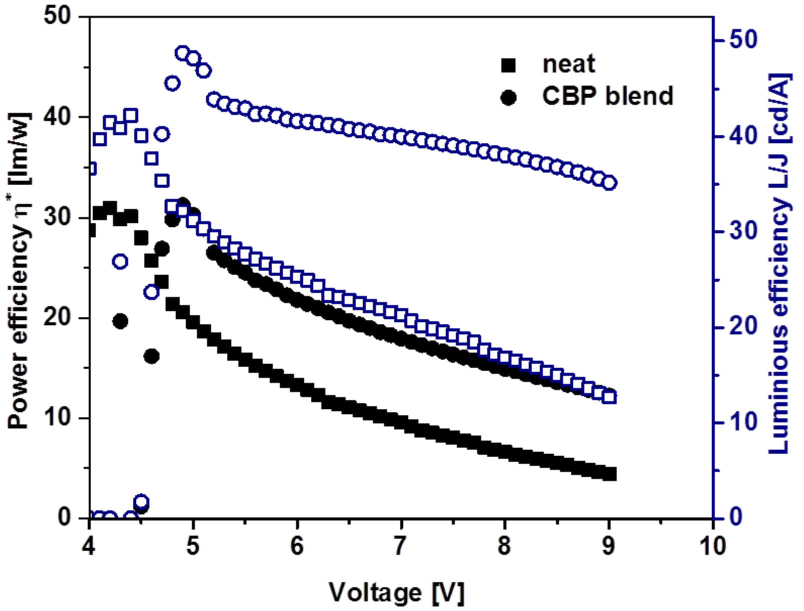

Figure 3.8 Power efficiency for both neat and CBP blend devices.

A similar maximum power efficiency (see Figure 3.8) of about 31 lm/W was observed at 28 cd/m^2 and 15 cd/m^2 for neat and blend devices which corresponded to current densities of 0.068 mA/cm^2 and 0.030 mA/cm^2 respectively. However blend devices had a higher power efficiency in comparison with the neat devices, suggesting reduced triplet-triplet annihilation. A summary of the device results is presented in Table 3.2.

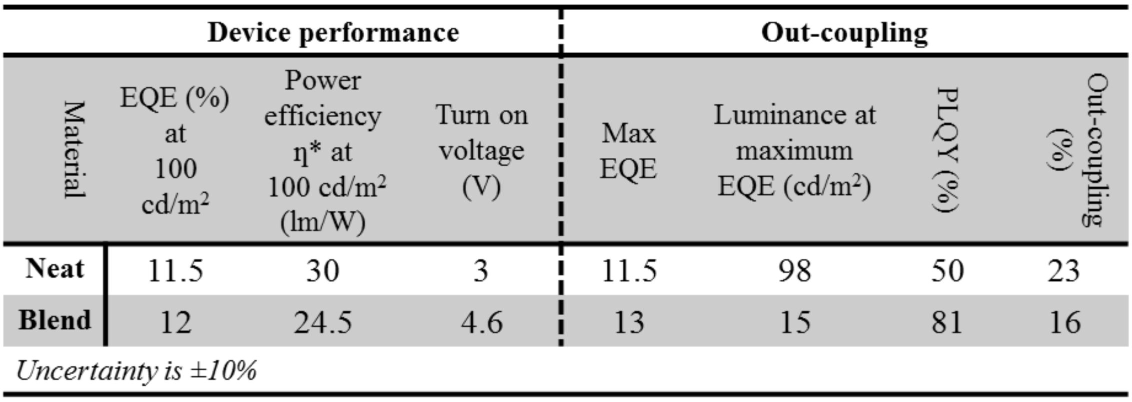

Device performance				Out-coupling			
Material	EQE (%) at 100 cd/m²	Power efficiency η* at 100 cd/m² (lm/W)	Turn on voltage (V)	Max EQE	Luminance at maximum EQE (cd/m²)	PLQY (%)	Out-coupling (%)
Neat	11.5	30	3	11.5	98	50	23
Blend	12	24.5	4.6	13	15	81	16

Uncertainty is ±10%

Table 3.2 A summary of device performance parameters for neat and CBP blend emissive layers.

3.5 Dipole orientation

Conventionally, the EQE in an OLED is governed by the product of four different parameters:

$$\phi_{\mathrm{EQE}} = \phi_{\mathrm{escape}} \times \phi_{\mathrm{capture}} \times \phi_{\mathrm{spin}} \times \phi_{\mathrm{PLQY}} * 100\% \tag{3.1}$$

where ϕ_{spin} is related to the spin statistics for the formation of singlet or triplet excitons. Since Iridium complexes harvest both singlet and triplet emitters ϕ_{spin} is constant and equal to 1. Additionally, ϕ_{PLQY} is the photoluminensce quantum yield in the solid state which has different values between zero to 100% summarized in Table 3.1, $\phi_{capture}$ is the fraction of electrons and holes that recombine to form excitons, and ϕ_{escape} is the photon outcoupling factor which has been theoretically calculated to be 0.2 (20%) [28]. That said, the outcoupling (ϕ_{escape}) can be optimised using dipole orientation in the emissive layer as explained in Chapter 1. At the maximum EQE (with reasonable brightness) electrons and holes are completely balanced leading to an optimal recombination ($\phi_{capture}$) of 1, and as such the outcoupling (ϕ_{escape}) could be calculated for each device (see Table 3.2).

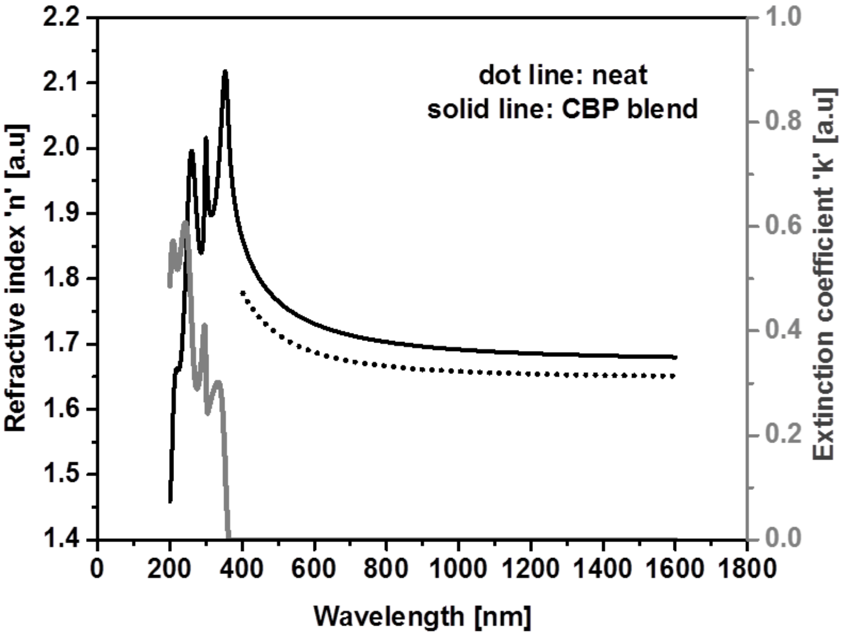

Figure 3.9 Refractive index and extinction coefficient for neat (dot line) and CBP blend (solid line) of G1 Ir(ppy)$_3$.

According to these calculations, neat devices reached above the theoretical limit with 23% outcoupling efficiency. This suggested the existence of horizontally oriented dipoles in the emissive layer. To check this hypothesis, ellipsometry and angular dependent PL measurements were performed in neat and blend devices. Figure 3.9 shows the refractive index, n, and extinction coefficient, k, for neat and CBP blend films of G1 Ir(ppy)$_3$ obtained from spectroscopic ellipsometry. The result obtained from ellipsometry measurement for neat film didn't provide imaginary component of the refractive index. This indicates random orientation as the orientation order parameter S (from Equation 2.8) was zero.

The blend with CBP appeared to be slightly more birefringent. The orientation order parameter, S was calculated using Equation 2.8 for a CBP blend with G1 Ir(ppy)$_3$ giving a value of 0.02 which is close to the isotropic value (S=0). This also suggested random orientation of the dipoles. However, the dipole orientation in spin coated samples was dominated by the morphology and spin coating conditions which suggested more investigation by angle dependent PL measurements were necessary. Angle dependent PL measurements were performed according to the methodology outlined in Chapter 2 for encapsulated samples. The optical constants from ellipsometry measurements were then used in the software program Setfos 4 to fit the experimental data (see Figure 3.10). The fit suggested that the G1 Ir(ppy)$_3$ in neat and blend films were isotropic which could be due to homoleptical orientation of G1 Ir(ppy)$_3$. However, the horizontal orientation of the emissive layer which is presumably the reason for the slightly high outcoupling (> 20 %) in neat devices could have also been dominated by the anisotropic orientation of the layer underneath. To further investigate this, the ellipsometry measurements were performed on a neat PEDOT: PSS layer. The results are shown in Figure 3.11 which details the real and imaginary parts of optical constants. This indicates that the anisotropic orientation of PEDOT: PSS which could affect the horizontal orientation of the spin casted emissive layer on top of it.

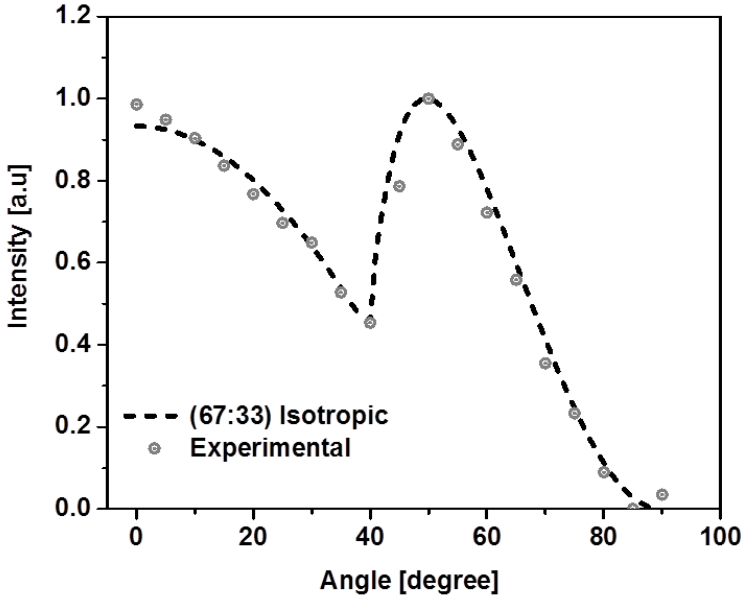

Figure 3.10 Experimental data (circles) and fitting (dash line) for angle dependent PL spectrum measurement.

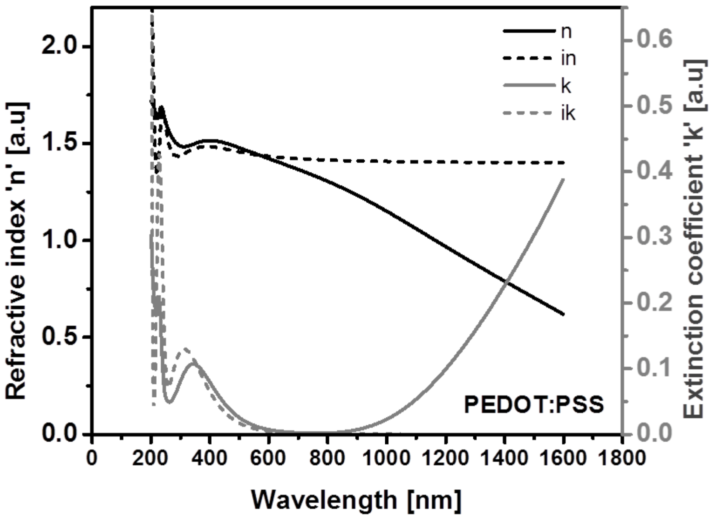

Figure 3.11 Refractive index and extinction coefficient for PEDOT:PSS.

3.6 Conclusion

This chapter details a full and systematic characterisation of a simple dendritic structure, G1Ir $(ppy)_3$, in solution, neat film and CBP blend. The results showed strong inter-chromophore interaction in the solid state which could be controlled with spacing the chromophore cores using a host material. Moreover device characteristics of neat and CBP blend were discussed. Although neat and blend devices showed similar EQEs, introducing space by host material (CBP) in blended devices may prevented triplet-triplet annihilation which enhanced device performance. Using an electron transport layer (TPBi) increased the efficiency in comparison with previous studies on the same material. This was due to the hole blocking role of TPBi as it provided more balance between electrons and holes and subsequently achieved a higher recombination rate. Although, the results indicated the intrinsic isotropic behaviour of G1 due to its homoleptical structure, horizontal orientation of spin casted emissive layers could be achieved by the presence of an anisotropic layer underneath which in the work described in this chapter was PEDOT: PSS.

In the next Chapter, the effect of changes in the number and type of dendrons will be discussed using a dendritic structure with the same chromophore core. A similar methodology will be used to provide a fair comparison. Furthermore, the effect of polymerisation will be studied as a route to potential candidates for solution processed materials suitable for scaling up to industrial usage.

References

[1] C. Adachi, M.A. Baldo, M.E. Thompson, S.R. Forrest, Nearly 100% internal phosphorescence efficiency in an organic light-emitting device, Journal of Applied Physics, 90 (2001) 5048-5051.
[2] M. Baldo, S. Lamansky, P. Burrows, M. Thompson, S. Forrest, Very high-efficiency green organic light-emitting devices based on electrophosphorescence, Applied Physics Letters, 75 (1999) 4.
[3] J. Wilson, A. Dhoot, A. Seeley, M. Khan, A. Köhler, R. Friend, Spin-dependent exciton formation in π-conjugated compounds, Nature, 413 (2001) 828-831.
[4] C. Adachi, R.C. Kwong, P. Djurovich, V. Adamovich, M.A. Baldo, M.E. Thompson, S.R. Forrest, Endothermic energy transfer: A mechanism for generating very efficient high-energy phosphorescent emission in organic materials, Applied Physics Letters, 79 (2001) 2082-2084.
[5] C. Adachi, M.A. Baldo, S.R. Forrest, S. Lamansky, M.E. Thompson, R.C. Kwong, High-efficiency red electrophosphorescence devices, Applied Physics Letters, 78 (2001) 1622-1624.
[6] M. Baldo, M. Thompson, S. Forrest, High-efficiency fluorescent organic light-emitting devices using a phosphorescent sensitizer, Nature, 403 (2000) 750-753.
[7] S.-C. Lo, C.P. Shipley, R.N. Bera, R.E. Harding, A.R. Cowley, P.L. Burn, I.D. Samuel, Blue phosphorescence from iridium (III) complexes at room temperature, Chemistry of materials, 18 (2006) 5119-5129.
[8] Y. You, S.Y. Park, Phosphorescent iridium (III) complexes: toward high phosphorescence quantum efficiency through ligand control, Dalton Transactions, (2009) 1267-1282.
[9] Y.C. Chiu, J.Y. Hung, Y. Chi, C.C. Chen, C.H. Chang, C.C. Wu, Y.M. Cheng, Y.C. Yu, G.H. Lee, P.T. Chou, En Route to High External Quantum Efficiency (∼ 12%), Organic True-Blue-Light-Emitting Diodes Employing Novel Design of Iridium (III) Phosphors, Advanced Materials, 21 (2009) 2221-2225.
[10] E. Holder, B.M. Langeveld, U.S. Schubert, New trends in the use of transition metal-ligand complexes for applications in electroluminescent devices, Advanced Materials, 17 (2005) 1109-1121.
[11] Q. Huang, K. Walzer, M. Pfeiffer, V. Lyssenko, G. He, K. Leo, Highly efficient top emitting organic light-emitting diodes with organic outcoupling enhancement layers, Applied physics letters, 88 (2006) 3515.
[12] X. Chen, J.-L. Liao, Y. Liang, M. Ahmed, H.-E. Tseng, S.-A. Chen, High-efficiency red-light emission from polyfluorenes grafted with cyclometalated iridium complexes and charge transport moiety, Journal of the American Chemical Society, 125 (2003) 636-637.
[13] A.J. Sandee, C.K. Williams, N.R. Evans, J.E. Davies, C.E. Boothby, A. Köhler, R.H. Friend, A.B. Holmes, Solution-processible conjugated electrophosphorescent polymers, Journal of the American Chemical Society, 126 (2004) 7041-7048.
[14] H. Zhen, C. Luo, W. Yang, W. Song, B. Du, J. Jiang, C. Jiang, Y. Zhang, Y. Cao, Electrophosphorescent chelating copolymers based on linkage isomers of naphthylpyridine-iridium complexes with fluorene, Macromolecules, 39 (2006) 1693-1700.
[15] P.L. Burn, S.C. Lo, I.D. Samuel, The Development of Light-Emitting Dendrimers for Displays, Advanced Materials, 19 (2007) 1675-1688.
[16] S.-C. Lo, E.B. Namdas, C.P. Shipley, J.P. Markham, T.D. Anthopolous, P.L. Burn, I.D. Samuel, The synthesis and properties of iridium cored dendrimers with carbazole dendrons, Organic electronics, 7 (2006) 85-98.
[17] S.-C. Lo, P.L. Burn, Development of dendrimers: macromolecules for use in organic light-emitting diodes and solar cells, Chemical reviews, 107 (2007) 1097-1116.
[18] S.-C. Lo, R.E. Harding, E. Brightman, P.L. Burn, I.D. Samuel, The development of phenylethylene dendrons for blue phosphorescent emitters, Journal of Materials Chemistry, 19 (2009) 3213-3227.

[19] T. Hebner, C. Wu, D. Marcy, M. Lu, J. Sturm, Ink-jet printing of doped polymers for organic light emitting devices, Applied Physics Letters, 72 (1998) 519-521.

[20] J. Ding, J. Gao, Y. Cheng, Z. Xie, L. Wang, D. Ma, X. Jing, F. Wang, Highly Efficient Green-Emitting Phosphorescent Iridium Dendrimers Based on Carbazole Dendrons, Advanced Functional Materials, 16 (2006) 575-581.

[21] S. Hecht, J.M. Fréchet, Dendritic encapsulation of function: applying nature's site isolation principle from biomimetics to materials science, Angewandte Chemie International Edition, 40 (2001) 74-91.

[22] T. Tsuzuki, N. Shirasawa, T. Suzuki, S. Tokito, Organic light-emitting diodes using multifunctional phosphorescent dendrimers with iridium-complex core and charge-transporting dendrons, Japanese journal of applied physics, 44 (2005) 4151.

[23] M. Velusamy, K.J. Thomas, C.-H. Chen, J.T. Lin, Y.S. Wen, W.-T. Hsieh, C.-H. Lai, P.-T. Chou, Synthesis, structure and electroluminescent properties of cyclometalated iridium complexes possessing sterically hindered ligands, Dalton Transactions, (2007) 3025-3034.

[24] J. Markham, S.-C. Lo, S. Magennis, P. Burn, I. Samuel, High-efficiency green phosphorescence from spin-coated single-layer dendrimer light-emitting diodes, Applied physics letters, 80 (2002) 2645-2647.

[25] Y. Tao, C. Yang, J. Qin, Organic host materials for phosphorescent organic light-emitting diodes, Chemical Society Reviews, 40 (2011) 2943-2970.

[26] H. Fukagawa, K. Watanabe, S. Tokito, Efficient white organic light emitting diodes with solution processed and vacuum deposited emitting layers, Organic Electronics, 10 (2009) 798-802.

[27] E.B. Namdas, A. Ruseckas, I.D. Samuel, S.-C. Lo, P.L. Burn, Photophysics of fac-tris (2-phenylpyridine) iridium (III) cored electroluminescent dendrimers in solution and films, The Journal of Physical Chemistry B, 108 (2004) 1570-1577.

[28] A. Boudrioua, P. Hobson, B. Matterson, I. Samuel, W. Barnes, Birefringence and dispersion of the light emitting polymer MEH–PPV, Synthetic metals, 111 (2000) 545-547.

Chapter 4

Effects of Polymerisation and Dendronisation on iridium (III) OLEDs

4.1 Introduction

In organic light emitting diodes, a key property requirement of the material is a high photoluminescence quantum yield. It is now widely recognized that OLED materials also need to have sufficient charge mobility to avoid high driving voltages. In Chapter 3, a first generation Iridium dendrimer (with electrically insulating biphenyl dendrons) was described as a candidate for solution processed OLEDs. One option to improve the charge transport and potentially therefore the efficiency of OLED devices would be to incorporate a charge-transporting moiety within the device or dendrimer structure. Carbazole-based compounds are well-known as high mobility hole-transporting materials and accordingly, they have been used widely in phosphorescent metal complexes OLEDs as host materials [1, 2] and within host free dendrimers in which the carbazole unit makes up the dendron [3, 4]. The inclusion of the carbazole dendrons within Iridium III (Ir) complexes by covalent bonding, results in the formation of a single multifunctional dendrimer in which the carbazole serves indirectly as the host material while the Ir (III) core acts as an emissive dopant. The main benefit of this approach over doped devices is that phase separation is avoided, leading to higher device performance [5].

It has been found that first generation dendrons are insufficient to prevent interactions between the emissive core[6]. Although higher generation dendrons will sufficiently reduce the internal interactions to maintain a high PLQY, they usually cause a significant reduction in charge transport[7, 8]. A compromise therefore exists that the intermolecular interactions that affect the quenching in luminescent materials can be controlled by the number of dendrons [4, 9-11]. Dendrons can be used as branched shells surrounding the Ir complex to prevent self-aggregation and concentration quenching of the emissive core in the solid state. Singly-dendronised dendrimers have an opened face of the core chromophore which lends them susceptible to intermolecular interaction. This issue can be resolved by creating so-called “doubly-dendronised dendrimers” which have two dendrons attached to each ligand of the core[12, 13].

Phosphorescent dendrimer materials with suitable dendrons can be used to make highly efficient solution processed OLEDs[4]. Nevertheless, the viscosity of these dendrimer solutions under standard processing concentrations is only slightly greater than the solvent they are dissolved in, and this viscosity is too low for solution processed mass production methods such as inkjet printing [14-16]. This is the motivation for exploring a new approach to the phosphorescent materials in the form of iridium (III) poly(dendrimers). It is anticipated that these materials would simultaneously improve the solution processibility whilst giving the material the better film forming needed for roll to roll or inkjet printing [13, 17, 18].

This Chapter first describes the pre-fabrication characterisation of a hostless dendrimer with a single carbazole Dendron, followed by its performance in a device. Next, the study focused on how polymerisation of this compound in order to achieve the desire film quality for printing techniques enhances the device performance and photophysical properties. Finally, the effect of introducing an additional carbazole dendron to the system will be described via a similar methodology on both doubly-dendronised dendrimer and the poly(dendrimer) analogues.

4.2 Singly-dendronised dendrimer and poly(dendrimer)

4.2.1 Material design and experimental methods

The chemical structure of singly-dendronised dendrimer (D1) and poly(dendrimer) (P1) are shown in Figure 4.1.a and b; both molecules consist of an Ir (III) core encapsulated within a set of carbazole dendrons. The poly(dendrimers) P1 was synthesized using Ring Opening Metathesis Polymerisation (ROMP) as it has been found to be an effective route for joining together bulky dendrimeric monomers with high M_ws[19, 20]. It has been shown that the use of conjugated polymers such as poly(fluorene) for phosphorescent emitters is problematic since they have low triplet energy. This leads to a reduction in the PLQY due to back transfer of triplet excitation from the phosphorescent emitter to the polymer [21, 22]. Therefore a norbornenyl-based non-conjugated polymer backbone was used with dendrimer side-chains to make the poly(dendrimers).

In addition, two small molecules commercially available from Lumtec, 4,4’-N,N’-dicarbazolyl-biphenyl (CBP) and 2,2',2''-(1,3,5-Benzinetriyl)-tris(1-phenyl-1-H-benzimidazole) (TPBi) were used as host and electron transport materials, respectively, shown in a previous Chapter (Figure 3.1.b and c).

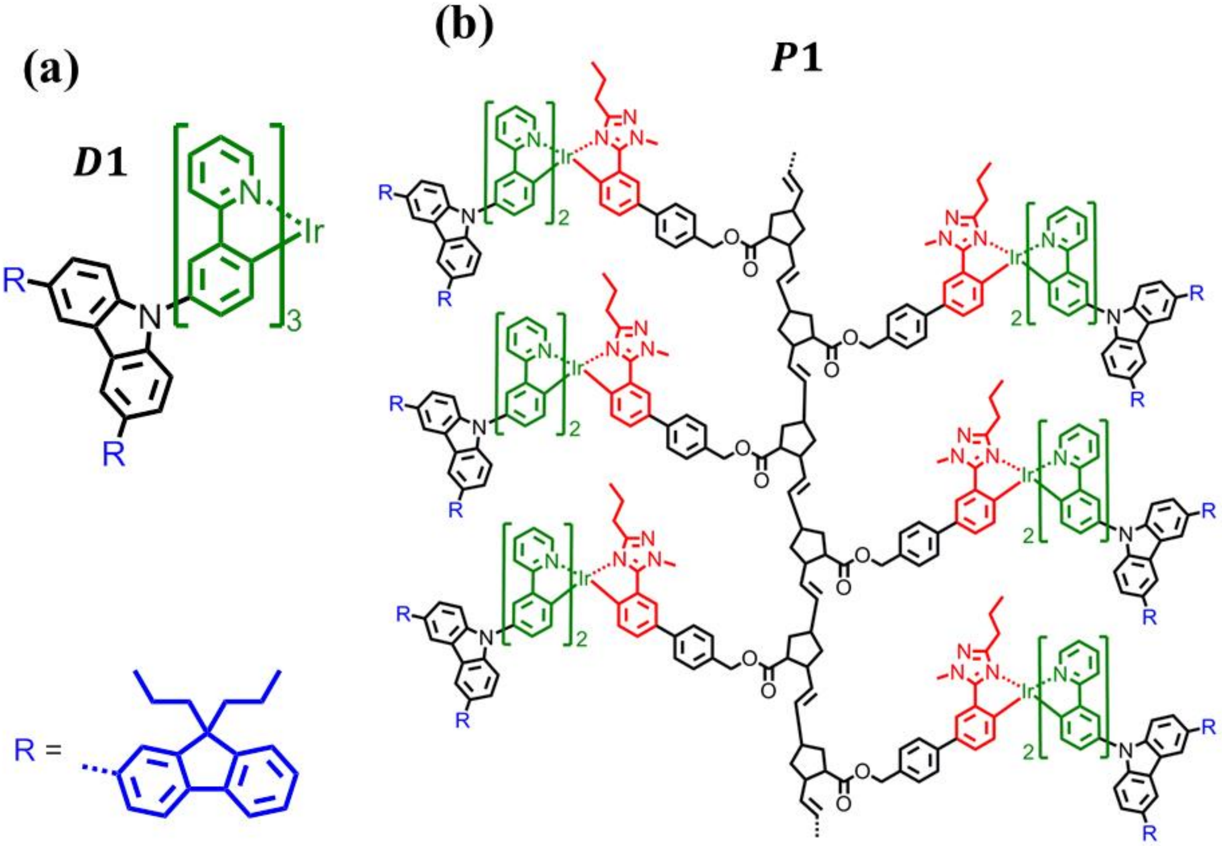

Figure 4.1 Chemical structures of, a) singly-dendronised dendrimers D1 and, b) singly-dendronised poly (denrimers) P1, with $\bar{M}_{w}$ of 160 kDa and a polydispersity (PDI) of 1.3.

The relevant device structure is shown in Figure 4.2.a and consists of pre-patterned indium-tin oxide (ITO) (170 nm)/ PEDOT: PSS (40 nm)/ emissive layer (≈50 nm-80 nm)/ TPBi (35 nm)/ LiF(1 nm)/ Al(100 nm). Substrates were pre-cleaned with isopropanol and water and then treated with UV-ozone for 15 minutes at 25°C immediately prior to use. PEDOT: PSS was spin coated on the pre-patterned ITO coated glass substrates (10 Ω/sq) and annealed for 15 min at 150° C. The PEDOT: PSS layer was used to improve hole-injection into the device by bending the energy levels of emissive layer to ITO. Devices were then transferred into a glovebox where the emissive layer (neat or blend) was deposited on the substrates by spin-coating inside the box. Spin-coatings were performed using solutions in chlorobenzene or chloroform at a concentration of 20 mg/ml where the blend solution consisted of 20 wt% dopant. The spin speed and concentration were chosen to be the same for D1 and P1 devices in order to monitor viscosity and subsequently thickness differences. The thickness of the emissive layers was measured with a Dektak where the thickness for the dendrimer layer was (≈50 nm) and for the poly(dendrimer) (≈80 nm). The results were consistent with reported studies where the viscosity of dendrimers is equal to the solvent and the viscosity of pol(dendrimer) slightly changes with concentration [18]. The final layers for the devices were deposited via thermal evaporation using a shadow mask to deposit successive layers of TPBi, LiF, and Al in a vacuum chamber with a base pressure of around 5×10^{-6} mbar. The TPBi deposition rate was maintained at approximately 1 Å/s. After the organic layer was deposited, the cathode layers, LiF (1 nm) and Al (100 nm), were deposited using a second shadow mask without breaking the vacuum. Cathode layers were chosen according to their energy levels (see Figure 4.2 b). Completed devices were transferred under inert atmosphere from the vacuum chamber to a glovebox (water and oxygen concentration levels < 0.1 ppm) for encapsulation with a glass cover using UV cured epoxy resin and an adhesive desiccant. Encapsulated devices were then transferred outside glovebox for characterisation as explained in Chapter 2.

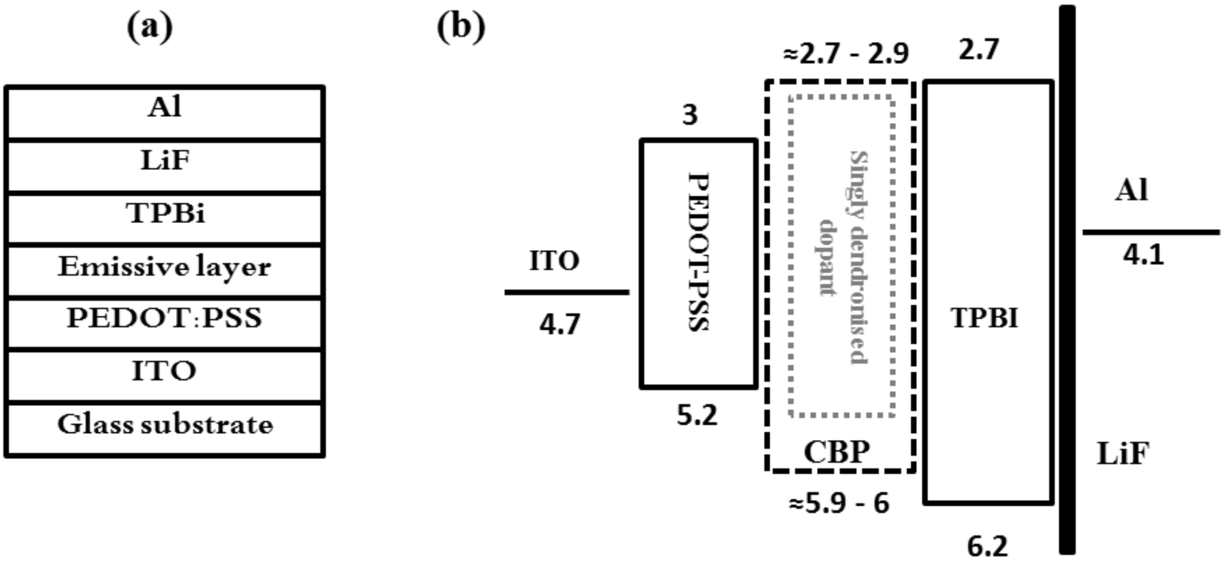

Figure 4.2 a) Device structure, b) energy level diagram for different layers.

4.2.2 Photo-physical properties

In order to use these compounds in OLED structures, photo-physical characterisation was performed and the results are presented in this Section. From the previous Chapter, the HOMO energy level of G1 Ir(ppy)$_3$ with biphenyl ligands was found to be 5.2 eV. However, from PESA measurements, the HOMO energy level of the singly-dendronised materials (D1 and P1) was found to be 5.4 eV. This suggests that the HOMO density for these compounds was not just on the Iridium core, but was also located on the dendrimeric carbazole units.

The absorption spectra of this family of compounds in solution, neat films and, CBP blend films are shown in Figure 4.3. The Absorption spectra for the dendrimer D1 and the poly(dendrimer) P1 both consist of two different regions: a short wavelength region from 280-350 nm due to singlet-singlet $\pi - \pi^*$ absorption by the carbazole dendron and phenylpyridyl ligand, and a weak absorption shoulder at longer wavelengths assigned to metal to ligand charge transfer. The strong absorption feature at 320 nm is a characteristic of carbazole unit which is consistent with $\pi - \pi^*$ absorption, as previously reported in other carbazole containing materials[4]. This to a slightly lower HOMO-LUMO energy gap of the carbazole unit compared with phenyl rings[4].

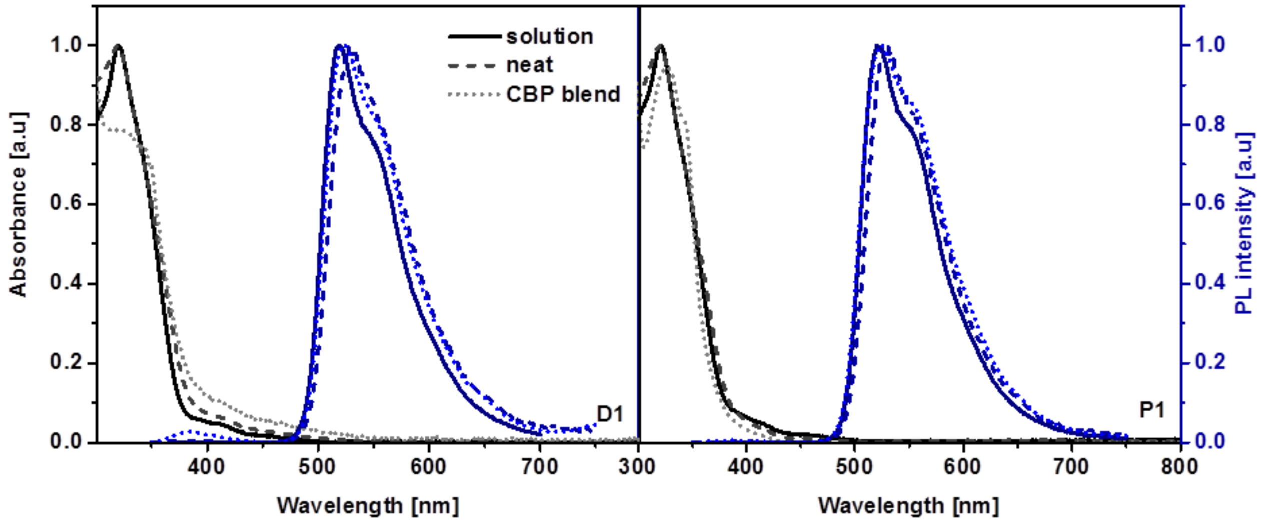

Figure 4.3 Normalized absorption (black) and PL (blue) spectra of singly-dendronised dendrimers D1 and poly (dendrimers) P1 for solution (solid line), neat film (dash line), and CBP blend film (dotted line).

The photoluminescence spectra of the compounds were studied in order to investigate the effect of polymerisation on the emission properties of these compounds. Figure 4.3 shows the normalized PL spectra for D1 and P1 in solution, neat film and, in CBP. Looking at each material separately, the shape of the PL spectra in solution, neat and, CBP blend are almost identical; however, the emission peak is slightly red-shifted (≈2-10 nm) and the shoulder is less pronounced moving from solution to the solid state. This was anticipated and can be attributed to a decrease of freedom in the solid-state.

The PL spectra in solution for the singly-dendronised compounds have a maximum emission peak at 520 nm and a shoulder at 548 nm. A very weak emission peak in the blends was noted at 385 nm, which is due to the host material (CBP). Comparing the results of absorption and PL emission spectra for D1 and P1, there are no significant differences to be noted. This suggests that the polymerisation of the compound doesn’t have any effect on the intrinsic emission of the chromophore core.

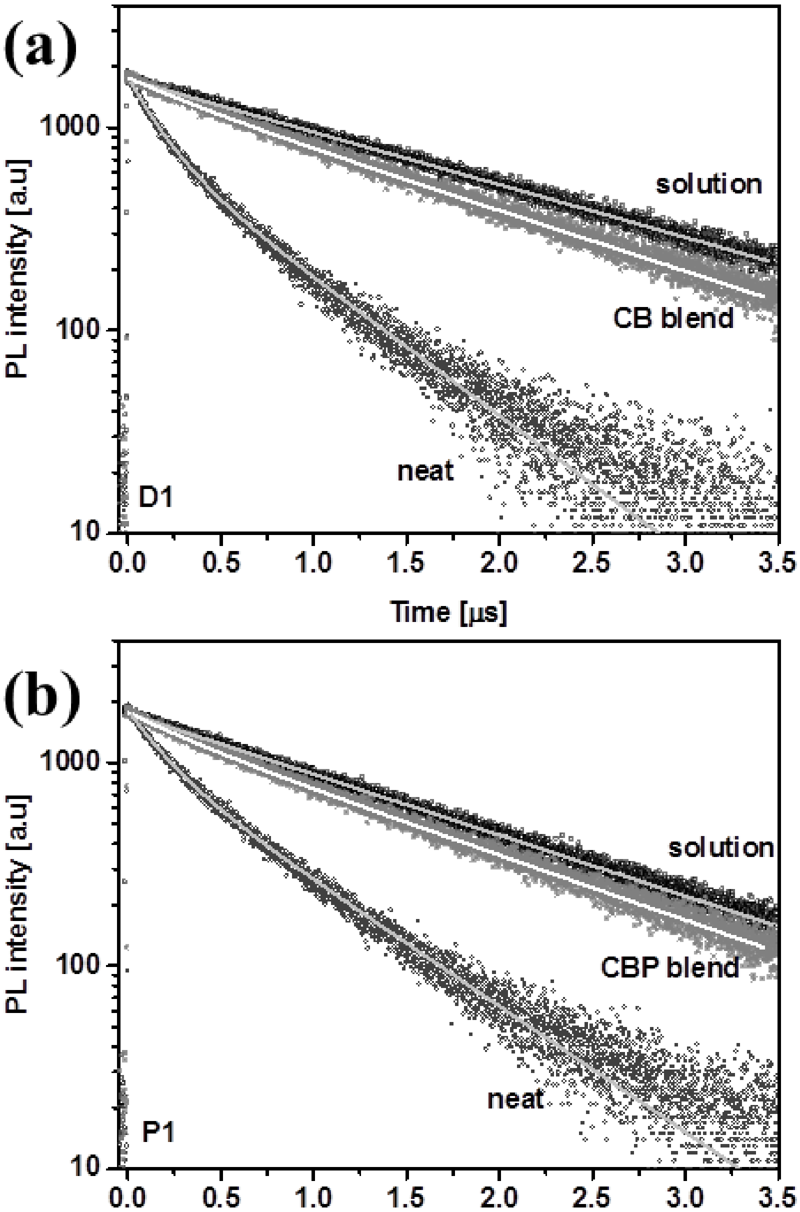

Figure 4.4 Lifetime measurements (TCSPC) for: a) singly-dendronised dendrimer (D1) and b) poly(dendrimers) (P1) in degassed solution, neat film, and CBP blend film. Comparing the solid state neat film of both compounds, it can be noted that the bi-exponential PL decay moving toward the mono-exponential decay. The samples were excited by a 372 nm LED and the emission was detected at the peak of PL spectra (520nm- 525nm)

The PLQY and the PL decay measurements were performed in order to investigate the effect of polymerisation on the luminescence concentration. Measurements were initially performed on degassed solutions of all compounds, as explained in Chapter 2. The solution PLQY values of these compounds are shown in table 4.1. The values for these compounds is higher than the PLQY values of their biphenyl counterparts, which have been reported to be ~ 65% [17]. Given that the uncertainty of the measurements is about 10%, the solution PLQY values are in good agreement for D1 and P1 which is expected as they share the same emissive core, and the individual cores are well separated in optically dilute solutions. The PL decay measurements (see Figure 4.4) for D1 and P1 in solution shows a mono-exponential decay with lifetimes of the emissive species (see Table 4.1) for the singly-dendronised dendrimer (D1≈1.7μs) and the poly(dendrimer) (P1≈1.5μs). However, the radiative lifetimes for all these compounds, calculated from the PLQY and the PL decay values, are similar (all ≈ 2.1μs) indicating that the polymerisation doesn't affect the emission from the excited species.

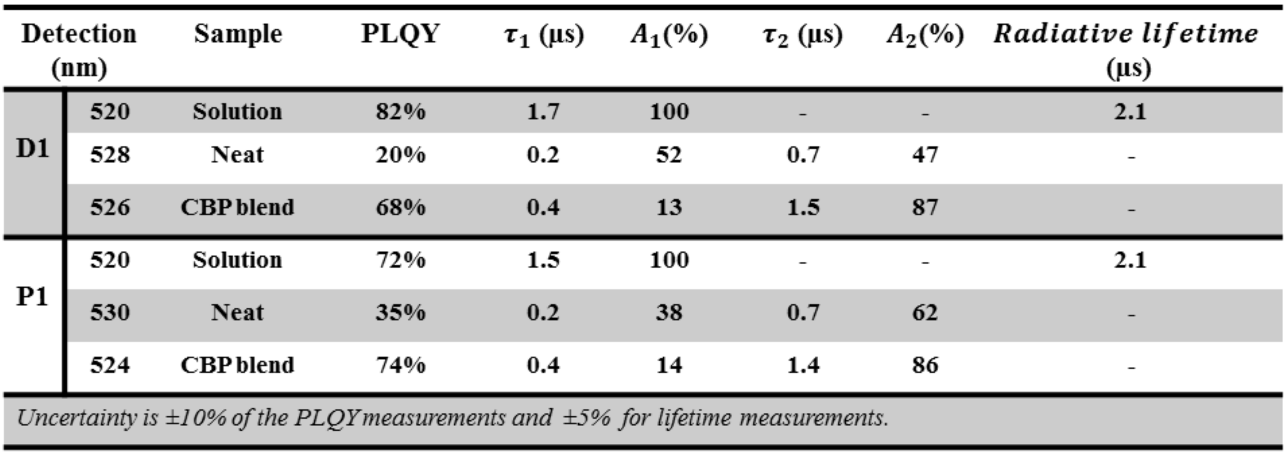

	Detection (nm)	Sample	PLQY	τ_1 (μs)	A_1(%)	τ_2 (μs)	A_2(%)	*Radiative lifetime* (μs)
D1	520	Solution	82%	1.7	100	-	-	2.1
	528	Neat	20%	0.2	52	0.7	47	-
	526	CBP blend	68%	0.4	13	1.5	87	-
P1	520	Solution	72%	1.5	100	-	-	2.1
	530	Neat	35%	0.2	38	0.7	62	-
	524	CBP blend	74%	0.4	14	1.4	86	-

Uncertainty is ±10% of the PLQY measurements and ±5% for lifetime measurements.

Table 4.1 A summary of PLQY and PL decay values for singly-dendronised compounds in degassed solution, solid state neat and, blend.

The PLQY values for neat films show an abrupt decrease compared to the solution values, for example from 82% to 20% for D1, which indicates that strong inter-chromophore interactions lead to concentration quenching in the solid state. A summary of PLQY values and PL decay measurements are presented in Table 4.1.

The PL decay lifetime measurements for neat films are bi-exponential decays. This indicates that there are multiple emissive species present in the neat films. However, the effect of polymerisation can be clearly seen by changes in the amplitudes and lifetimes of these species (seen in Table 4.1). Polymerisation of the dendritic structures seems to increase not only the slower component lifetime and amplitude factor, but also the PLQY values.

In order to further decrease the concentration quenching between cores, these compounds were blended with CBP. The photo-physical properties for these compounds were investigated in 20% wt CBP blends and are shown in Table 4.1. The solid state PLQY of these blends increases, showing a similar trend to that observed with the solution PLQY measurements. Moreover, the lifetime decays show a bigger ratio of the slower components with a more similar lifetime to the solution. Both of these values are consistent with each other, showing that there are still inter-chromophore interactions that are not completely controlled in CBP blends. The lifetime of the CBP emissive peak at 385 nm which was observed in the blends (see Figure 4.3) - was reported to be on the order of ns [23], which was faster than the time resolution of our instrument.

4.2.3 Device performance

To assess whether the high photoluminescence efficiency found in the solid state for these compounds could lead to efficient OLEDs, a number of devices were fabricated. This Section presents the results of these devices.

The typical electrical characteristics of D1 and P1 is shown in Figure 4.5 for neat and CBP blend devices. TPBi was used in all the devices as it was shown in Chapter 3 that TPBI not only facilitates the electron injection, but increases the recombination rate by blocking holes, which both of these processes lead to higher EQE values. Neat devices were tested to lower voltages to avoid triplet-triplet annihilation and demonstrated quick roll off, as shown in neat devices of D1 (see Figure 4. 5. a). Although similar values of luminance and current density were obtained for both compounds, there are distinct differences in the performances of neat and blend-based devices. In neat devices, slightly higher turn on voltages were observed for poly(dendrimer) devices (4.6V) in comparison with the dendrimer (3.5 V), which is consistent with the slightly thicker active layer.

The neat devices showed sharper current and luminance increases with lower turn on voltage in comparison with their CBP blend counterparts for each material. It is clear that they pass higher current density through devices at the same voltage in comparison with the blended devices. There are multiple possible reasons for this including, for example, better interfaces in the neat devices or better charge injection into the neat devices. Polymerisation seems to slightly improve the performance and this could be due to providing higher viscosity, better film forming or better packing and morphology.

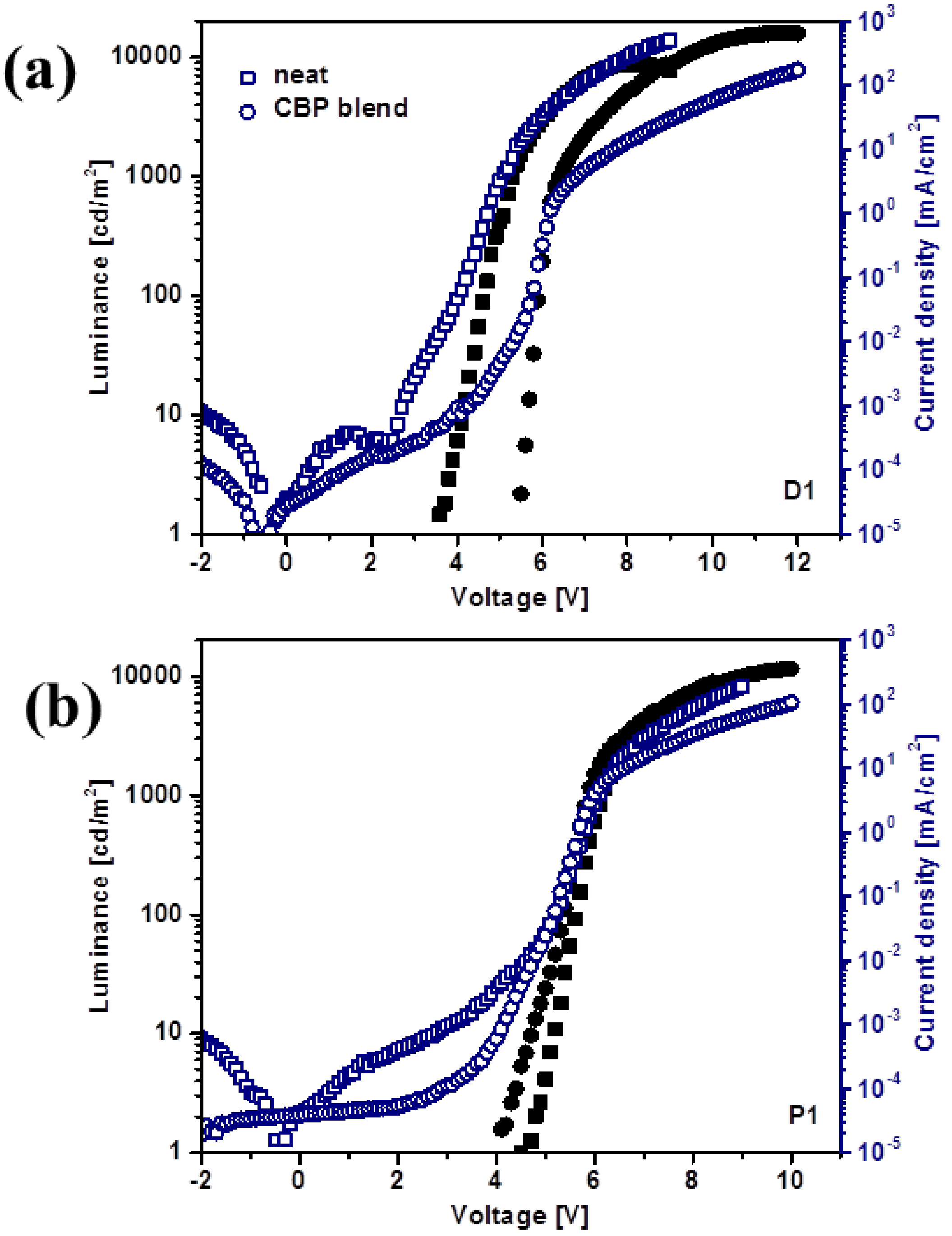

Figure 4. 5 Current density and luminance characteristics in neat (square) and CBP blend (circle) devices for singly-dendronised: a) dendrimer (D1), and b) poly (dendrimers) (P1).

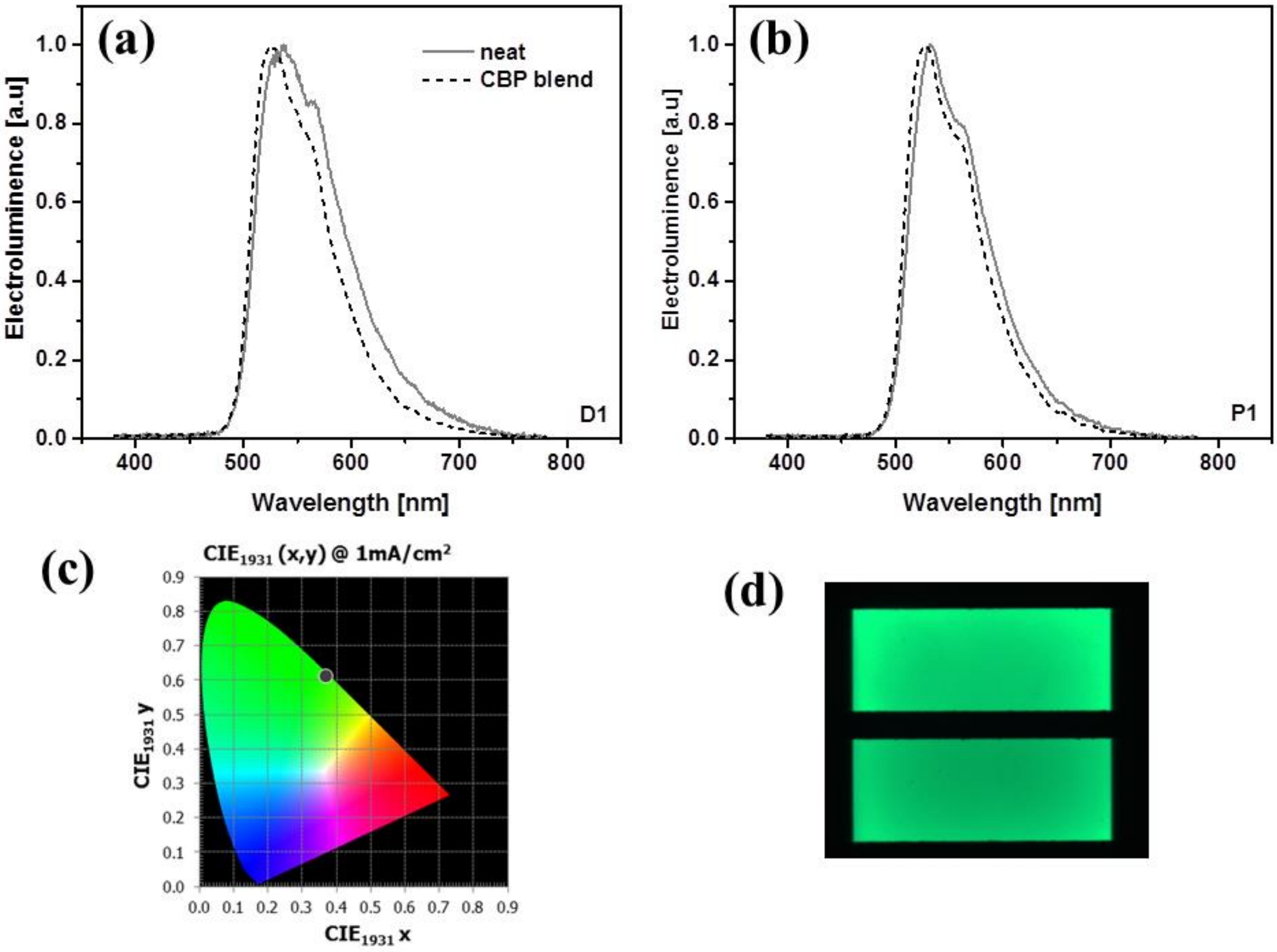

Figure 4.6 Electroluminescent spectrum for singly-dendronised compounds in neat (solid line) and CBP blend (dot line) devices: a) D1, b) P1; c) CIE co-ordinates, and d) close up of an actual performing device.

Figure 4.6. a and b show the electroluminescent spectrum for both compounds as neat and CBP blend devices. EL and PL spectra for each compound are in agreement with each other, sharing similar shape. This indicates that the electrical excitation process is similar to the photo excitation. Polymerisation seems to decrease the red shifts as observed in neat films compared with blended devices. This is in agreement with the PL spectrum results in Figure 4.3. For the singly-dendronised compounds, the maximum emission peak in blends is at 525 nm and the emission color was green with CIE co-ordinates of (0.37, 0.54) at 1mA/cm^2 (see Figure 4.6.c). A clear green color is observable (see Figure 4.6. d).

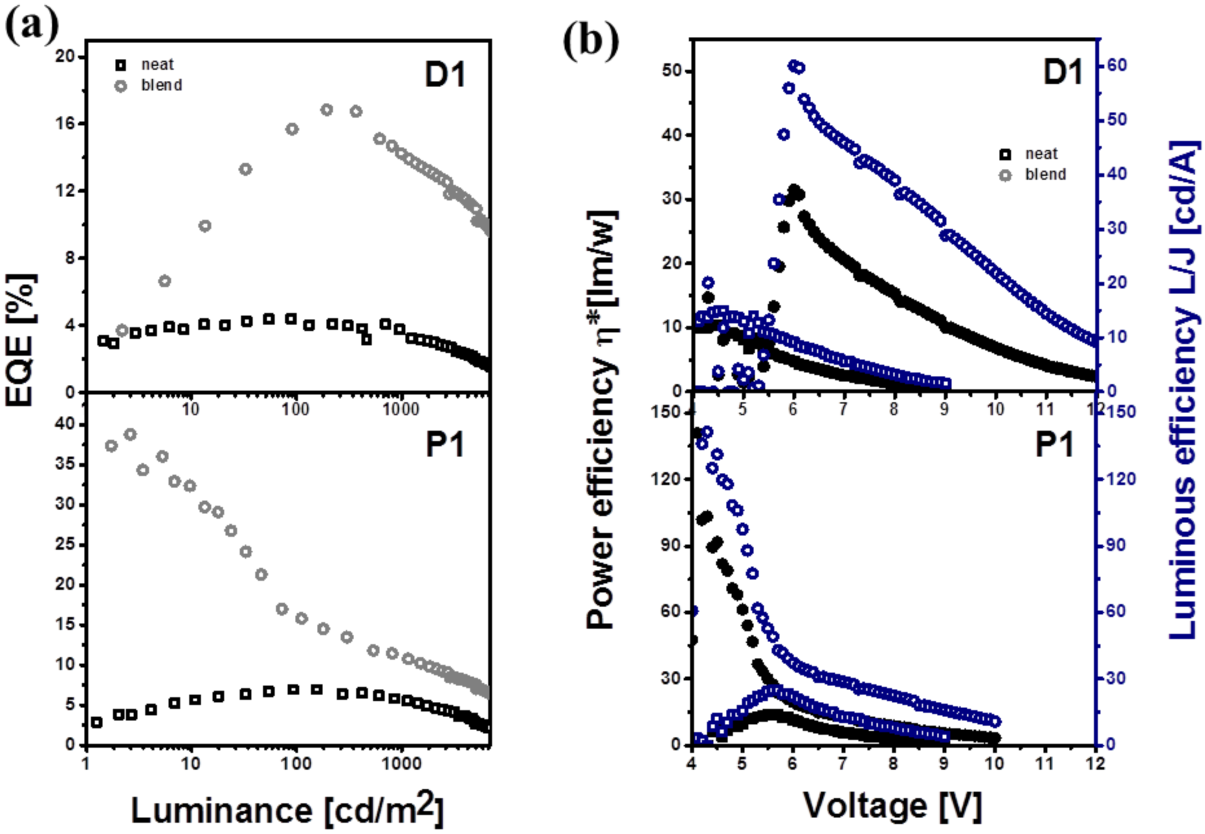

Figure 4.7 Efficiency of devices are presented for both compounds in different units: a) EQE and b) power efficiency (left axis) and luminous efficiency (right axis).

External quantum efficiencies were calculated for the devices in order to provide a better understanding of the V-I-L (voltage-current-luminance) characteristics, as this is proportional to the ratio of luminance to current. The EQE versus the luminance for the devices are shown in Figure 4.7.a. The data shows that devices with a neat emissive layer are less efficient. However, the EQE values (at 100 cd/m^2) increase for D1 (4.5%) compared with P1 (7%), confirming that polymerisation benefits device performance in this case. This can be due to better film forming as the poly(dendrimer) has better film packing. In contrast to neat devices, the one with a blended emissive layer demonstrates a sharp initial increase in EQE, and confirms the higher injection barrier in them. This could be due to the bigger energy gap between the energy levels of CBP and PEDOT: PSS. Moreover, the efficiency can be represented in other units for example power efficiency and luminous efficiency (see Figure 4.7.b) for both compounds in neat and blend devices. The effect of polymerisation can be seen in the increased power efficiency value (33.5 lm/W) for P1 compared with D1 (29.7 lm/W). A summary of device performance is presented in Table 4.2.

4.2.4 Dipole orientation

According to theoretical studies of out-coupling of an OLED explained in Chapter 1, the amount of light which can escape the OLED devices without any manual enhancement is approximately 20% of the total PLQY of the emissive layer[24]. This is because of several loss channels in the OLED structure, which include: glass absorption; edge emission; wave guided or plasmon modes; etc. Therefore, the EQE value of an OLED is expected to reach a maximum of 20% of the obtained PLQY values. However, some of the devices made from singly-dendronised materials demonstrated EQE values higher than the theoretical limitation, which indicates an out-coupling of more than 20%. Indeed, the poly(dendrimer) material in blend devices performed with an excellent maximum EQE of 30% at a the eye-detectable brightness (17 cd/m^2) which has not been observed in solution processed OLEDs before. This result suggests the possibility of horizontally oriented dipoles in the emissive layer, which is further described in this Section.

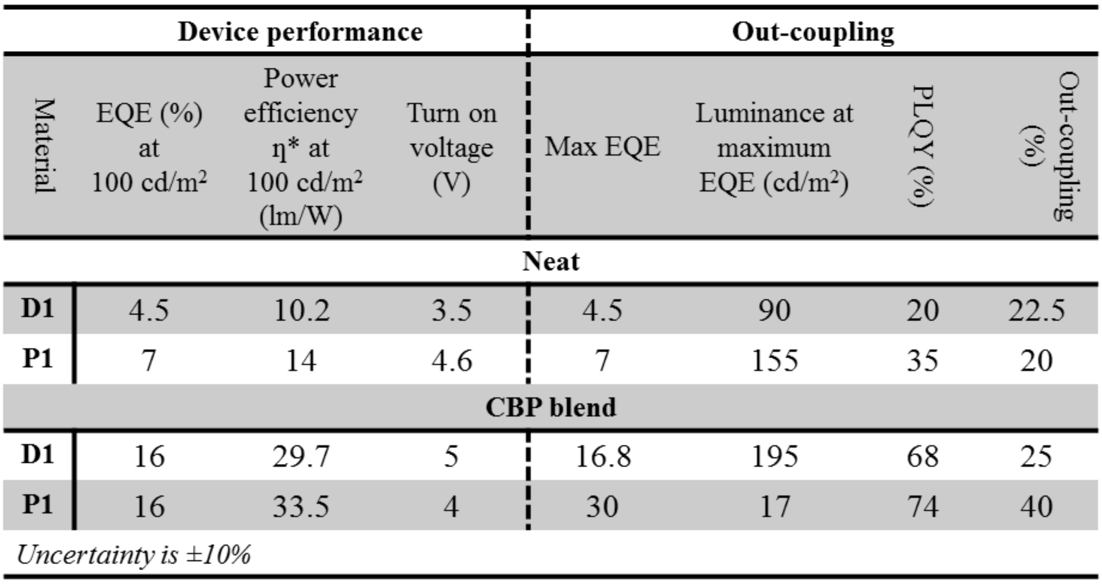

Device performance				Out-coupling			
Material	EQE (%) at 100 cd/m^2	Power efficiency η* at 100 cd/m^2 (lm/W)	Turn on voltage (V)	Max EQE	Luminance at maximum EQE (cd/m^2)	PLQY (%)	Out-coupling (%)
Neat							
D1	4.5	10.2	3.5	4.5	90	20	22.5
P1	7	14	4.6	7	155	35	20
CBP blend							
D1	16	29.7	5	16.8	195	68	25
P1	16	33.5	4	30	17	74	40

Uncertainty is ±10%

Table 4.2 A summary of electrical characterization and out-coupling calculations for carbazole dendrimers and poly (dendrimers) in neat and blended devices.

The out-coupling parameter (ϕ_{escape}) was calculated for all devices (see Table 4.2) at the maximum EQE where electrons and holes are equally balanced and providing near 100% recombination rate. The singly dendronised dendrimer (D1) exceeded the theoretical limit of out-coupling (20%), displaying outcoupling of 22.5% and 25% in neat and blend devices respectively and moreover outstanding outcoupling for the poly(dendrimer) P1 of 40%. Variable angle spectroscopic ellipsometry and angle dependent PL measurements were performed for these materials as explained in Chapter 2 to investigate the possible preferred orientation of the emissive dipoles.

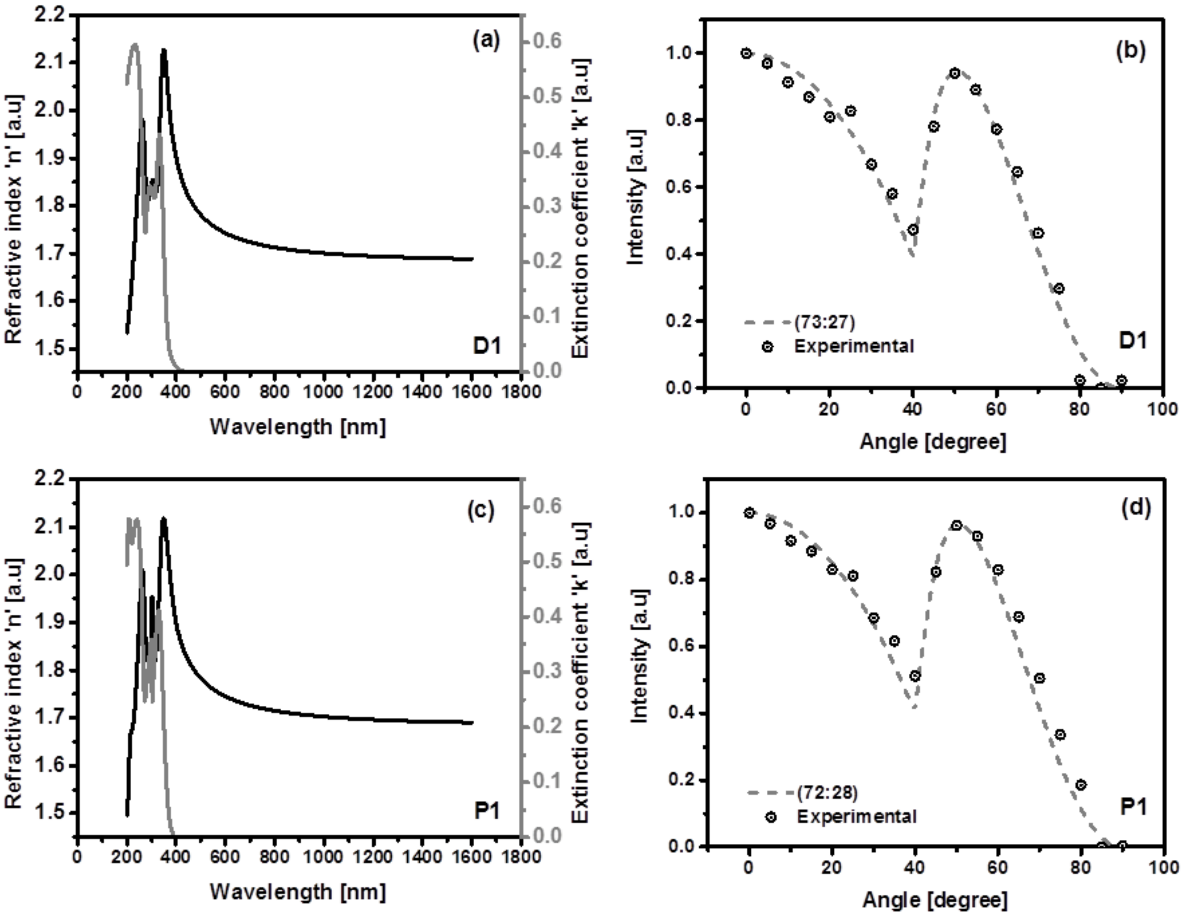

Figure 4.8 Variable angle spectroscopic ellipsometry (a and c) and angle dependent PLresults (b and d) for singly-dendronised compounds D1 and P1 respectively.

The measurements were performed on blended materials as they provided higher phosphorescent efficiencies, which lead to more reliable investigation[25]. The refractive index and extinction coefficient results for CBP blended films from ellipsometry measurements are shown in Figure 4.8 a and c respectively for D1 and P1. Following the UV-VASE experiments, the orientation order parameter, *S*, was calculated according to equation 2.8 with 0.03 and 0.0082, respectively, for D1 and P1. Although the S values are close to zero and indicate randomly orientation of the materials, further investigation on dipole orientation was performed via angle dependent PL spectrum measurements. It has been reported before that horizontally oriented dipoles can be achieved from spin casted films of isotropic materials[26]. The angle dependent PL spectrum measurements were performed on encapsulated films spin coated from the same solvent and conditions as applied during fabrication.

The experimental results from angle dependent PL measurements were then matched with simulation results from Setfos using the optical constants from VASE measurements and thickness of the emissive layer. The results indicate the existence of 73% and 72% horizontally oriented dipole respectively for D1 and P1, which are slightly higher than the isotropic model, which has 67% horizontally oriented dipoles. Similar behaviour has been reported in other solution processed organic light emitting materials[26]. Recent dipole orientation studies have shown that Iridium dendrimers with one different ligand attached to the core (i.e., heteroleptic complexes), similar to P1, are more likely to contain horizontally oriented emissive dipoles [27, 28]. This is a promising result for the OLED industry toward increasing the outcoupling of OLED devices via the intrinsic emission properties of the material.

4.3 Doubly-dendronised dendrimer and poly(dendrimer)

4.3.1 Material design and experimental methods

The interactions between the chromophore cores cannot be fully controlled with the first generation of the singly-dendronised compounds Ir (III) dendrimers. The photo-physical studies on their blended counterparts also indicated this fact by the existence of two emissive species. Moreover, previous studies have shown that higher generation dendrimers would bring the drawback of poorer transport characteristics [7, 8]. Nevertheless, a compromise between the improved PLQY and reduced charge transport (and vice versa) can be reached through increasing the number of dendrons attached to the Ir (III) core [4, 9-11]. The self-aggregation and concentration quenching of emissive core in the solid state can be prevented using dendrons as branched shells surrounding the chromophore cores. This approach can also resolved the opened face of the core chromophore in singly-dendronised compounds which are sentient to intermolecular interaction. A doubly-dendronised dendrimer (D2) was synthesised by introducing the second carbazole dendron to the other ligand of the core (see Figure 4.9.a). The poly(dendrimer) (P2) analogous to D2 was synthesised by ROMP in order to provide higher material viscosities which is advantageous to industrial mass production methods (e.g., inkjet printing). The chemical structures of both these compounds are shown in Figure 4.9 a and b.

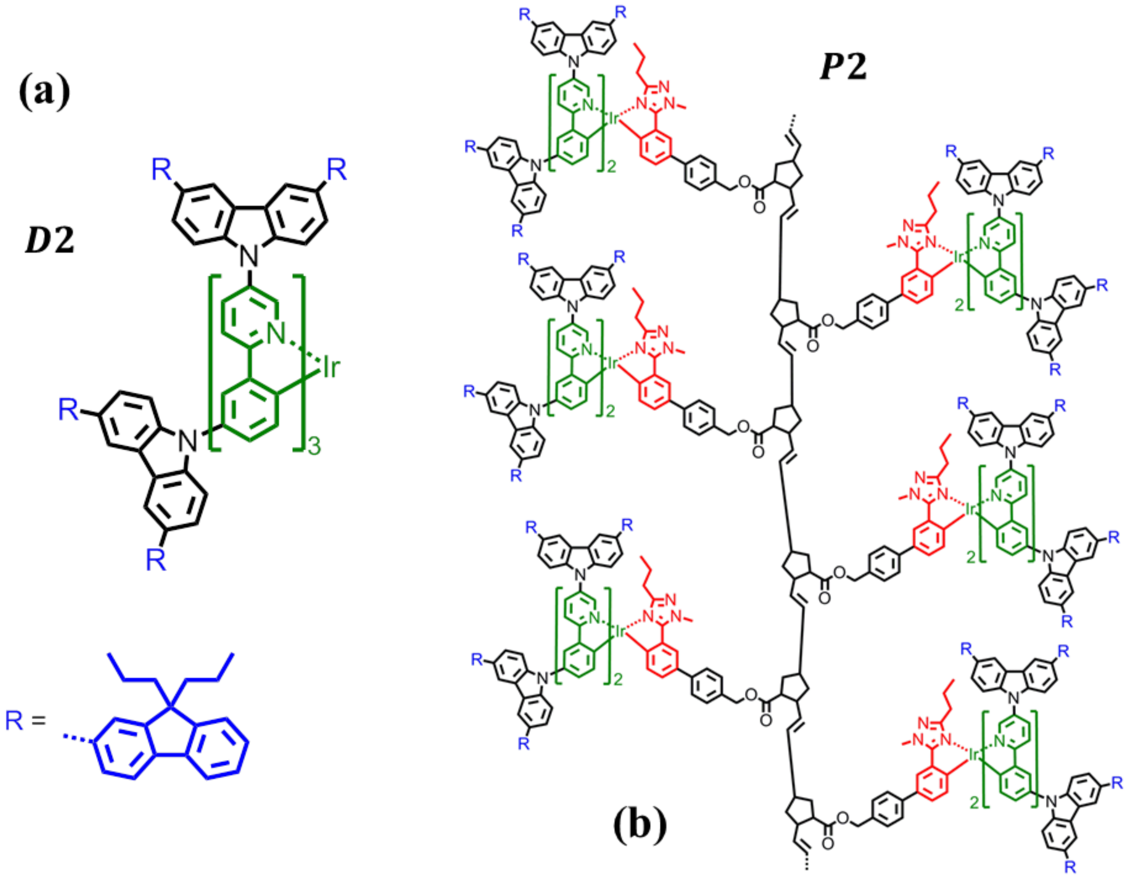

Figure 4.9 Chemical structures of, a) doubly-dendronised dendrimer, D2, b) doubly-dendronised poly(dendrimer), P2 with a $\bar{M}_\mathrm{w}$ of 68 kDa and a PDI of 2.4.

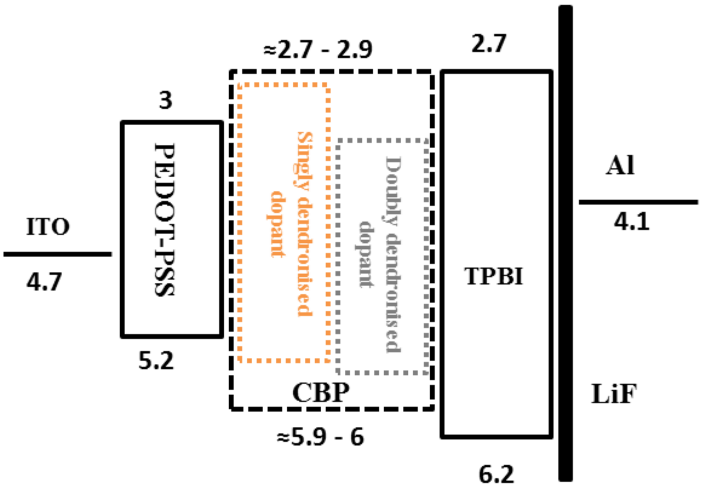

Figure 4.10 Energy level diagram for doubly-dendronised compounds.

The identical device structure and fabrication process was used for these compounds in order to have a consistent comparison (see Figure 4.10).

4.3.2 Photo-physical properties

The photo-physical characteristics were measured in order to investigate the dendronisation effects intrinsically and in OLEDs structure. The HOMO energy level of the doubly-dendronised compounds (D2 and P2) was calculated from the IP obtained by PESA measurements. The result shows that adding the second carbazole dendron increase the HOMO density to 5.6 eV, which is slightly higher than for singly-dendronised compounds (see Figure 4.10).

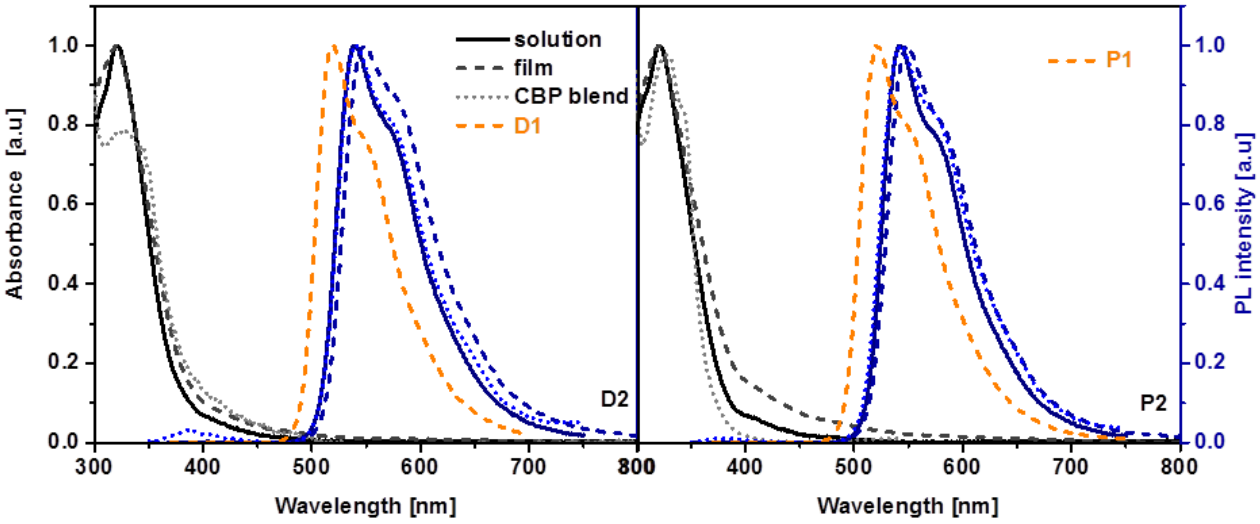

Figure 4.11 Normalized absorption (black) and PL (blue) spectra for doubly-dendronised dendrimer, D2, and poly(dendrimer), P2, for solution (solid line), neat film (dash line), CBP blend film (dotted line), PL absorption of singly-dendronised compounds are also plotted in orange dash line for comparison.

Figure 4.11 shows the absorption spectrum of the doubly-dendronised compounds. The absorption consists of two main regions for short and long wavelengths: the shorter wavelength absorption is due to singlet-singlet $\pi - \pi^*$ absorption by the carbazole dendrons and phenylpyridyl ligands and the longer wavelength absorption assigned to MLCTs. Although not shown, in non-normalized spectra the strong absorption peak of carbazole at 320 nm was found to increase with dendronisation, due to the increased in the number of carbazole units[4].

There is a red shift in the onset of **D2** and **P2** absorption compared with **D1** and **P1** which suggests a slightly narrower optical gap for doubly-dendronised compounds in comparison with singly-dendronised. This was then confirmed by HOMO-LUMO results inferred from PESA measurements of IP where the optical gaps for the singly- and doubly- dendronised compounds were found to be ≈ 2.6 eV and ≈ 2.2 eV, respectively. As previously reported, this is attributed to the attachment of the second dendron to the pyridine moiety of the phenylpyridine ligand, which extends the conjugation of the ligand[4, 17].

The PL spectra in solution for singly- dendronised compounds have a maximum emission peak at 520 nm and a shoulder at 548 nm. However, in the spectra of both of the doubly-dendronised compounds, the presence of the additional dendron resulted in a 20 nm red-shift in the emission spectra (compared with their singly-dendronised counterparts), with a peak maximum at 540 nm. The motivation for adding the additional dendron was to improve the core encapsulation in order to decrease intermolecular interactions. Nonetheless the drawback of this technique is an increase of conjugation length of the ligand involved in the MLCT, resulting in a red-shift in the emission colour [6, 29, 30]. The CBP emission peak in the blends can be seen for doubly-dendronised blends as reported for previous compounds. Moreover, polymerisation in doubly-dendronised compounds doesn’t have any effect on the intrinsic emission as the chromophore cores are the same. The PL spectrum in solution was identical for D2 and P2. This was also seen in the singly-dendronised compounds in the previous Section.

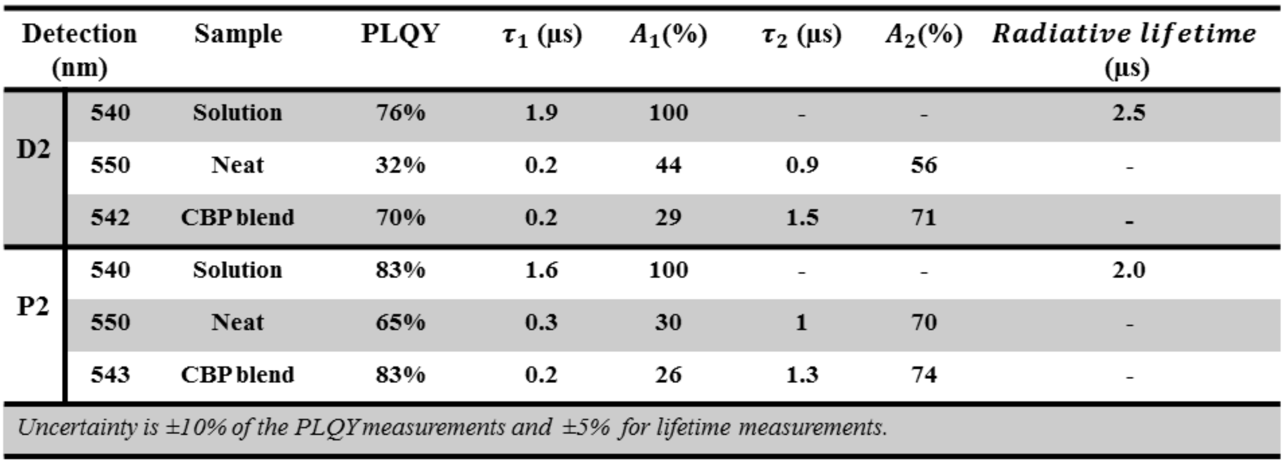

Detection (nm)		Sample	PLQY	τ_1 (μs)	A_1(%)	τ_2 (μs)	A_2(%)	*Radiative lifetime* (μs)
D2	**540**	**Solution**	**76%**	**1.9**	**100**	-	-	**2.5**
	550	**Neat**	**32%**	**0.2**	**44**	**0.9**	**56**	-
	542	**CBP blend**	**70%**	**0.2**	**29**	**1.5**	**71**	-
P2	**540**	**Solution**	**83%**	**1.6**	**100**	-	-	**2.0**
	550	**Neat**	**65%**	**0.3**	**30**	**1**	**70**	-
	543	**CBP blend**	**83%**	**0.2**	**26**	**1.3**	**74**	-

Uncertainty is ±10% of the PLQY measurements and ±5% for lifetime measurements.

Table 4.3 A summary of PLQY and PL decay values for doubly-dendronised compounds in degassed solution and solid states.

In order to better investigate the effect of dendronisation on concentration quenching on this pair of compounds, the PLQY and PL decay measurements were performed. The optically dilute degassed solutions were prepared as explained in Chapter 2. A summary of PLQY and PL decay values for doubly-dendronised compounds are presented in Table 4.3. The solution PLQY for the doubly-dendronised dendrimer D2 is higher than the PLQY value for its biphenyl counterpart, which is 71% [17]. The PLQY values for the singly- and doubly- dendronised compounds are similar and within the experimental error. Giving that they share the same emissive core, and that the cores are well separated in optically dilute solutions, the results are consistent with what we expect. The PLQY values decreased in solid states for both neat and blends. However, the effect of dendronisation is more observable in solid state where higher PLQY values are obtained for D2 compared with D1. The PL decay measurements were then used to confirm this result.

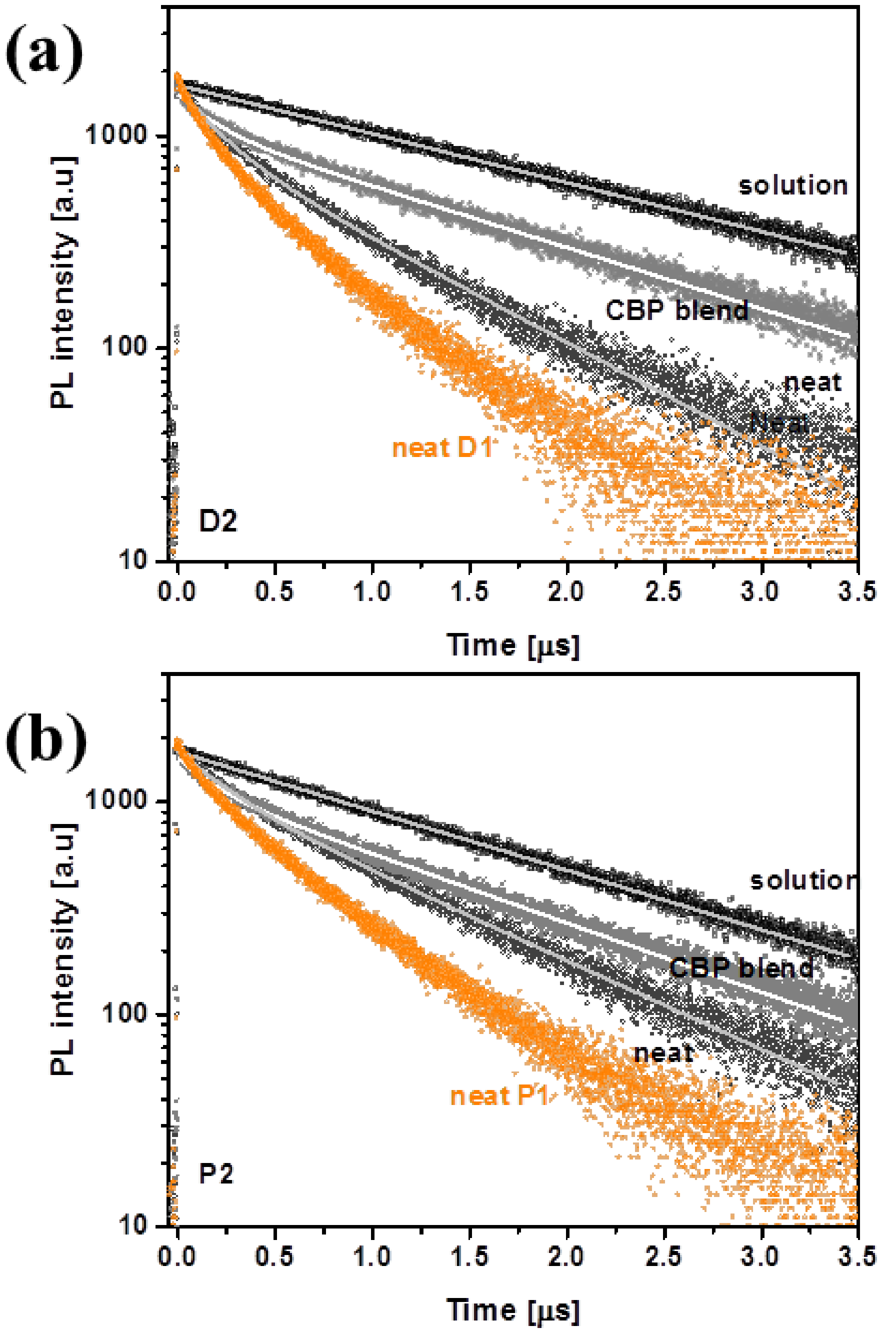

Figure 4.12 TCSPC measurements for a) doubly-dendronised dendrimer (D2) and b) doubly-dendronised poly(dendrimer) (P2) in degassed solution and solid states. The PL decay measurements of singly-dendronised compounds (D1 and P1) in neat film solid state are plotted as a reference in orange color. The samples were excited by a 372 nm LED and the emission was detected at the peak of PL spectra (540 nm- 545 nm)

The PL decay measurements are shown in Figure 4.12 for doubly-dendronised dendrimer (D2) and poly(dendrimer) (P2). The PL decay measurement for D2 and P2 in degassed solution shows also a mono-exponential decay but with a longer lifetime in comparison with their singly-dendronised counterparts: i.e., D2 ≈1.9µs whilst D1 ≈1.7µs and P2 ≈1.6µs whilst P1 ≈1.5µs). These results indicate that although the inter-chromophore interactions that lead to substantial photoluminescence quenching are not strong in solution, adding the second dendron is effective in reducing the inter-chromophore interactions in the solid state as the chromophore core will be slightly different from the singly dendronised. However the dendronisation and polymerisation don't affect the emission from excited species as the dendronisation didn't affect the radiative lifetime in the doubly-dendronised family of compounds.

The PL decay lifetime measurements in the solid state demonstrate the existence of two emissive species similar to what is observed for their singly-dendronised counterparts. Nevertheless, the presence of the additional dendron changes the lifetimes of the singly-dendronised dendrimer with a more significant contribution for the faster lifetimes (faster :0.2 µs, slower 0.7µs) in D1 to more than 50% contribution of slower emissive species with longer life time (faster : 0.2 µs, slower: 0.9 µs) in the doubly-dendronised dendrimer D2. Figures 4.12 a and b show the PL decay for the neat films transition from the bi-exponential toward the mono-exponential lifetime in moving from singly-dendronised dendrimer D1 to D2 and from P1 to P2. This indicates that inter-polymer interactions play a significant role in PL quenching in the neat films; therefore, encapsulation of the emissive core via double dendronisation leads to a slight increase in PLQY in the neat film by reducing the concentration quenching on the emissive cores.

4.3.3 Device performance

To assess the impact of the high PLQY values of the doubly-dendronised compounds in real devices, a number of devices were fabricated and the results presented in this Section. All devices were fabricated in an identical structure to those for the singly-dendronised compounds to enable an objective and fair comparison. TPBi was also used in these devices as the electron transport and hole blocking layer.

The electrical characteristics of the devices are shown in Figure 4.13. The neat devices (square points) were turned on at lower voltages (4V) and demonstrated a sharp increase in current density and luminance. They attained a higher current density and luminance, which indicates better interface and charge injection into the neat films. This behaviour is similar to what was observed for the singly-dendronised neat films presented in the previous Chapter. The photo-physical properties of the blended solutions showed an enhancement in luminance quenching by introducing extra space between the chromophore cores. Therefore a number of devices were fabricated from CBP blend solutions to evaluate their efficiency in OLEDs. The poly(dendrimer) blend also demonstrated a lower turn on voltage (4.9V) in comparison with the dendrimer (6V), which indicates better injection - this can be attributed to better film formation at the interface of the emissive layer.

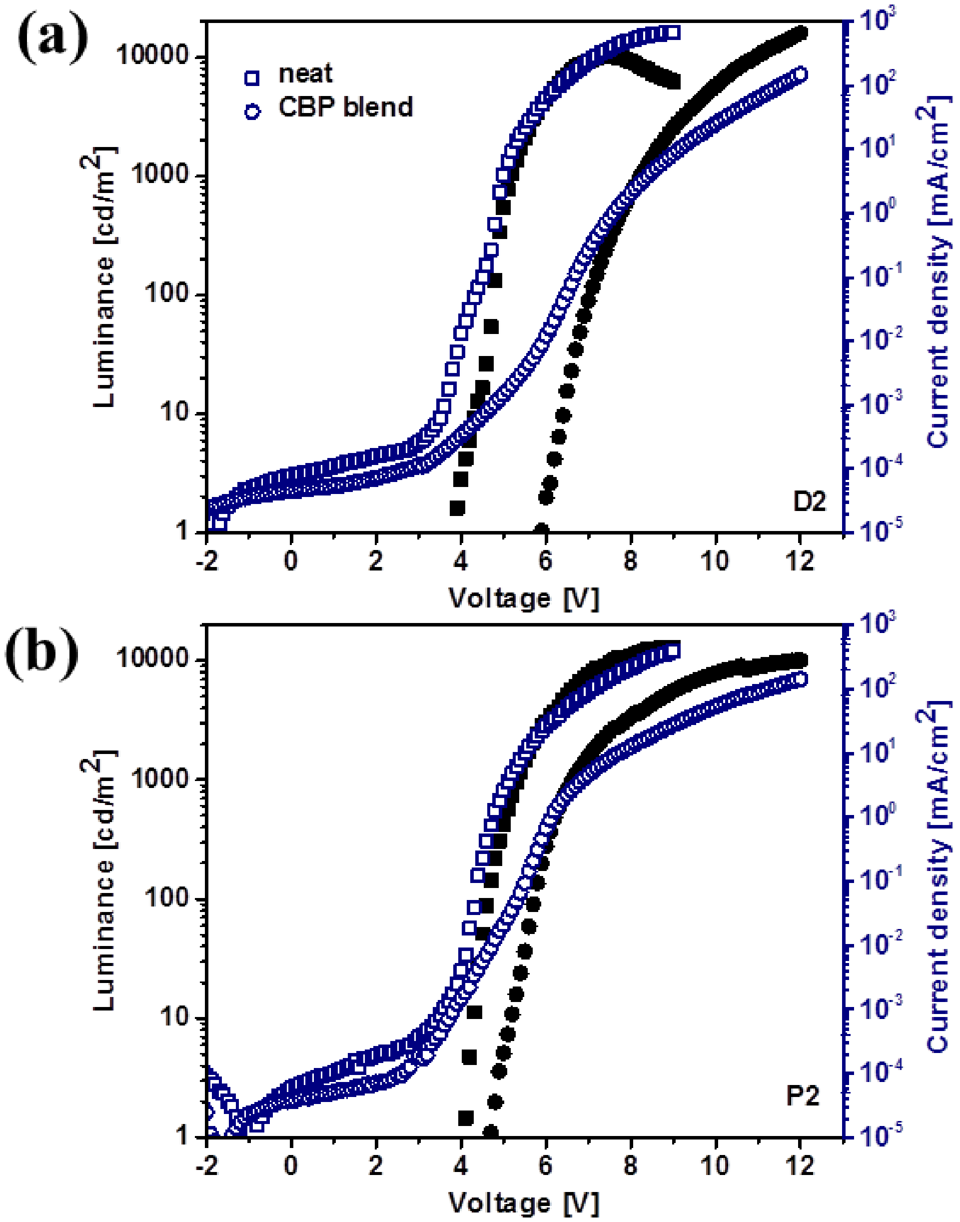

Figure 4.13 Electrical characteristics in neat (square) and CBP blend (circle) devices for doubly-dendronised :a) dendrimer D2, and b)poly(dendrimer) P2.

The EL spectra for performing devices are shown in Figure 4.14 a and b. The shape of EL spectra are in agreement with PL spectra of the same compounds, and also with those of the singly-dendronised compounds (D1 and P1). This indicates that dendronisation doesn't make any change in emissive properties as shown by the PL spectra. However, for the doubly- dendronised compounds, the peak is red-shifted by 20 nm and the yellowish green colour with CIE co-ordinates of (0.46, 0.54) at 1 mA/cm^2 (see Figure 4.14 c and d). These observations are consistent with the photo-physical properties.

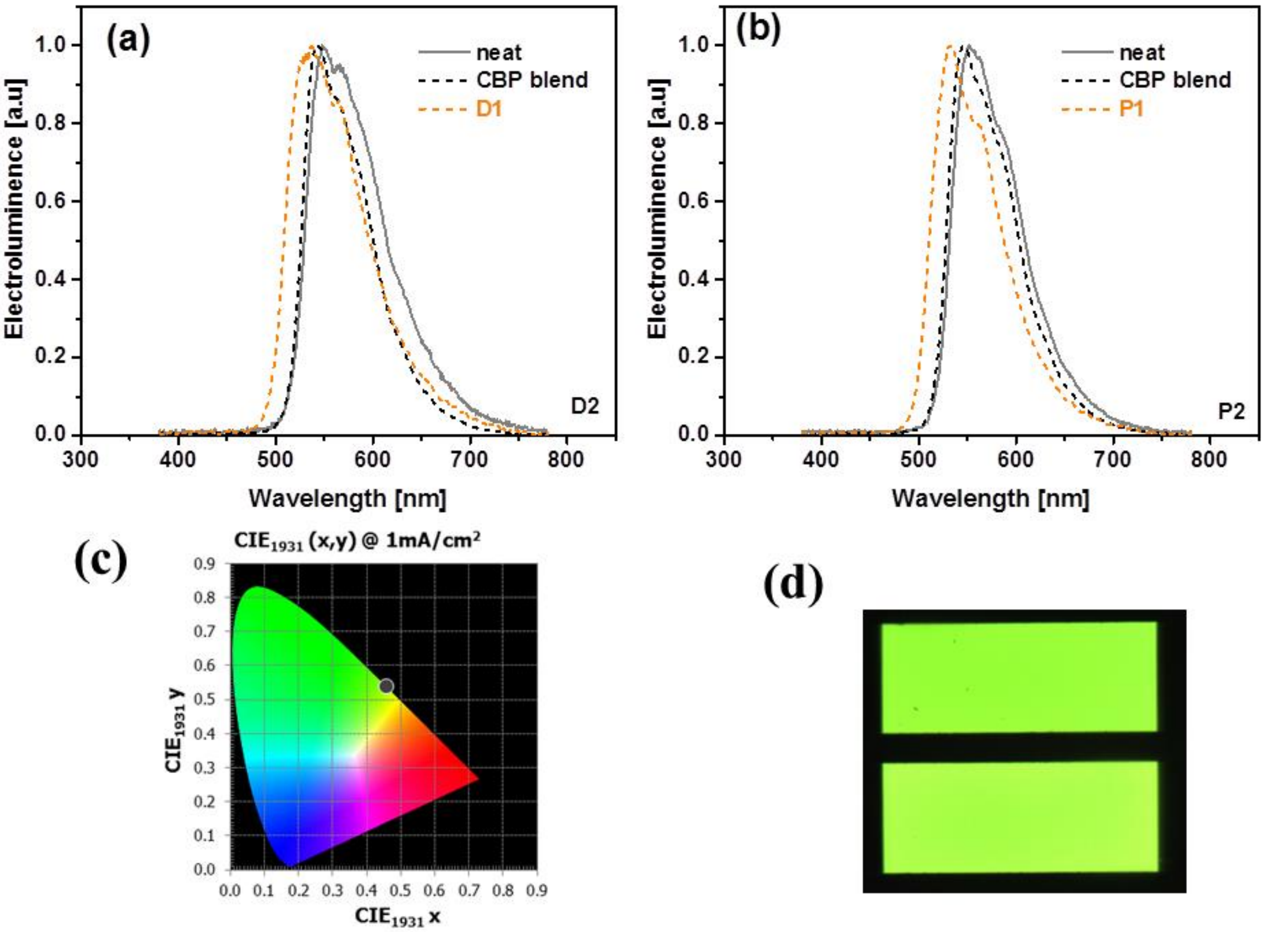

Figure 4.14 Electroluminescent spectrum for doubly-dendronised compounds in neat (solid line), and CBP blend (dotted line) devices: a) D2, b) P2, The EL spectra of their singly-dendronised counterparts are plotted in orange colour as reference, c) CIE co-ordinates, and d) close up of actual performing device.

In order to have a better understanding of the device properties, their efficiencies were plotted in different units (see Figure 4.15). The effect of dendronisation is more noticeable in the neat devices as the EQE increases from 4.5% for D1 to 6% for D2, and the power efficiency increases from 10.2 lm/ W for D1 to 12.8 lm/W for D2.

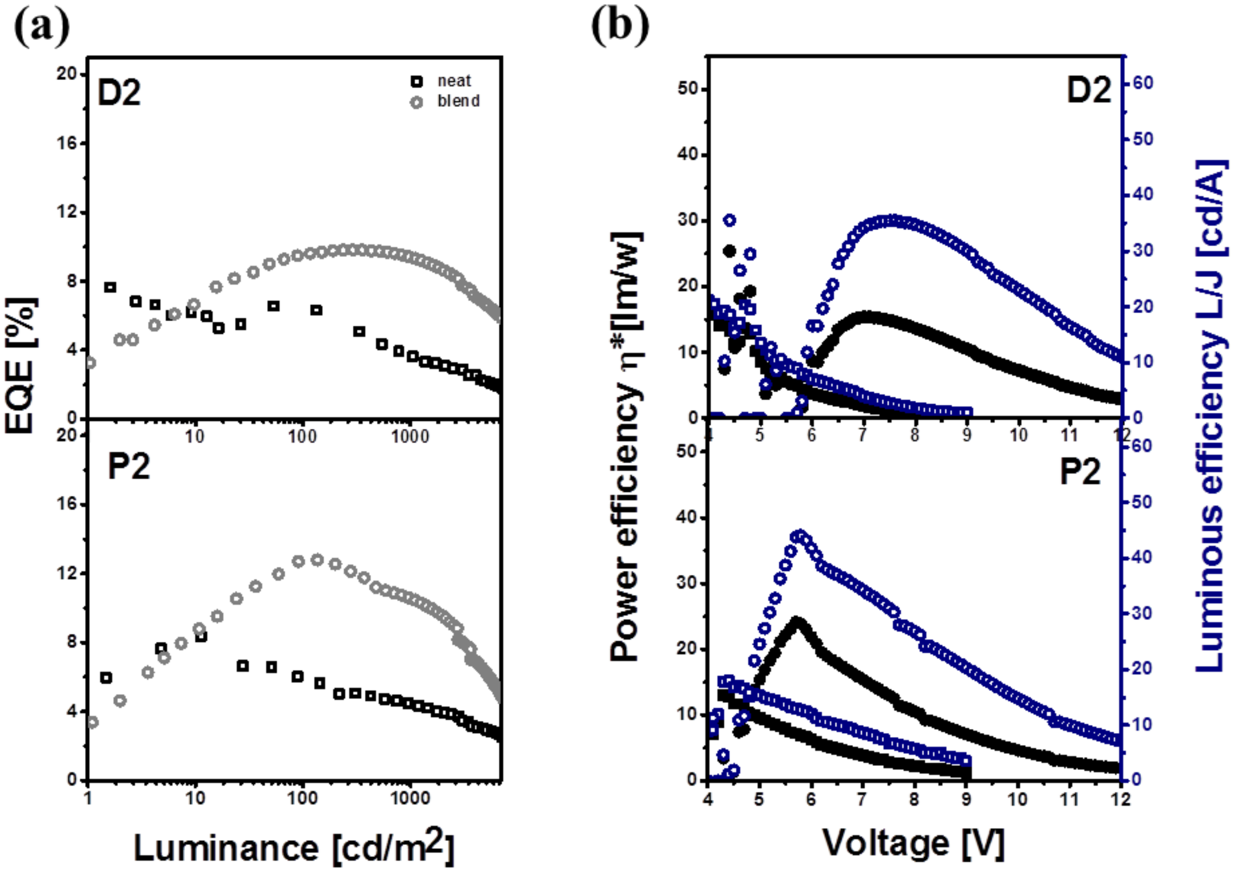

Figure 4.15 Efficiency of devices are presented for D2 and P2 in different units: a) EQE and b) power efficiency (left axis) and luminous efficiency (right axis).

The efficiencies of the singly-dendronised devices are consistent with the measured PLQY values while for doubly-dendronised compounds these values are less than theoretical expectation. Previous studies show that introducing additional dendrons or increasing the dendrimer generation can have different impacts on the charge transport depending on the type of dendron. For example, the first generation singly- and doubly-dendronised $Ir(ppy)_3$ dendrimers with the biphenyl dendron have the same hole mobility, which is double that of second generation singly-dendronised dendrimers[8, 12]. In contrast, attaching a second carbazole based dendron enhances the charge transport in the system by about an order of magnitude due to reduced disorder in the films[31]. Therefore, increasing the hole mobility by one order of magnitude for the doubly-dendronised compounds (D2 and P2) can lead to lower EQEs due to imbalances between the electron- and hole-charges. Moreover, it can affect the film morphology and packing which is also known to play a critical role in organic device performance [32, 33]. A summary of the device performance for the doubly-dendronised compounds D2 and P2 are presented in Table 4.4. The outcoupling values for these devices are not higher than the theoretically expected values. This is why the dipole orientation was not studied for D2 or P2.

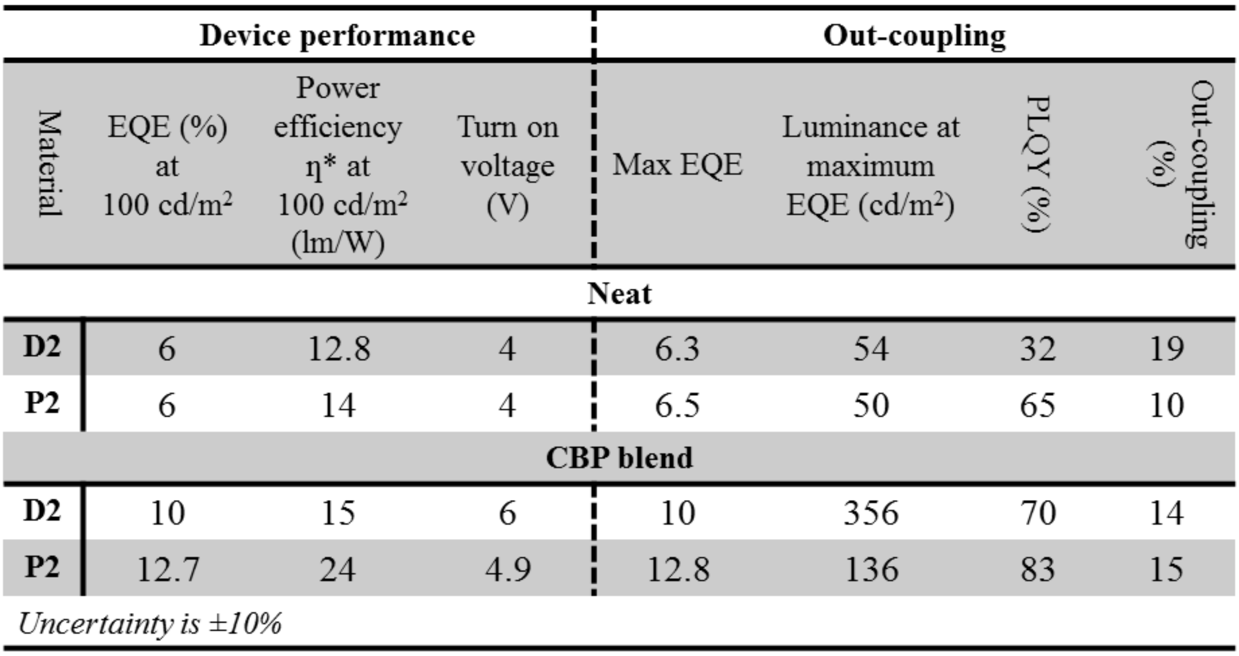

	Device performance			Out-coupling			
Material	EQE (%) at 100 cd/m²	Power efficiency η* at 100 cd/m² (lm/W)	Turn on voltage (V)	Max EQE	Luminance at maximum EQE (cd/m²)	PLQY (%)	Out-coupling (%)
Neat							
D2	6	12.8	4	6.3	54	32	19
P2	6	14	4	6.5	50	65	10
CBP blend							
D2	10	15	6	10	356	70	14
P2	12.7	24	4.9	12.8	136	83	15

Uncertainty is ±10%

Table 4.4 A summary of electrical characterization and outcoupling calculations from doubly-dendronised dendrimer and poly(dendrimer) in devices.

4.4 Conclusion

In this Chapter, a novel approach was described for solution-processable phosphorescent materials for OLED applications by integration of hole-transporting carbazole based Ir_{III} dendrimers into polymer architectures. By increasing the number of dendrons attached to the ligands of Ir_{III} dendrimers, both the intra- and inter-chain inter-chromophore interactions could be controlled by core encapsulation, leading to higher PLQY values in the solid state and longer life times of the emissive species. A drawback of this approach was a red-shift in the emission colour due to an increase in conjugation length of the ligand. This double dendron approach to control optoelectronic properties was also used for poly(dendrimers), providing the extra advantage of better film forming and possibly higher solution viscosity. Although, this family of materials has potential for hostless single layer OLED devices, blended emissive layers showed further reduction in inter-chromophore interaction and concentration quenching. The addition of a second dendron improved the device performance of D2 relative to D1, which is consistent with the expected increase of an order of magnitude in mobility. An excellent EQE result was achieved for singly dendronised poly(dendrimer) (P1) with the maximum EQE of 30% which has not previously been achieved in solution processed OLEDs. This was evidence for horizontally oriented emissive dipoles in the singly dendronised dendrimer D1 and poly(dendrimer) P1, observed initially by an out coupling (25% and 40% respectively) which was higher than the theoretically expected out coupling value (20%). This is a promising achievement as it allows more efficient OLEDs to be realized via modifications made to the intrinsic properties of the material.

In the next Chapter, a systematic study on singly dendronised co-polymers containing both hole- and electron- transporting moieties will be presented in order to investigate the possibility of achieving more efficient devices by balancing the device charge transport via an ambipolar material.

References

[1] K. Brunner, A. van Dijken, H. Börner, J.J. Bastiaansen, N.M. Kiggen, B.M. Langeveld, Carbazole compounds as host materials for triplet emitters in organic light-emitting diodes: tuning the HOMO level without influencing the triplet energy in small molecules, Journal of the American Chemical Society, 126 (2004) 6035-6042.
[2] A. van Dijken, J.J. Bastiaansen, N.M. Kiggen, B.M. Langeveld, C. Rothe, A. Monkman, I. Bach, P. Stössel, K. Brunner, Carbazole compounds as host materials for triplet emitters in organic light-emitting diodes: polymer hosts for high-efficiency light-emitting diodes, Journal of the American Chemical Society, 126 (2004) 7718-7727.
[3] J. Ding, J. Gao, Y. Cheng, Z. Xie, L. Wang, D. Ma, X. Jing, F. Wang, Highly Efficient Green-Emitting Phosphorescent Iridium Dendrimers Based on Carbazole Dendrons, Advanced Functional Materials, 16 (2006) 575-581.
[4] K.A. Knights, S.G. Stevenson, C.P. Shipley, S.-C. Lo, S. Olsen, R.E. Harding, S. Gambino, P.L. Burn, I.D. Samuel, A rapid route to carbazole containing dendrons and phosphorescent dendrimers, Journal of Materials Chemistry, 18 (2008) 2121-2130.
[5] J. Ding, J. Lü, Y. Cheng, Z. Xie, L. Wang, X. Jing, F. Wang, Solution-Processible Red Iridium Dendrimers based on Oligocarbazole Host Dendrons: Synthesis, Properties, and their Applications in Organic Light-Emitting Diodes, Advanced Functional Materials, 18 (2008) 2754-2762.
[6] S.-C. Lo, E. Namdas, P. Burn, I. Samuel, Synthesis and properties of highly efficient electroluminescent green phosphorescent iridium cored dendrimers, Macromolecules, 36 (2003) 9721-9730.
[7] J. Lupton, I. Samuel, R. Beavington, M. Frampton, P. Burn, H. Bässler, Control of mobility in molecular organic semiconductors by dendrimer generation, Physical Review B, 63 (2001) 155206.
[8] J.P. Markham, I.D. Samuel, S.-C. Lo, P.L. Burn, M. Weiter, H. Bässler, Charge transport in highly efficient iridium cored electrophosphorescent dendrimers, Journal of applied physics, 95 (2004) 438-445.
[9] S.C. Lo, T.D. Anthopoulos, E.B. Namdas, P.L. Burn, I.D. Samuel, Encapsulated Cores: Host-Free Organic Light-Emitting Diodes Based on Solution-Processible Electrophosphorescent Dendrimers, Advanced materials, 17 (2005) 1945-1948.
[10] J. Markham, S.-C. Lo, S. Magennis, P. Burn, I. Samuel, High-efficiency green phosphorescence from spin-coated single-layer dendrimer light-emitting diodes, Applied physics letters, 80 (2002) 2645-2647.
[11] S.C. Lo, R.N. Bera, R.E. Harding, P.L. Burn, I.D. Samuel, Solution-Processible Phosphorescent Blue Dendrimers Based on Biphenyl-Dendrons and Fac-tris (phenyltriazolyl) iridium (III) Cores, Advanced Functional Materials, 18 (2008) 3080-3090.
[12] S. Gambino, S.C. Lo, Z. Liu, P.L. Burn, I.D. Samuel, Charge Transport in a Highly Phosphorescent Iridium (III) Complex-Cored Dendrimer with Double Dendrons, Advanced Functional Materials, 22 (2012) 157-165.
[13] W.-Y. Lai, J.W. Levell, M.N. Balfour, P.L. Burn, S.-C. Lo, I.D. Samuel, The ‘double dendron’approach to host free phosphorescent poly (dendrimer) OLEDs, Polymer Chemistry, 3 (2012) 734-740.
[14] T. Shimoda, K. Morii, S. Seki, H. Kiguchi, Inkjet printing of light-emitting polymer displays, Mrs Bulletin, 28 (2003) 821-827.
[15] M. Singh, H.M. Haverinen, P. Dhagat, G.E. Jabbour, Inkjet printing-process and its applications, Advanced materials, 22 (2010) 673.
[16] J.P. Gunning, J.W. Levell, M.F. Wyatt, P.L. Burn, J. Robertson, I.D. Samuel, The development of poly (dendrimer) s for advanced processing, Polymer Chemistry, 1 (2010) 730-738.
[17] W.-Y. Lai, M.N. Balfour, J.W. Levell, A.K. Bansal, P.L. Burn, S.-C. Lo, I.D. Samuel, Poly (dendrimers) with phosphorescent iridium (III) complex-based side chains prepared via ring-opening metathesis polymerization, Macromolecules, 45 (2012) 2963-2971.

[18] W.-Y. Lai, J.W. Levell, A.C. Jackson, S.-C. Lo, P.V. Bernhardt, I.D. Samuel, P.L. Burn, A phosphorescent poly (dendrimer) containing iridium (III) complexes: synthesis and light-emitting properties, Macromolecules, 43 (2010) 6986-6994.
[19] K.O. Kim, T.-L. Choi, Synthesis of Dendronized Polymers via Macromonomer Approach by Living ROMP and Their Characterization: From Rod-Like Homopolymers to Block and Gradient Copolymers, Macromolecules, 46 (2013) 5905-5914.
[20] K.O. Kim, T.-L. Choi, Synthesis of rod-like dendronized polymers containing G4 and G5 ester dendrons via macromonomer approach by living ROMP, ACS Macro Letters, 1 (2012) 445-448.
[21] X. Chen, J.-L. Liao, Y. Liang, M. Ahmed, H.-E. Tseng, S.-A. Chen, High-efficiency red-light emission from polyfluorenes grafted with cyclometalated iridium complexes and charge transport moiety, Journal of the American Chemical Society, 125 (2003) 636-637.
[22] N.R. Evans, L. Sudha Devi, C.S. Mak, S.E. Watkins, S.I. Pascu, A. Köhler, R.H. Friend, C.K. Williams, A.B. Holmes, Triplet energy back transfer in conjugated polymers with pendant phosphorescent iridium complexes, Journal of the American Chemical Society, 128 (2006) 6647-6656.
[23] V. Jankus, C. Winscom, A.P. Monkman, The photophysics of singlet, triplet, and degradation trap states in 4, 4-N, N′-dicarbazolyl-1, 1′-biphenyl, The Journal of chemical physics, 130 (2009) 074501.
[24] W. Brütting, J. Frischeisen, T.D. Schmidt, B.J. Scholz, C. Mayr, Device efficiency of organic light-emitting diodes: Progress by improved light outcoupling, physica status solidi (a), 210 (2013) 44-65.
[25] Y. Sakai, M. Shibata, D. Yokoyama, Simple model-free estimation of orientation order parameters of vacuum-deposited and spin-coated amorphous films used in organic light-emitting diodes, Applied Physics Express, 8 (2015) 096601.
[26] L. Zhao, T. Komino, M. Inoue, J.-H. Kim, J.C. Ribierre, C. Adachi, Horizontal molecular orientation in solution-processed organic light-emitting diodes, Applied Physics Letters, 106 (2015) 063301.
[27] C.-K. Moon, K.-H. Kim, J.W. Lee, J.-J. Kim, Influence of host molecules on emitting dipole orientation of phosphorescent iridium complexes, Chemistry of Materials, 27 (2015) 2767-2769.
[28] M.J. Jurow, C. Mayr, T.D. Schmidt, T. Lampe, P.I. Djurovich, W. Brütting, M.E. Thompson, Understanding and predicting the orientation of heteroleptic phosphors in organic light-emitting materials, Nature materials, (2015).
[29] C. Adachi, M.A. Baldo, S.R. Forrest, M.E. Thompson, High-efficiency organic electrophosphorescent devices with tris (2-phenylpyridine) iridium doped into electron-transporting materials, Applied Physics Letters, 77 (2000) 904.
[30] E.B. Namdas, A. Ruseckas, I.D. Samuel, S.-C. Lo, P.L. Burn, Photophysics of fac-tris (2-phenylpyridine) iridium (III) cored electroluminescent dendrimers in solution and films, The Journal of Physical Chemistry B, 108 (2004) 1570-1577.
[31] S. Gambino, S.G. Stevenson, K.A. Knights, P.L. Burn, I.D. Samuel, Control of Charge Transport in Iridium (III) Complex-Cored Carbazole Dendrimers by Generation and Structural Modification, Advanced Functional Materials, 19 (2009) 317-323.
[32] P. Wolfer, A. Armin, A. Pivrikas, M. Velusamy, P.L. Burn, P. Meredith, Solution structure: defining polymer film morphology and optoelectronic device performance, J. Mater. Chem. C, 2 (2013) 71-77.
[33] A. Armin, P. Wolfer, P.E. Shaw, M. Hambsch, F. Maasoumi, M. Ullah, E. Gann, C.R. McNeill, J. Li, Z. Shi, Simultaneous enhancement of charge generation quantum yield and carrier transport in organic solar cells, Journal of Materials Chemistry C, 3 (2015) 10799-10812.
[34] S.G. Stevenson, Dendrimer light-emitting diodes, in, University of St Andrews, 2008.

Chapter 5

Ambipolar Poly(dendrimer) OLEDs

5.1 Introduction

Phosphorescent poly(dendrimers) have the potential to be applied in large area OLED display applications because of their efficient photo-physical properties and solution processability. Their solution processability provides engineering advantages so that film deposition can be achieved via wet processes such as large area screen or ink-jet printing. In the previous chapter, poly(dendrimers) containing a carbazole moiety as the hole transport dendron showed promising device performance. However, to achieve the necessary high device efficiencies, it would be ideal to develop ambipolar polymeric materials that contain both an electron- and hole- transporting moiety to improve recombination efficiency.

Several reports have shown the beneficial effects of doping polymeric hole transport materials with oxadiazole electron transport molecules [1, 2]. Combinations of carbazole and oxadiazole derivatives have also been shown to be widely used as a suitable choice for ambipolar host materials. There are different approaches to incorporate both moieties: blends of small molecule or polymeric derivatives of oxadiazole with polymeric carbazole derivatives[3-8], host polymers with a carbazole backbone and oxadiazole pendants[9], block and random copolymers of carbazole and oxadiazole based monomers as a host material[10], and conjugated or non-conjugated host molecules of carbazole and oxadiazole moieties[11-15] for example.

On the other hand, blending two host materials or an ambipolar host material with a phosphorescent iridium complex can lead to phase separation. To address this issue, single co-polymers containing carbazole and oxadiazole moieties and a phosphorescent iridium complex were designed to retain both charge transport (electron and hole) and triplet harvesting properties. This chapter contains photo-physical and OLED device characterization of the block co-polymer and random copolymer containing carbazole and oxadiazole moieties.

5.2 Material design and experimental methods

Figure 5.1.a and b show the block co-polymer (B) and random co-polymer (R) that were used in the work described in this chapter. These two materials have the same chemical units consisting of a phosphorescent iridium complex with a carbazole dendron and an oxadiazole unit (in pink), both directly attached to a non-conjugated polymer back bone. In block co-polymer (B) alternating sections of the polymer chain consist of either all oxadiazole units or the iridium core with carbazole dendrons. However, in the random co-polymer (R) the oxadiazole and iridium core/carbazole units are attached to the polymer back bone completely randomly. In addition, two small molecules commercially available from Lumtec, 4,4'-N,N'-dicarbazolyl-biphenyl (CBP) and 2,2',2"-(1,3,5-Benzinetriyl)-tris(1-phenyl-1-H-benzimidazole) (TPBi) were used as a host and electron transport materials, respectively. The structure of these can be seen in Chapter 3, Figure 3.1.b and c.

The photo-physical characterisation was performed on degassed optically dilute solutions and solid state films (neat and blend) as detailed in Chapter 2. Neat films were spin cast from a 15 mg/ml and 18 mg/ml concentrations respectively for B and R compounds, while for blends the dopant ratio was 20 wt%. The thicknesses of the solid state samples for photophysical testing were identical to those used in devices. Due to their high molecular weight, both co-polymers were stirred into the solvent overnight prior to the deposition to ensure they had fully dissolved.

Devices (see Figure 5.2.a) were fabricated on pre-patterned ITO substrates with 170 nm of ITO thickness and 10 Ω/sq sheet resistance. Substrates were pre-cleaned with isopropanol and DI water and then treated with UV-ozone for 15 minutes at 25°C immediately prior to the deposition of next layer. A 30nm PEDOT:PSS film was then deposited and annealed for 15min at 150° C. The PEDOT:PSS was used to ease the injection according to the energy level diagram (see Figure 5.2.b). Devices were then transferred into a nitrogen-filled glovebox where the emissive layers (neat or blend) were deposited on the substrates by spin-coating (2100 rpm) from the overnight stirred solutions. The film thickness (~ 70-80 nm) used in photo-physical characterisation was used in device fabrication. Chlorobenzene and chloroform were used as the solvents for these devices for neat and blend films, respectively.

Finally, successive layers of TPBi (35 nm), LiF, and Al were deposited using thermal evaporation through shadow masks in a vacuum chamber under a base pressure of around 5×10^{-6}mbar. The deposition rate for the TPBi layer was maintained at approximately 1 Å/s. The cathode layers, LiF (1 nm) and Al (100 nm), were then sequentially deposited without breaking the vacuum, using a second shadow mask. These cathode layers were selected according to the appropriate energy levels in the device. Completed devices were transferred under an inert atmosphere from the vacuum chamber to a glovebox (water and oxygen concentration levels < 0.1 ppm) for encapsulation with a glass cover using UV cured epoxy resin and an adhesive desiccant. Encapsulated devices were then transferred outside of glovebox for characterisation as explained in Chapter 2.

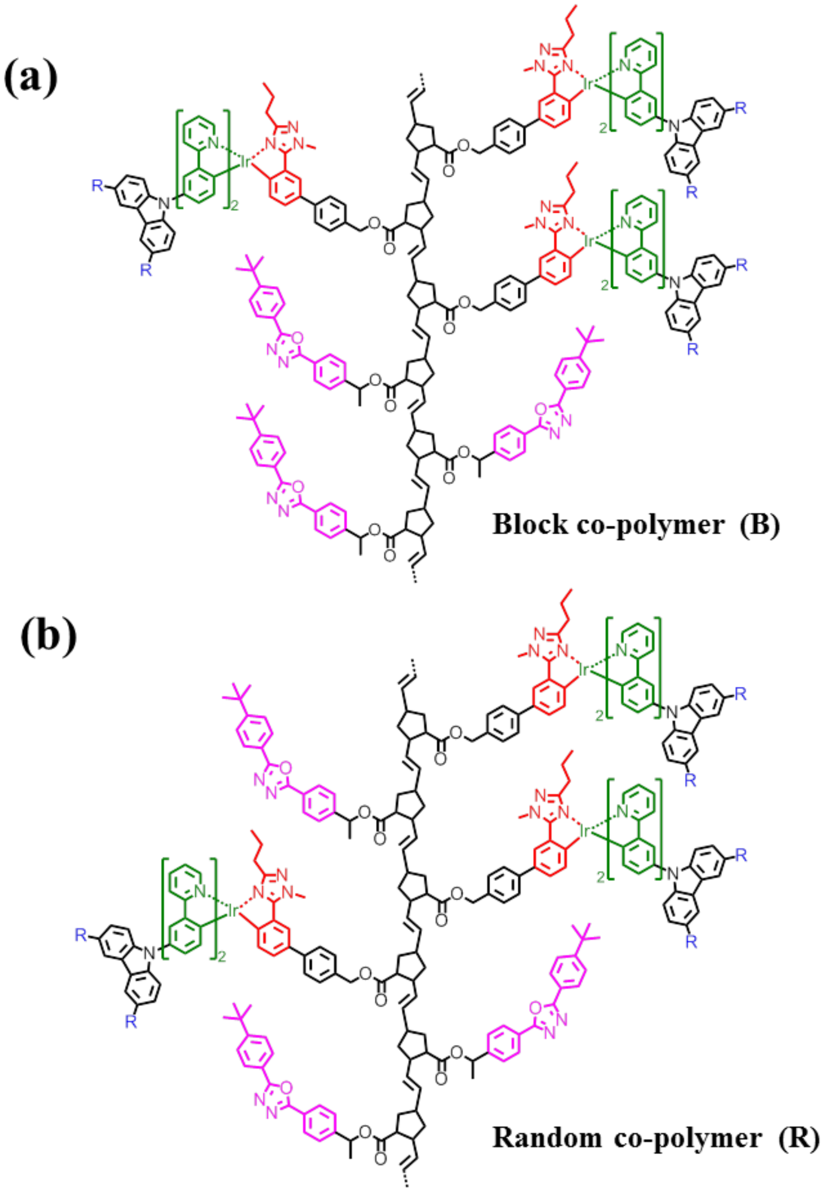

Figure 5.1 Chemical structures of a) block co-polymer with $\bar{M}_w$ of 640 kDa and a polydispersity (PDI) of 6.3 (B), b) random co-polymer (R) with $\bar{M}_w$ of 360 kDa and a polydispersity (PDI) of 3.7. The hole transport dendron (carbazole) are attached to iridium core and electron transport moieties (oxadiazole) are presented in pink.

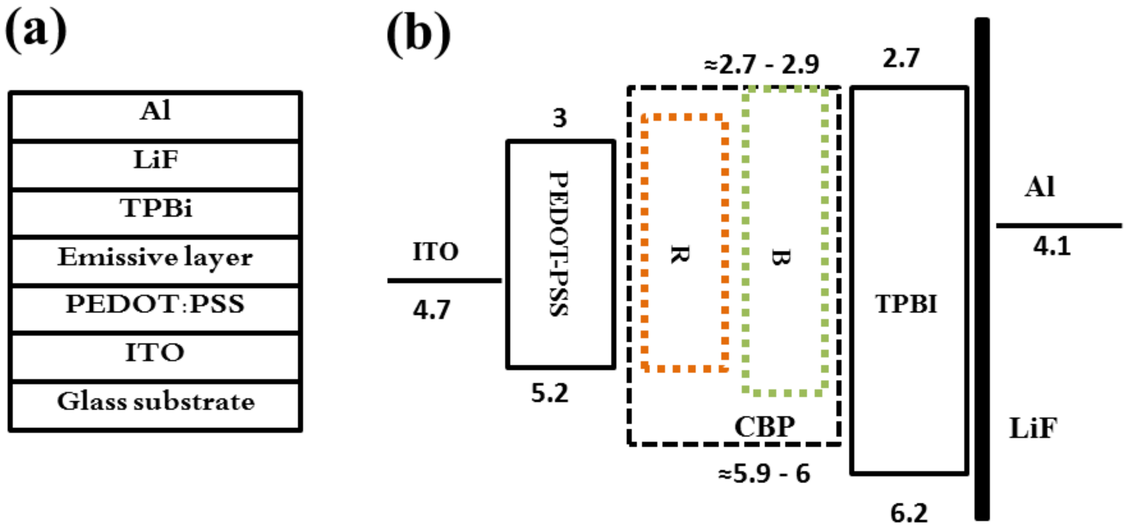

Figure 5.2 a) device structure, b) energy diagram for different layers. The cathode and transport materials were selected to match the HOMO/LUMO levels of the copolymers. The HOMO and LUMO of TPBi and CBP were taken from literature respectively [16, 17]. The work function for metals were taken from original material sheet provided by CSIRO, the energy level of co-polymers were obtained from PESA measurements as explained in Chapter 2.

5.3 Photo-physical properties

As a first step of the characterization, PESA measurements were conducted for co-polymers. The measured HOMO energy levels for the block and random co-polymers were 5.3 and 5.2 eV respectively. These values are slightly lower than poly(dendrimer) P1 without the oxadiazole as the electron transport moiety which was 5.4 eV.

The absorption and PL spectra for the co-polymer family are shown in Figure 5.3. The absorption spectra were identical to poly(dendrimer) P1 presented in Chapter 4 with similar main regions of singlet-singlet $\pi - \pi^*$ absorption and metal to ligand charge transfer.

The PL spectra for the co-polymer family in solution and CBP blend were similar to the singly dendronised counterparts in Chapter 4 with the main emission peak at 520 nm coming from the phosphorescent emission of Ir III complex. The result suggests that adding the electron transport moiety didn't change the main emission in the compounds. The red shift of solid state spectra in each compound was anticipated due to a decrease of freedom in comparison with solution. However, the neat film of the block co-polymer showed an extra emission at 375 nm which is from accumulation of oxadiazole moieties. This peak became more intense in the CBP blend film as the CBP emission was added (see Figure 5.3.c). Moreover, this indicates that the block co-polymer had a wider optical band gap of 3.2 eV in comparison with random co-polymer (2.6 eV).

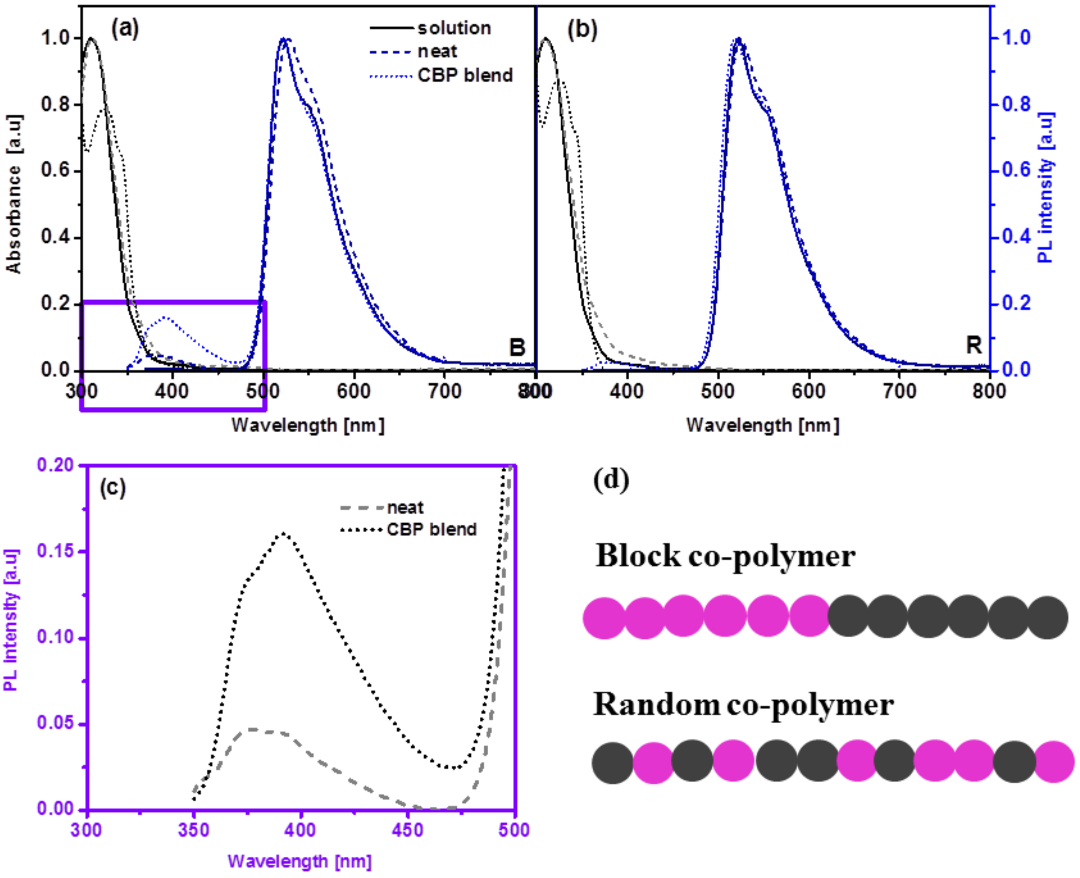

Figure 5.3 normalized absorption and PL spectra for a) block co-polymer (B), b) random co-polymer (R), c) a zoom in for part of PL spectra of block co-polymer (B), for solution (solid line), neat (dash line), and CBP blend films (dot line), d) a schematic diagram for block and random co-polymers. The pink and black circles are representative for electron (oxadiazole) - and hole-transporting (Ir- carbazole dendrimer) moieties respectively.

PL intensity and PLQY measurements were also performed on all compounds (see Figure 5.4). Unlike the singly dendronised poly(dendrimer) in the previous chapter, the co-polymers' lifetimes in solution decayed biexponentially. This suggests that adding the electron transport moiety increased the interchange interaction leading to quenching of the photoluminescence even in diluted solutions. This effect was more destructive in the block co-polymer decreasing the slower component lifetime from 1.5 µs for the random co-polymer to 1.2 µs. There were two possible explanation this; accumulation of chromophore cores at one side of the polymer back bone, and the barrier for energy transfer from the oxadiazole moieties to the Ir- carbazole dendrimer when the moieties are completely separated (see Figure 5.3.d). These results are in agreement with PLQY data which are summarized in Table 5.1 and an extra emission peak in PL spectrum at 375 nm for block co-polymer (see Fig 5.3.c)

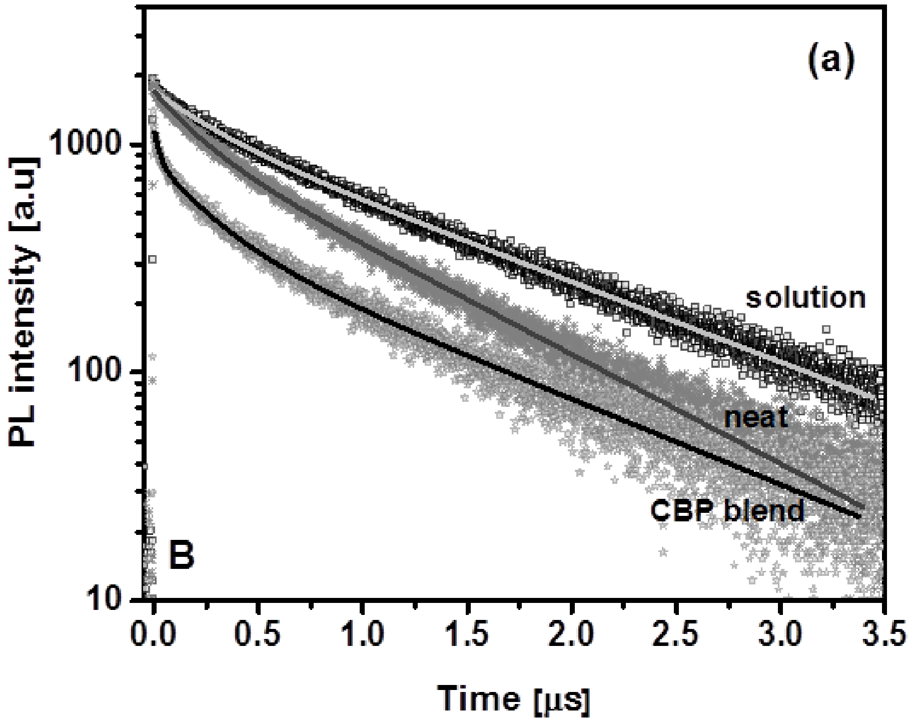

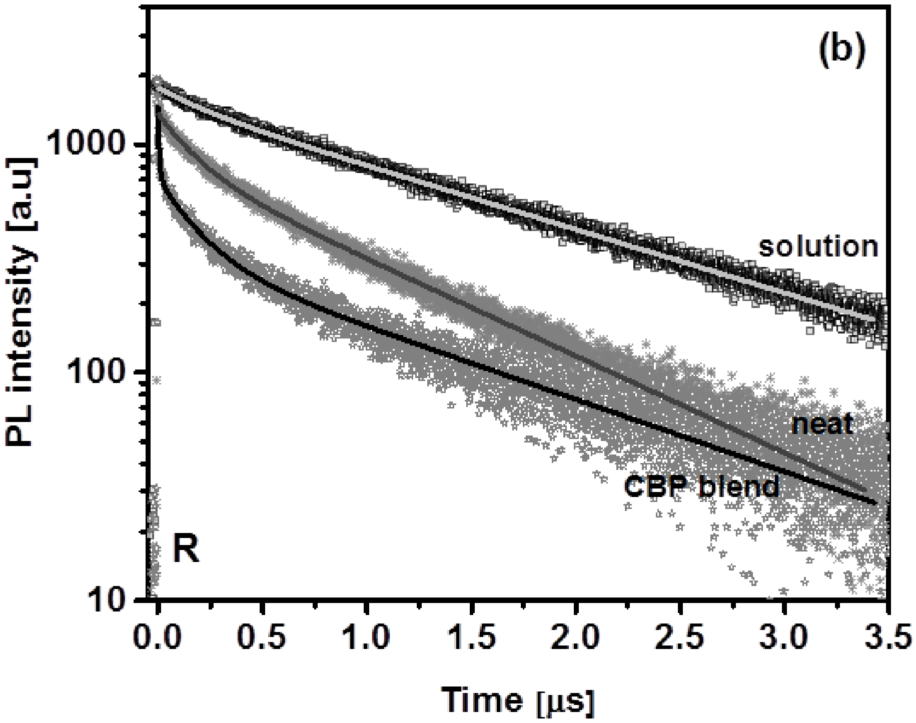

Figure 5.4 Lifetime measurements (TSPC) for a) block co-polymer (B), and b) random co-polymer (R) in degassed solution, neat, and CBP blend. The samples were excited by a 372 nm LED and the emission was detected at the peak of PL spectra (520-525 nm).

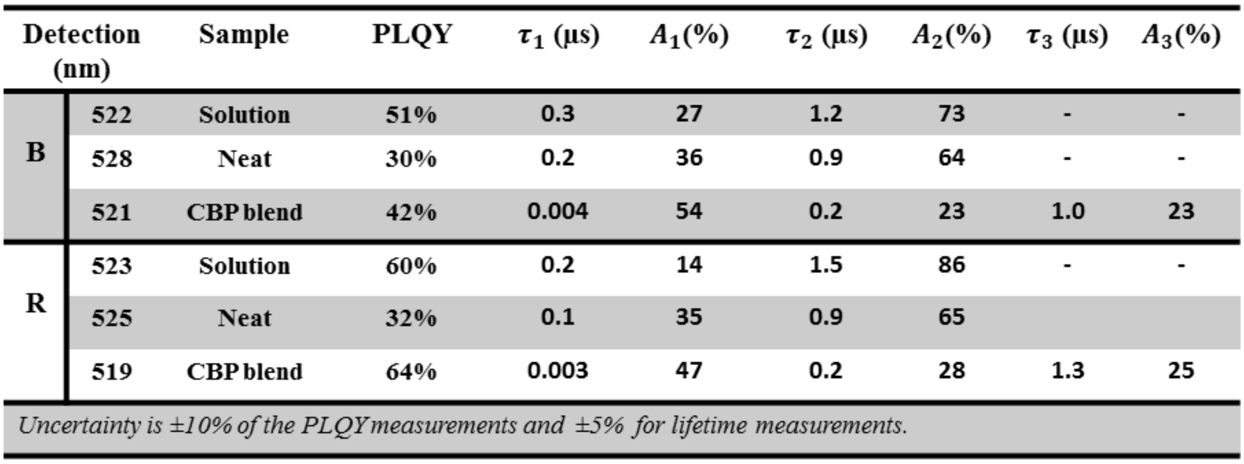

Detection (nm)		Sample	PLQY	τ_1 (μs)	A_1(%)	τ_2 (μs)	A_2(%)	τ_3 (μs)	A_3(%)
B	**522**	**Solution**	**51%**	**0.3**	**27**	**1.2**	**73**	**-**	**-**
	528	**Neat**	**30%**	**0.2**	**36**	**0.9**	**64**	**-**	**-**
	521	**CBP blend**	**42%**	**0.004**	**54**	**0.2**	**23**	**1.0**	**23**
R	**523**	**Solution**	**60%**	**0.2**	**14**	**1.5**	**86**	**-**	**-**
	525	**Neat**	**32%**	**0.1**	**35**	**0.9**	**65**		
	519	**CBP blend**	**64%**	**0.003**	**47**	**0.2**	**28**	**1.3**	**25**

Uncertainty is ±10% of the PLQY measurements and ±5% for lifetime measurements.

Table 5.1 A summary of the photo-physical characteristics for the co-polymer family in solution, neat films, and CBP blends.

Interchain, interchromophore interactions were more noticeable in the block co-polymer as the PLQY values were slightly smaller with more quenching between emissive species due to accumulation of chromophore cores. Although introducing more space between chromophores by doping with more of the carbazole moiety of CBP in the blends seemed to increase PLQY values, the solid state blends still had three emissive species involved in non-radiative recombination. This indicated that the interaction was not completely under control.

5.4 Device performance

In order to investigate the electroluminescence properties of the materials' performance, devices were fabricated using neat and blend films as described previously. In neat devices, the block co-polymer presented better performance with turn on voltage 4V and EQE of 4.8 % in comparison with 6.3 V and 4 % for the random co-polymer. In blend devices, the turn on voltage remained lower for the block co-polymer while the EQE improved for the random co-polymer with 10 % in comparison with the block co-polymer 8 %. From electrical characterisation (see Figure 5.5) of these devices, it can be seen that the block co-polymer was superior in neat devices than the random co-polymer. This could be due to improved ambipolar charge transport in the block co-polymer as similar moieties are next to each other; while in random co-polymer the randomly distributed electron and hole moieties act like trapping centres for charge transport (see Figure 5.3.d). However, in the blend system, (see Figure 5.5.b), the trapping effect in the random co-polymer was not dominant due to the large ratio (80%) of CBP. The slightly better performance of the random co-polymer in the CBP blend was likely due to high PLQY. Devices using the block co-polymer (see Figure 5.5.a) had a lower turn on voltage for both neat and blended films. The abrupt increase in current density also suggests an ease of injection, and better interface formation with this compound. This was anticipated from better energy match of the LUMO in compound B.

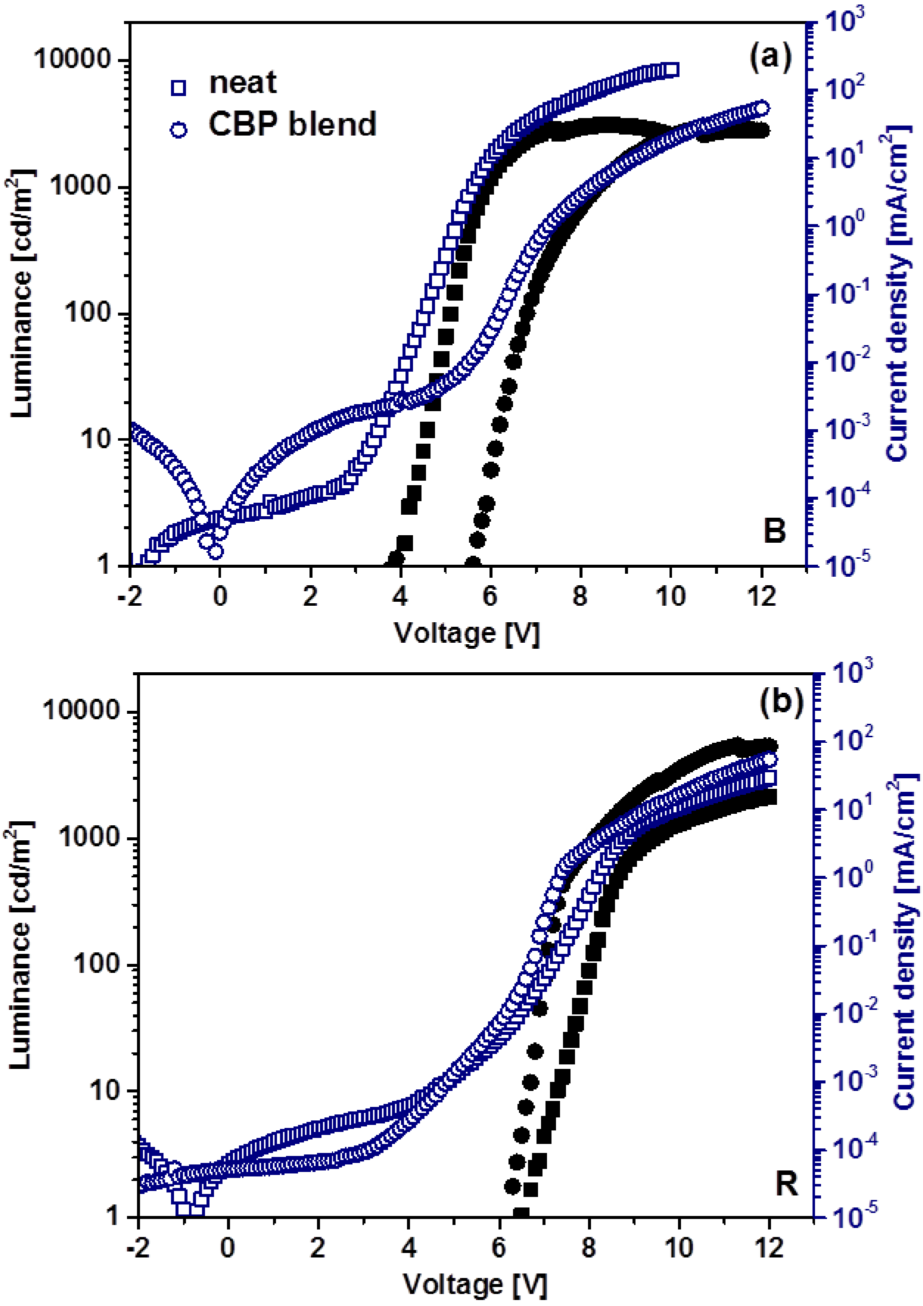

Figure 5.5 Current density and luminance characteristics for a) the block co-polymer (B) with separate distribution of electron- and hole-transporting moieties, b) the random co-polymer (R) with random distribution of oxadiazole group to the polymer back bone.

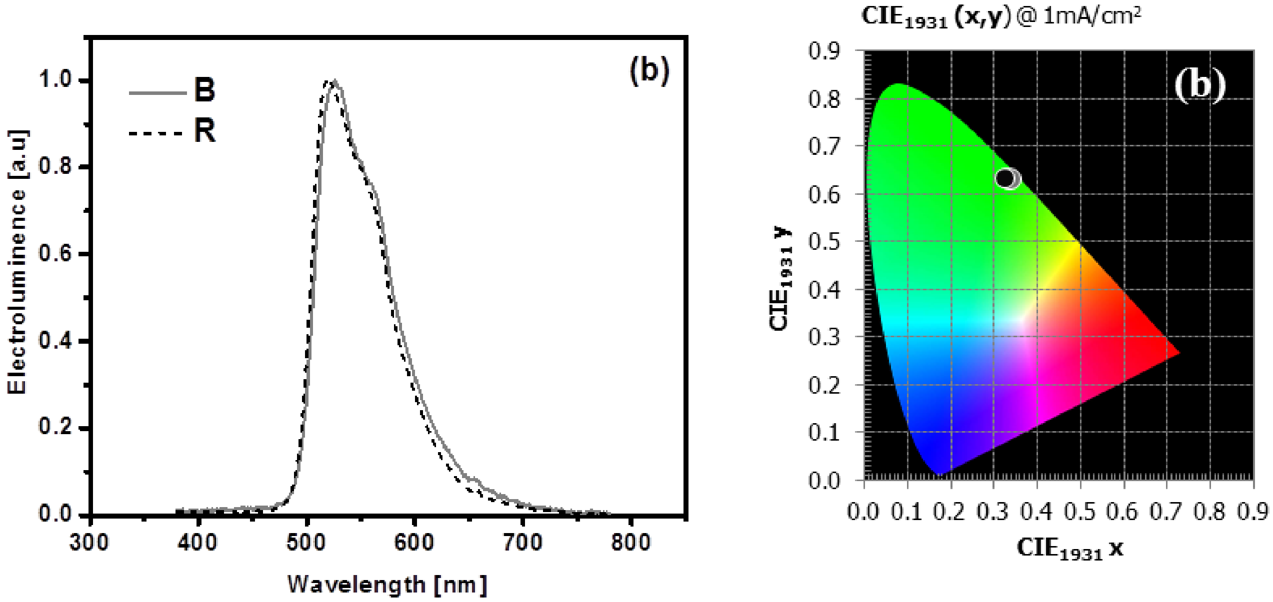

Figure 5.6 a) Electroluminescent for three compounds in blends, b) CIE co-ordinates for both co-polymers.

Figure 5.6.a shows similar EL spectra for both compounds due to the similar chromophore that they share. The maximum peak of the emission at 520 nm indicated no change in photo physical properties in transitioning from films into actual devices. The CIE co-ordinates of both materials are shown in Figure 5.6.b with similar green emission and about (0.32, 0.63).

The EQE values for all devices are presented in Figure 5.7.a. Blends had higher EQE values which was due to higher PLQYs. This was from introducing more space between chromophores leading to less concentration quenching. However, the abrupt increase at the beginning of the EQE trends for blends suggested the presence of an injection barrier in blended devices, which could be due to a bigger energy difference between PEDOT: PSS and the blended emissive layer. The same effect has been observed in the work presented in previous chapters. The out-coupling parameters were calculated at the maximum EQE of the devices, with the recombination rate assumed to be 100% due to balance between charge carrier types. None of the out-coupling values exceeded the theoretical limit; therefore no further investigation for dipole alignment was processed. A summary of the optical and electrical characterisation of the devices is provided in Table 5.2. Power and luminous efficiency were also calculated for all of the devices, with the results shown in Figure 5.7.b. As can be seen, the random co-polymer had slightly more efficient devices in the blend films, with 15.5 lm/W at 100 cd/m^2.

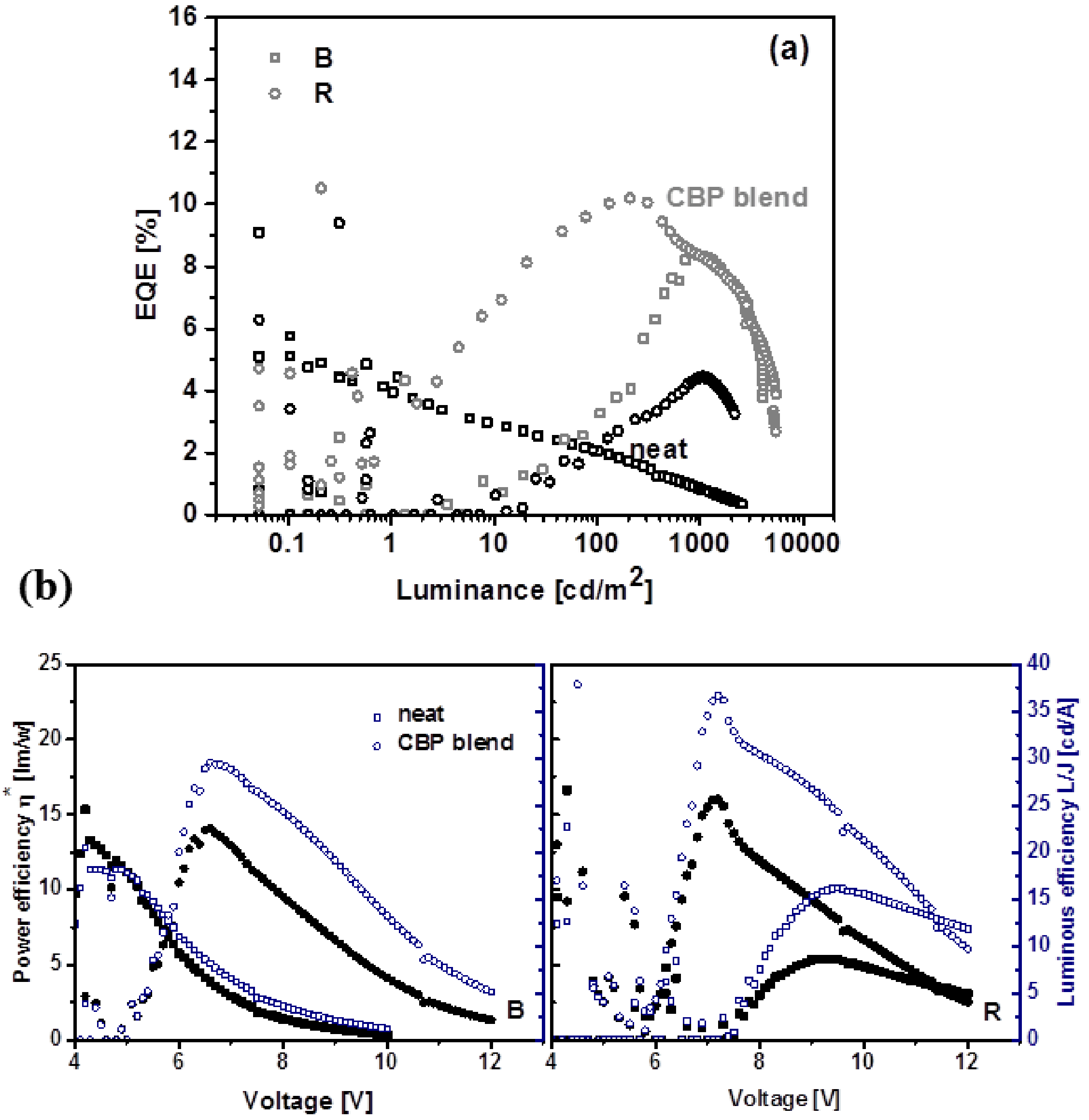

Figure 5.7 a) EQE values for block co-polymer (square) and random co-polymer (circle) in neat (black colour) and blend (grey colour), b) power efficiency and luminous efficiency for both compounds.

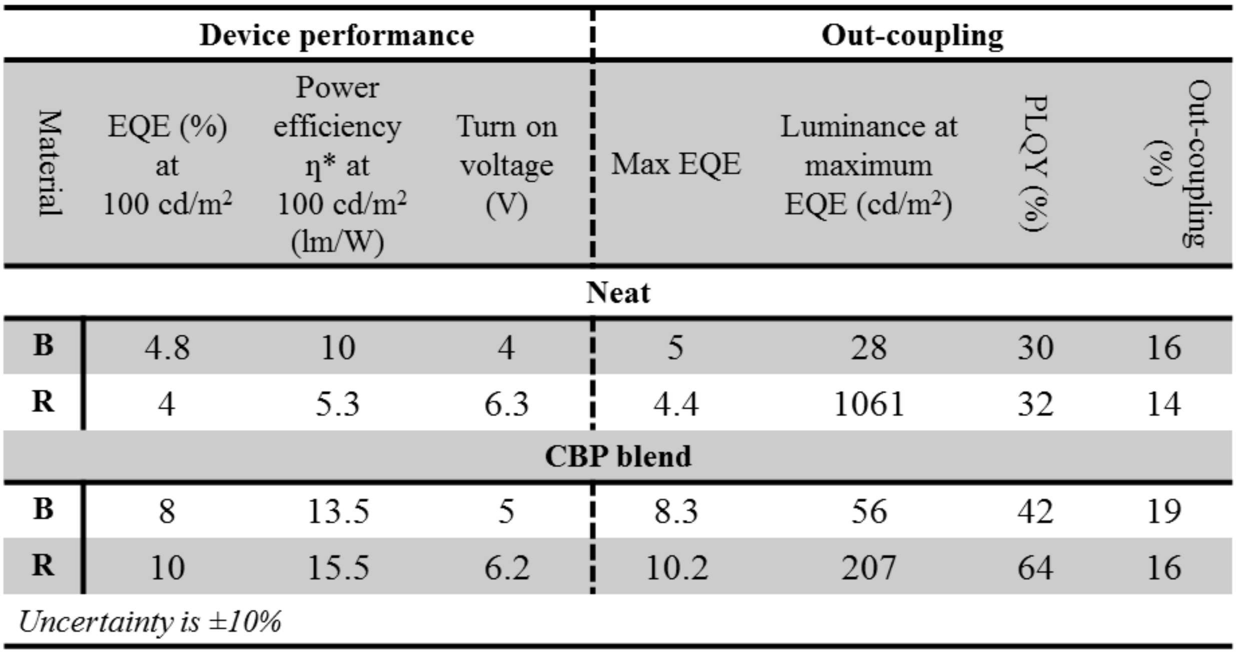

Device performance				Out-coupling			
Material	EQE (%) at 100 cd/m^2	Power efficiency η* at 100 cd/m^2 (lm/W)	Turn on voltage (V)	Max EQE	Luminance at maximum EQE (cd/m^2)	PLQY (%)	Out-coupling (%)
Neat							
B	4.8	10	4	5	28	30	16
R	4	5.3	6.3	4.4	1061	32	14
CBP blend							
B	8	13.5	5	8.3	56	42	19
R	10	15.5	6.2	10.2	207	64	16

Uncertainty is ±10%

Table 5.2 A summary of device performance (left side) and out-coupling values (right side) for devices of both compounds.

5.5 Conclusion

In this Chapter, a new approach was described for solution-processable ambipolar poly(dendrimer) phosphorescent materials for OLED applications. This was achieved by the integration of electron-transporting moieties (oxadiazole) into a carbazole based poly(dendrimer). The electron transport moieties were distributed in two different ways: a block co-polymer with separated phase of electron and hole moieties, and a random co-polymer with random distribution of both moieties. The PLQY values suggested better photo-physical properties for the co-polymer with random distribution. However in neat devices, the block co-polymer presented better performances with lower turn on voltages and better EQE, this was due to ambipolar transport with less trapping effects. The device performance in blended devices was more promising for random co-polymer due to better PLQY.

In next Chapter, the first temperature-dependent measurement on LEFET structure will be detailed. LEFETs have been chosen as suitable device structure for this study, providing simultaneous study of charge injection, photo-physics, and recombination in semiconductors.

References:

[1] C. Jiang, W. Yang, J. Peng, S. Xiao, Y. Cao, High-efficiency, saturated red-phosphorescent polymer light-emitting diodes based on conjugated and non-conjugated polymers doped with an Ir complex, Advanced Materials, 16 (2004) 537-541.
[2] X. Gong, M.R. Robinson, J.C. Ostrowski, D. Moses, G.C. Bazan, A.J. Heeger, High-Efficiency Polymer-Based Electrophosphorescent Devices, Advanced Materials, 14 (2002) 581-585.
[3] C. Adachi, R. Kwong, S.R. Forrest, Efficient electrophosphorescence using a doped ambipolar conductive molecular organic thin film, Organic Electronics, 2 (2001) 37-43.
[4] S. Lamansky, P.I. Djurovich, F. Abdel-Razzaq, S. Garon, D.L. Murphy, M.E. Thompson, Cyclometalated Ir complexes in polymer organic light-emitting devices, Journal of applied physics, 92 (2002) 1570-1575.
[5] X. Yang, F. Jaiser, S. Klinger, D. Neher, Blue polymer electrophosphorescent devices with different electron-transporting oxadiazoles, Applied physics letters, 88 (2006) 021107.
[6] X. Yang, D. Muller, D. Neher, K. Meerholz, Highly efficient polymeric electrophosphorescent diodes, Advanced Materials, 18 (2006) 948-954.
[7] K. Zhang, Z. Chen, C. Yang, X. Zhang, Y. Tao, L. Duan, L. Chen, L. Zhu, J. Qin, Y. Cao, Improving the performance of phosphorescent polymer light-emitting diodes using morphology-stable carbazole-based iridium complexes, Journal of Materials Chemistry, 17 (2007) 3451-3460.
[8] S.-J. Kim, Y. Zhang, C. Zuniga, S. Barlow, S.R. Marder, B. Kippelen, Efficient green OLED devices with an emissive layer comprised of phosphor-doped carbazole/bis-oxadiazole side-chain polymer blends, Organic Electronics, 12 (2011) 492-496.
[9] K. Zhang, Y. Tao, C. Yang, H. You, Y. Zou, J. Qin, D. Ma, Synthesis and properties of carbazole main chain copolymers with oxadiazole pendant toward bipolar polymer host: tuning the HOMO/LUMO level and triplet energy, Chemistry of Materials, 20 (2008) 7324-7331.
[10] L. Deng, P.T. Furuta, S. Garon, J. Li, D. Kavulak, M.E. Thompson, J.M. Fréchet, Living radical polymerization of bipolar transport materials for highly efficient light emitting diodes, Chemistry of materials, 18 (2006) 386-395.
[11] M. Guan, Z. Chen, Z. Bian, Z. Liu, Z. Gong, W. Baik, H. Lee, C. Huang, The host materials containing carbazole and oxadiazole fragment for red triplet emitter in organic light-emitting diodes, Organic electronics, 7 (2006) 330-336.
[12] M.-k. Leung, C.-C. Yang, J.-H. Lee, H.-H. Tsai, C.-F. Lin, C.-Y. Huang, Y.O. Su, C.-F. Chiu, The unusual electrochemical and photophysical behavior of 2, 2'-bis (1, 3, 4-oxadiazol-2-yl) biphenyls, effective electron transport hosts for phosphorescent organic light emitting diodes, Organic letters, 9 (2007) 235-238.
[13] Y. Tao, Q. Wang, C. Yang, Q. Wang, Z. Zhang, T. Zou, J. Qin, D. Ma, A simple carbazole/oxadiazole hybrid molecule: an excellent bipolar host for green and red phosphorescent OLEDs, Angewandte Chemie, 120 (2008) 8224-8227.
[14] Y. Tao, Q. Wang, C. Yang, C. Zhong, K. Zhang, J. Qin, D. Ma, Tuning the optoelectronic properties of carbazole/oxadiazole hybrids through linkage modes: hosts for highly efficient green electrophosphorescence, Advanced Functional Materials, 20 (2010) 304-311.
[15] Y. Zhang, W. Haske, D. Cai, S. Barlow, B. Kippelen, S.R. Marder, Efficient blue-emitting electrophosphorescent organic light-emitting diodes using 2-(3, 5-di (carbazol-9-yl) phenyl)-5-phenyl-1, 3, 4-oxadiazole as an ambipolar host, RSC Advances, 3 (2013) 23514-23520.
[16] Y. Tao, C. Yang, J. Qin, Organic host materials for phosphorescent organic light-emitting diodes, Chemical Society Reviews, 40 (2011) 2943-2970.
[17] H. Fukagawa, K. Watanabe, S. Tokito, Efficient white organic light emitting diodes with solution processed and vacuum deposited emitting layers, Organic Electronics, 10 (2009) 798-802.

Chapter 6

Charge Transport and Recombination in Heterostructure Organic Light Emitting Transistors

6.1 Introduction

Organic light-emitting field effect transistors are dual function devices in that they have the electroluminescence capabilities of organic light-emitting diodes plus the switching capabilities of a field effect transistor in a single architecture [1-5]. This dual functionality can potentially lead to new applications such as simplified pixels for flat panel displays and potentially an electrical driven organic semiconductor laser. Although the emission brightness of LEFETs has improved over the last decade [6-17], their electrical switching ON/OFF ratio and EQE at high brightness are still very much sub-optimal. This is in part due to a lack of knowledge with respect to materials design and the absence of a comprehensive understanding of the charge transport and radiative recombination processes that occur in a LEFET.

A common method to probe the charge transport in organic semiconductor films is to measure the optoelectronic characteristics of the material as a function of temperature in a FET or diode configuration [18-24]. Specifically, in the diode configuration both transient (e.g., Time-of-Flight [25], photo-Charge Extraction in Linearly Increasing Voltage [photo-CELIV] [26]) and steady-state measurements (e.g., Space Charge Limited Current [SCLC]) have been used to measure mobility and recombination. Recently, Armin et al. reported an adapted injection-CELIV technique called MIS-CELIV which is capable of measuring the mobility of both carrier types in diode architectures relevant to operational devices such as solar cells and photodiodes [27]. However, in a functional OLED, it needs to be simultaneously probe not only the transport properties, but also the recombination dynamics (radiative and non-radiative). Thus, the traditional transport measurement methodologies only uncover at best half the pertinent physics. Furthermore, these existing techniques require that the injecting contact must be ohmic. Such a requirement is hard to achieve in an organic diode configuration. In an OFET architecture, the contact resistance at the metal organic interface can be completely eliminated by employing four-probes or the transmission line technique [28-31]. An OFET structure can potentially map multiple elements of transport such as charge injection at the organic-metal interface, contact resistance and mobility. However, OFETs are generally not designed to emit light and are thus, like the simple diode, not suitable for studying radiative and non-radiative recombination processes.

In this Chapter, we simultaneously probe the mobility and injection of carrier types, contact resistance and radiative recombination all as a function of temperature in a model bilayer LEFET. As it is typically difficult to find an organic semiconductor material that is highly luminescent and with high charge carrier mobility a bilayer LEFET architecture, consisting of a highly luminescent emissive layer (SY) and a separate charge transport layer (DPP-DTT), was employed. The bilayer LEFETs show decreases in the source-drain current, mobility (both electrons and holes), and brightness with decreasing the temperature. However, the external quantum efficiency increases by an order of magnitude at low temperatures. The changes in mobility and current are thermally activated consistent with the hopping transport characteristics normally associated with disordered semiconductors. It was thus demonstrated that the increase in EQE at low temperature is predominately due to an increase in the radiative recombination efficiency.

6.2 Experimental procedure

6.2.1 Device fabrication

Figure 6.1.a shows the device architecture for top-contact, bottom-gate LEFETs. The devices were fabricated on 400 nm thick SiNx gate dielectric layer, grown by low pressure physical vapor deposition (LPCVD), on top of a heavily *n*-doped silicon wafer purchased from Silicon Quest, International, Inc. After dicing the wafer into 15 x 15 mm substrates, they were cleaned as explained in Chapter 2. All remaining fabrication steps and device testing were performed inside a nitrogen filled MBraun glove box (O2 and H2O levels < 0.1 ppm). The gate dielectric layer was further passivated with poly (methylmethacrylate) (PMMA) (120,000 gmol) as an organic dielectric layer. A 35 mg/ml solution of PMMA in n-propylacetate (P99.5%) was spin-coated onto the substrates at 2500 rpm for 30 s and then 3000 rpm for 10 s. The substrates were then baked on a hot plate at 150 °C for 30 min. The PMMA film thickness was 120 nm. The materials used for the semiconducting channel were: an ambipolar diketopyrrolopyrrole-dithienothiophene (DPP-DTT) co-polymer [32]; and Super Yellow (SY), a phenyl-substituted poly(p-phenylenevinylene) co-polymer, as the emissive layer. SY (PDY–132) was purchased from Merck and was used without

further purification and DPP-DTT copolymer was provided by our collaborator with M_n =20 kDa, M_w = 50 kDa, and PDI = 2.5. The reported chemical structures for both these polymers are illustrated in Figure 6.1.b and c. The DPP-DTT layer was deposited on top of the PMMA layer from a 4 mg/ml solution in chloroform with 7% of 1,2 dichlorobenzene (≥99 %, anhydrous). In order to fully dissolve the DPP-DTT polymer, the solution was heated at 80 °C followed by a slow cooling protocol [33] and spin-coated at 1000 rpm for 60 s. This step was followed by baking the sample on a hot plate at 150 °C for 30 min. A 7 mg/ml solution of SY in toluene (>99.9% anhydrous) was spin-coated on top of the DPP-DTT layer at 2500 rpm for 30 s then at 3000 rpm for 10 s. The substrates were then annealed on a hot plate at 150 °C for 30 min. The LEFETs were completed by deposition of asymmetric electrodes under vacuum (2 x 10^{-6} mbar) through shadow masks (see Figure 6.1.d) prepared by deep reactive ion etching with channel widths of 16 mm and four different channel lengths 50, 80, 100 and 120 µm. Asymmetric source and drain contacts were deposited in two separated evaporations, first Au (hole injection) and then Ba (electron injection). The two metals were chosen due to their work functions being good matches for the relevant semiconductor energy levels to ensure optimized charge injection [17]. Devices were encapsulated with drop casting of Cytop CTL-809M (solvent: CTSolv.180) from Asahi Glass Japan.

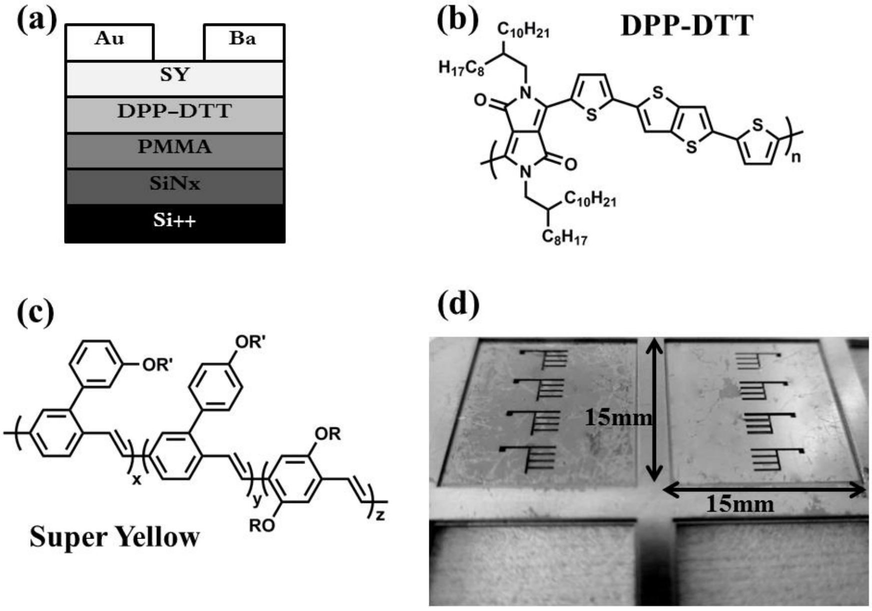

Figure 6.1 a) Schematic LEFET device architecture using asymmetric source and drain contacts; b) Chemical structure for DPP-DTT; c) chemical structure of Super Yellow; d) asymmetric shadow masks inside holder which used for contact deposition.

6.2.2 Temperature dependent measurement

A Janis closed-cycle Helium Opti-Cryostat (See Figure 6.2.a) was used for the temperature dependent measurements from 300 K to 135 K. The LEFET was connected to an electrical chip as shown in Figure 6.2.b and was mounted onto the cryostat finger, the sample chamber was evacuated (5×10^{-5} mbar) and refilled with He. The devices were cooled down from ambient and at each temperature, transfer and output characteristics, and emission intensity were recorded simultaneously for both electron and hole accumulation modes. Electrical characteristics of the devices were acquired using an Agilent B1500A Semiconductor Device Analyser at each temperature. The emission was recorded as photocurrent with a calibrated photomultiplier tube (PMT) positioned at one of the optical windows of the cryostat. The brightness was calculated from the PMT photocurrent by comparison with a device with known brightness as explained in Section 2.5.4.1 [15]. The EQE was calculated from the ratio of emitted photons to the number of injected charge carriers, which were extracted from the brightness and source-drain current, respectively, assuming Lambertian emission as described by Greenham et al [34].

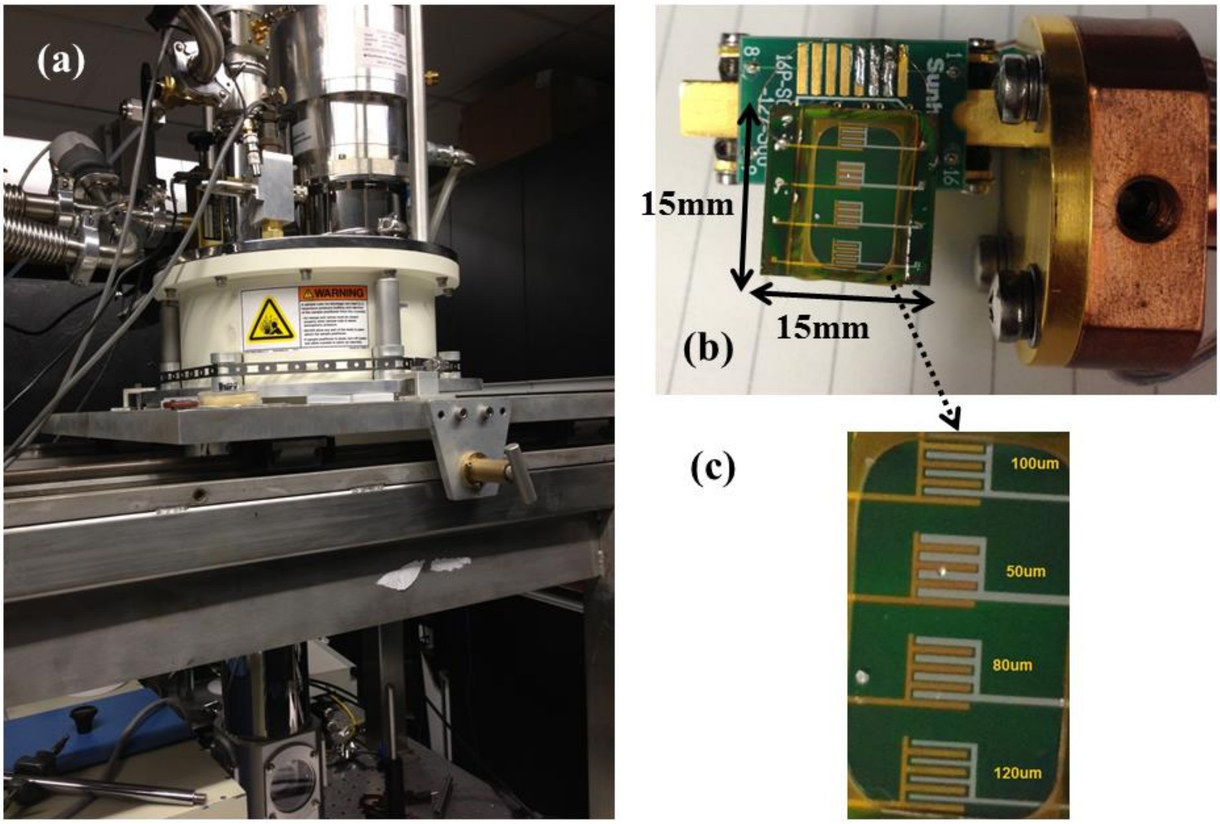

Figure 6.2 a) cryostat set up; b) encapsulated sample on chip with all electrical connections; c) optical images of LEFETs with different channel widths on one substrate.

The charge carrier mobility (**μ**) was calculated in the saturation regime as explained in Section 2.5.4.2 while the gate capacitance is comprised of the SiNx and PMMA layers, which were estimated as the sum of the capacitors in series.

The LEFETs shadow masks were designed to have four devices on each substrate with the same channel width but different channel length as shown in Figure 6.2.c In order to extract the intrinsic mobility, the total resistance was deduced from the output characteristics at different temperatures and for at least three devices with different channel lengths on one substrate. The contact resistance was extracted by extrapolating the intercept for a channel length equal to zero as shown in schematic diagram of Figure 6.3. Intrinsic mobilities were calculated as per standard procedures will be explained later in this Chapter [35-39].

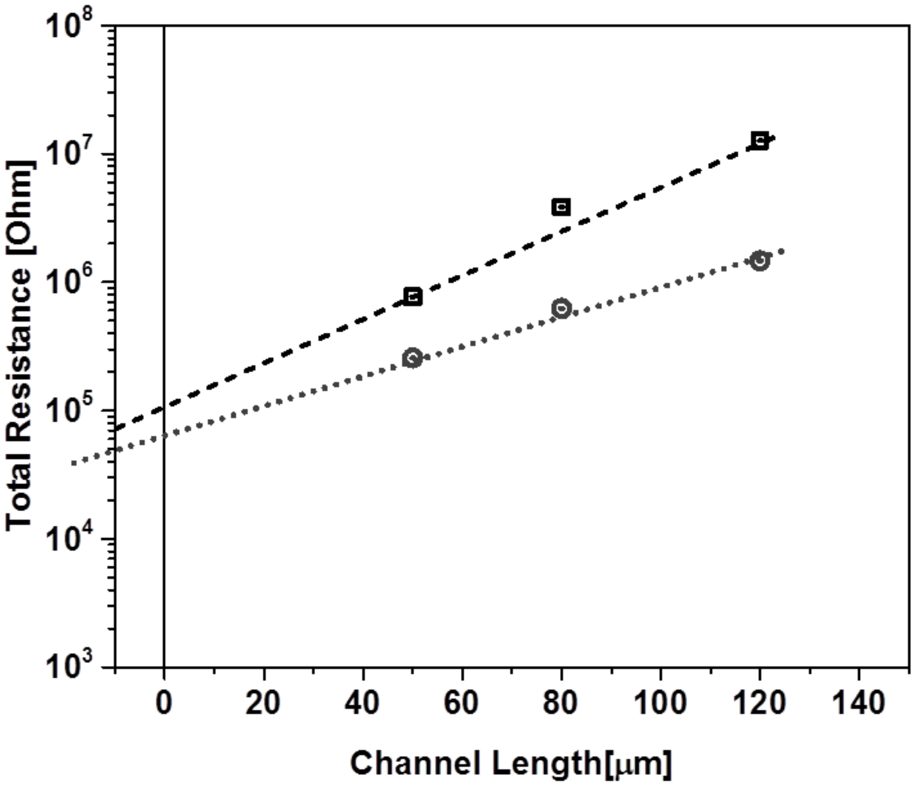

Figure 6.3 Schematic diagram of extraction the contact resistance from devices with different channel lengths.

6.2.3 Photoluminescence quantum yield measurement

The thin film PLQY measurements at room temperature were performed using the method described by Greenham et al [40]. Films of Super Yellow were spin-cast from toluene solutions with concentrations of ~7 mg/ml onto fused silica substrates, which were subsequently annealed at 150 °C for 30 min. The films were photo-excited with the 442 nm output of a HeCd laser that was attenuated with neutral density filters to ~0.2 mW. The interior of the integrating sphere was flushed with nitrogen for the duration of the measurement to minimize photodegradation, and the PL intensity was measured with a calibrated photodiode. The PLQY was measured at 4 points on the film and the results averaged.

For the temperature-dependent PLQY measurements, the film was placed inside an Oxford Instruments Optistat DN2 cryostat in a helium atmosphere. The same excitation source was used as for the room temperature-dependent measurements, although the power incident on the film was reduced to ~5 μW to minimize damage to the sample from sustained excitation. The films had absorbance at the excitation wavelength of ~1 so the majority of the incident light was absorbed. Two detectors were used to monitor the PL signal: a fibre coupled Ocean Optics USB2000 spectrometer, and a Si photodiode. Both were placed close to the sample with a long pass filter covering the photodiode to block any scattered excitation. The change in PLQY with temperature was estimated by comparing the relative change in the PL signal intensity between room temperature and a range of low temperatures. The emission from SY films is not isotropic so the emission was measured from multiple angles with the results averaged. Furthermore, the measurements were performed by modulating between high and low temperatures rather than using a gradient in order to rule out any degradation effects.

6.3 Results and discussions

6.3.1 Room temperature

Figure 6.4.a and b show typical electrical transfer characteristics of the model LEFETs at room temperature where channel length and width were 50 μm and 16 mm, respectively. The gate voltage was scanned from -100 V to + 100 V while keeping the source–drain voltage at a fixed value of -100 V or +100 V. The electrical output characteristics at room temperature are shown in Figure 6.4.c and d, the devices demonstrated both diode-like and saturation regimes for hole and electron accumulation [39]. The diode-like characteristics (super-linear increase of drain current with source-drain voltages) are more prominent in *n*-channel mode (V_G = 0 to 60 V). Further increase in the gate voltage from 80 V to 100 V leads to accumulation of electrons, and the transistor operates fully in the *n*-channel mode. These characteristics are typical of ambipolar LEFETs [41].

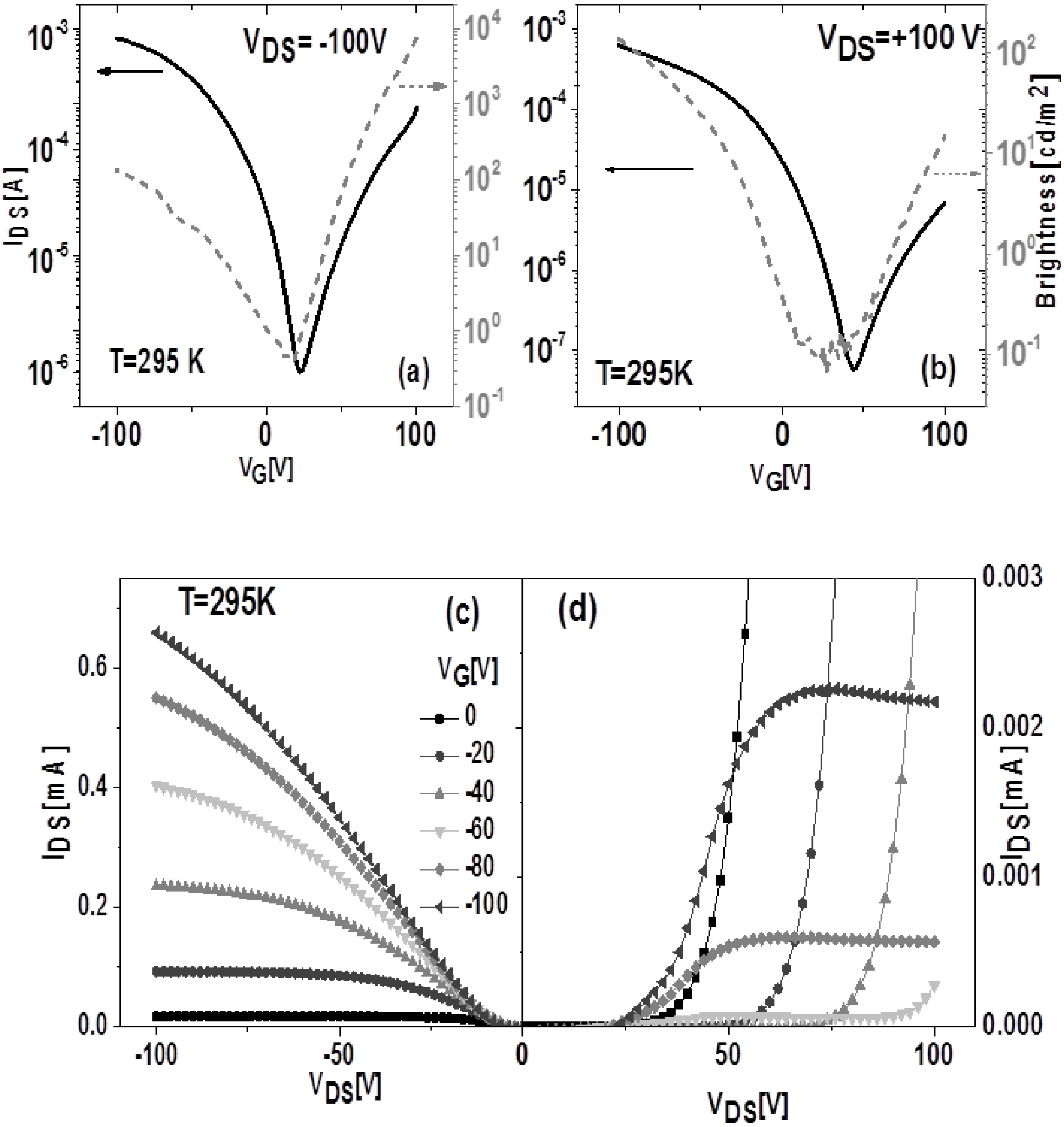

Figure 6.4 Electrical and optical characteristics of a typical LEFET at room temperature: a) source-drain current and brightness for *p*-mode, V_{DS} was kept constant at -100 V; b) source-drain current in *n*-mode, V_{DS} was kept constant at +100 V; c) and d) output characteristics for p and n modes, respectively. In all cases the channel length and channel width were 50 um and 16 mm, respectively.

Conduction of charge in the device occurs primarily at the DPP-DTT/PMMA dielectric interface. The field effect mobility at room temperature for both holes and electrons were calculated from the transfer characteristics in the saturation regims and found to be 0.06 cm^2/Vs and 0.002 cm^2/Vs, respectively. The electron mobility is lower than that previously reported for DPP-DTT/SY heterostructure LEFETs [41]. This is mainly due to different processing and testing condition of the samples (UV exposure during the encapsulation process; and environmental exposure during transfer to cryostat) and contact resistance (see Figure 6.4.c and d) associated with the electron injecting Ba electrode. Light emission (yellow-green colour) was clearly visible to the eye during device operation in both hole and electron accumulation modes. Figure 6.4.a and b show the brightness (cd/m^2) versus gate voltage for the LEFETs for hole and electron accumulation mode respectively (channel length and width of this device were 50 µm and 16 mm, respectively). The brightness increases with gate voltage, reaching 196 cd/m^2 with an EQE of 0.0013% in hole accumulation, and 21 cd/m^2 with an EQE of 0.038% for the electron accumulation.

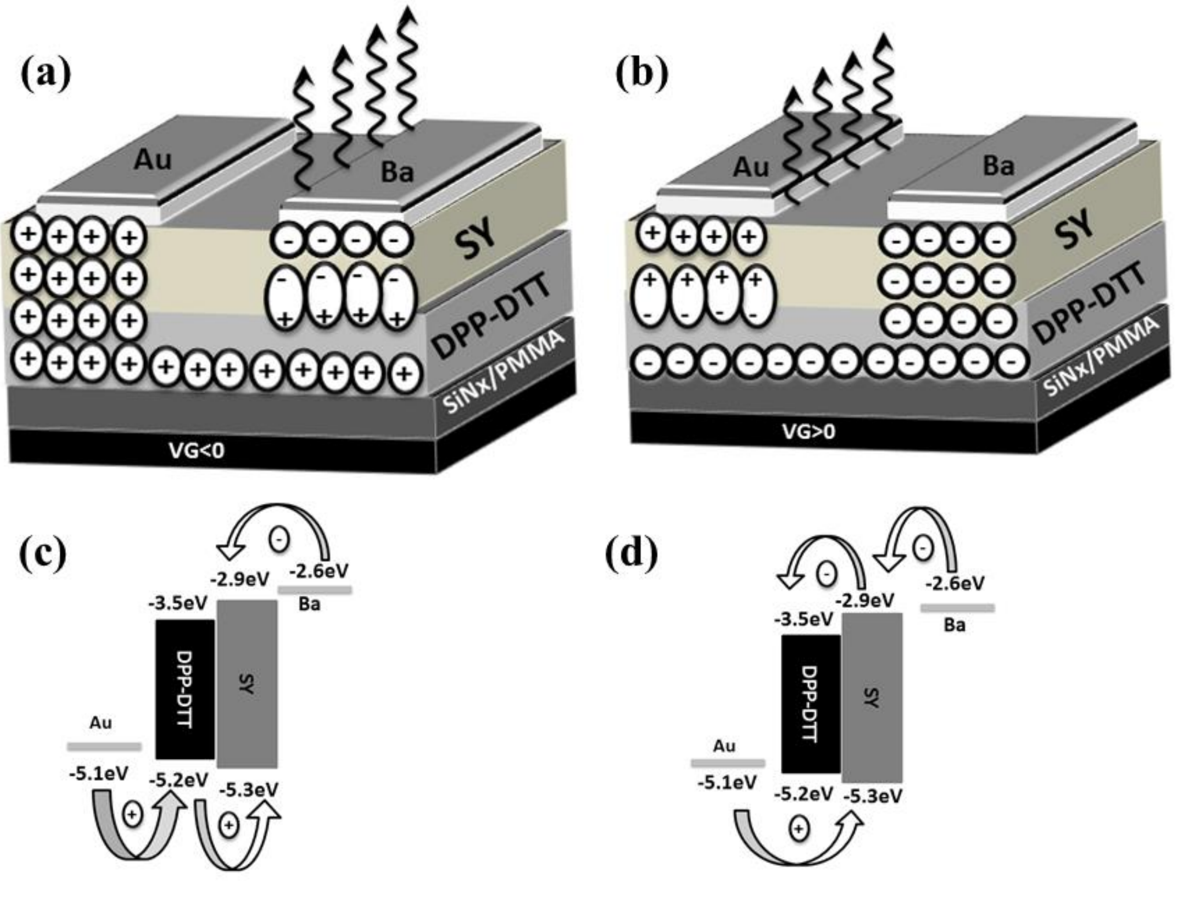

Figure 6.5 Operation mechanisms and energy level diagrams for the LEFETs: a) *p*-mode operation; b) *n*-mode operation; c) injection for *p*-mode; d) injection for *n*-mode.

Figure 6.5 shows the details of the operating mechanism along with the relevant energy levels of the semiconductors and contacts. For negative gate voltage ($V_G < 0$), positive charge carriers (holes) are accumulated at the semiconductor-dielectric interface and are the majority carrier in the LEFET, i.e., holes move towards the Ba electrode upon application of the source-drain voltage. These holes recombine with electrons injected from the Ba electrode (work function = 2.6 eV) into SY (EA = 2.9 eV) [17] resulting in exciton formation and subsequent light emission under the Ba electrode (see Figure 6.5.a and c). During operation in *n*-mode the applied gate voltage is positive and electrons are the dominant carrier in the channel. In this mode, electrons are transported toward the hole injecting contact leading to exciton formation and light emission under the Au electrode (see Figure 6.5.b and d). The emission mechanism is thus relatively straightforward to understand, enabling straightforward analyse of the device outputs under varying experimental conditions.

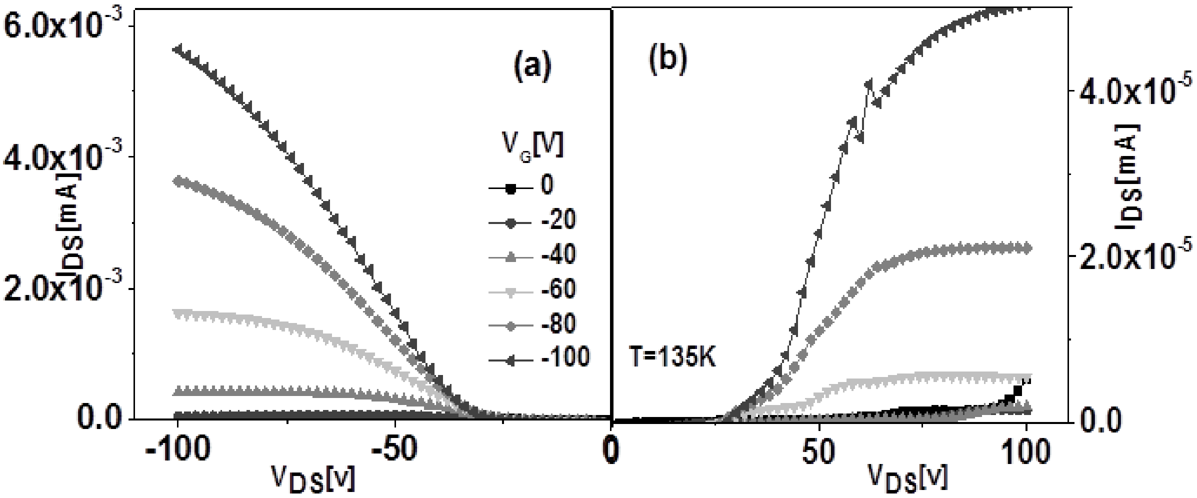

Figure 6.6 Output characteristics at 135 K for (a) Hole; (b) Electron accumulation modes. Channel length and width were 50 µm and 16 mm, respectively

6.3.2 Variable temperature mobility measurements

Figure 6.6 shows typical output characteristics with clear linear and saturation regimes of the LEFETs for both modes (channel length and width of this device were 50 µm and 16 mm, respectively) at an example temperature of 135 K. Figure 6.7.a and b show typical electrical characteristics from 295 K to 135 K for *p*-mode and *n*-mode operation, respectively. As the temperature decreases, the drain current decreases in both *p*- and *n*-channel modes. At low temperatures, the LEFETs demonstrate linear, diode-like and saturation regimes for both hole and electron accumulation. Below 175 K, the off-current drops significantly – this is associated with the freezing of free carriers as expected in a disordered semiconductor dominated by hopping transport physics [20]. From room temperature to 135 K, the mobility was found to depend strongly on temperature and the gate voltage. Figure 6.8 shows the plot of mobility (from the *p*-mode characteristics) versus inverse temperature for V_G = -15, -20 , -30, -40 and -50 V, for the 50 µm channel length and 16 mm channel width device at a constant source-drain voltage of -100 V. This data is consistent with a thermally activated hopping model [20], but one needs also to account for any possible temperature dependence of the contact resistance, which now is addressed to finally determine the intrinsic mobilities.

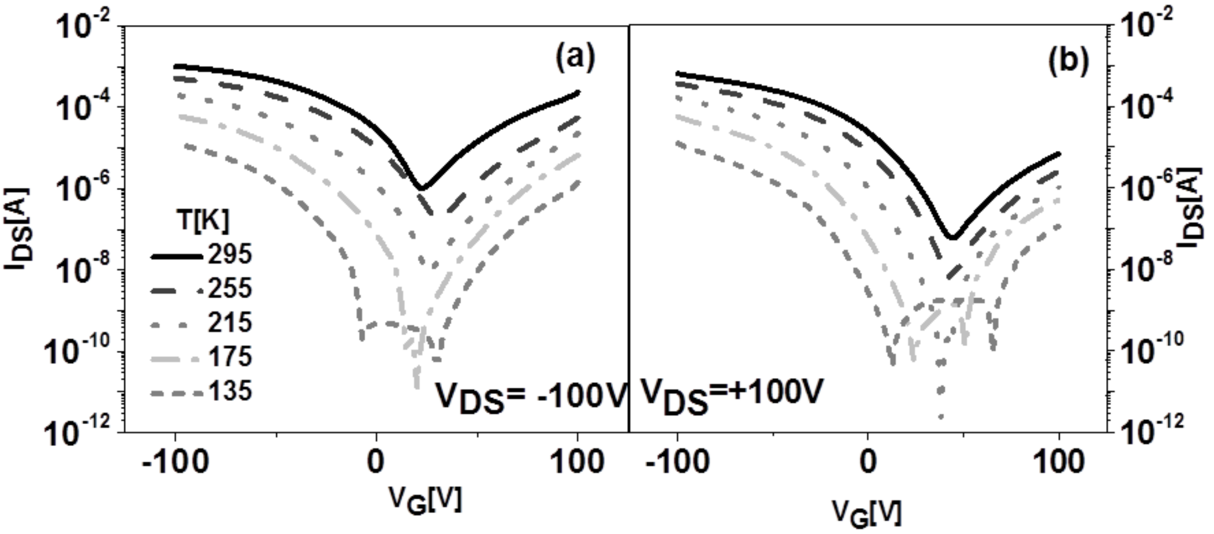

Figure 6.7 a) Source–drain current at different temperatures for *p*-mode at V_{DS}=-100 V; b) Source-drain current at different temperatures while V_{DS} was constant at +100 V.

Figure 6.9.a shows contact resistance (Rc) and channel resistance (Rch) for hole accumulation mode as a function of gate voltages at room temperature and 175 K. The total resistance (Rt = Rch + Rc) was extracted from the output characteristics as a function of gate voltage and temperature. Having the total resistance for at least three devices with different channel lengths on one substrate allows us to extrapolate the contact resistance from the zero channel (see Figure 6.3). The rationale behind using data from devices on the same substrate is to avoid any effect of changing film morphology and other fabrication inconsistencies. Overall, it has been found that the channel resistance in the hole accumulation mode decreases as the gate voltage increases. This is expected, since as the gate voltage increase, the channel becomes more conducting due to the accumulation of holes. As the temperature is lowered (175 K), both contact resistance and channel resistance increase significantly. As such, the Schottky barrier height for hole injection from the semiconductor to the metal increases leading to higher contact resistance [42].

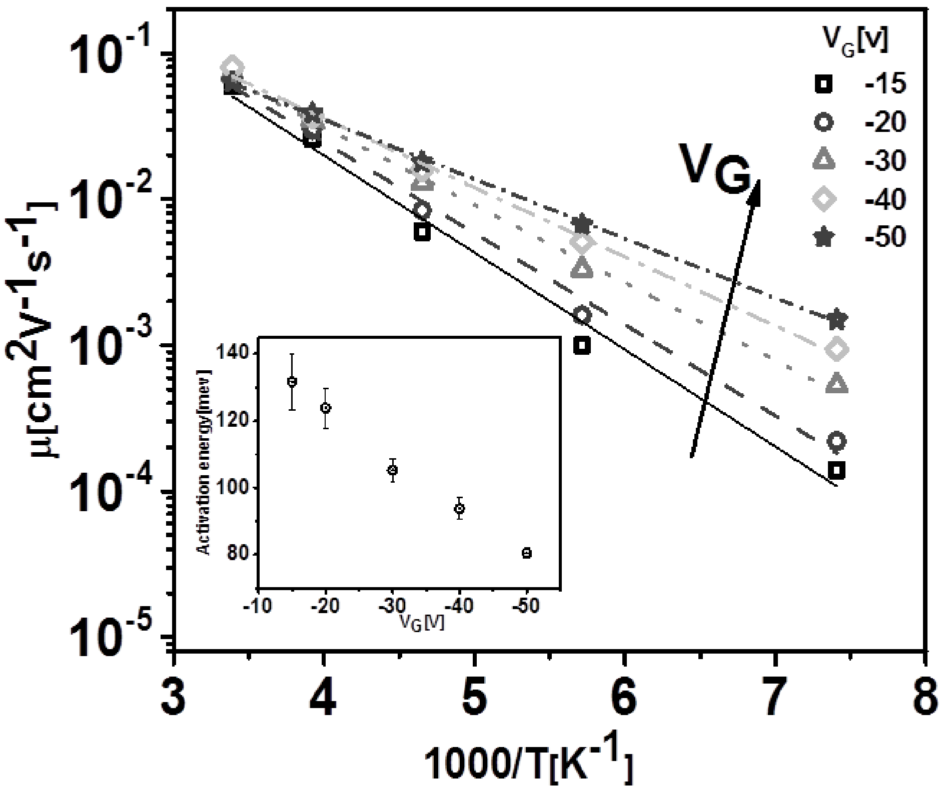

Figure 6.8 hole mobility as a function of temperature and gate voltage, and activation energy as a function of gate voltage (channel length and width were 50 um and 16 mm, respectively).

To accurately determine the activation energy of the intrinsic mobility was plotted (i.e., the mobility corrected with contact resistance) versus inverse temperature in a log-linear scale (see Figure 6.9.b). The intrinsic mobilities have been calculated from Equation 6.1 from the slope of the inverse channel resistance versus gate voltage [35-39]. Where μ_i is intrinsic mobility, L channel length, W channel width, C dielectric capacitance, R_{ch} channel resistance, and V_G gate voltage. Therefore the final intrinsic mobilities in this study are independent of gate voltage and contact resistance.

$$\mu_i = \frac{L}{WC}\frac{\partial\left({R_{ch}}^{-1}\right)}{\partial(V_G)} \tag{6.1}$$

The intrinsic mobilites are higher than the contact limited mobilities and follow the Arrhenius Equation with thermally activated charge transport. The calculated activation energy E_t = 114 meV for holes, which is only slightly higher than reported activation energy for DPP-DTT-based FETs [32].

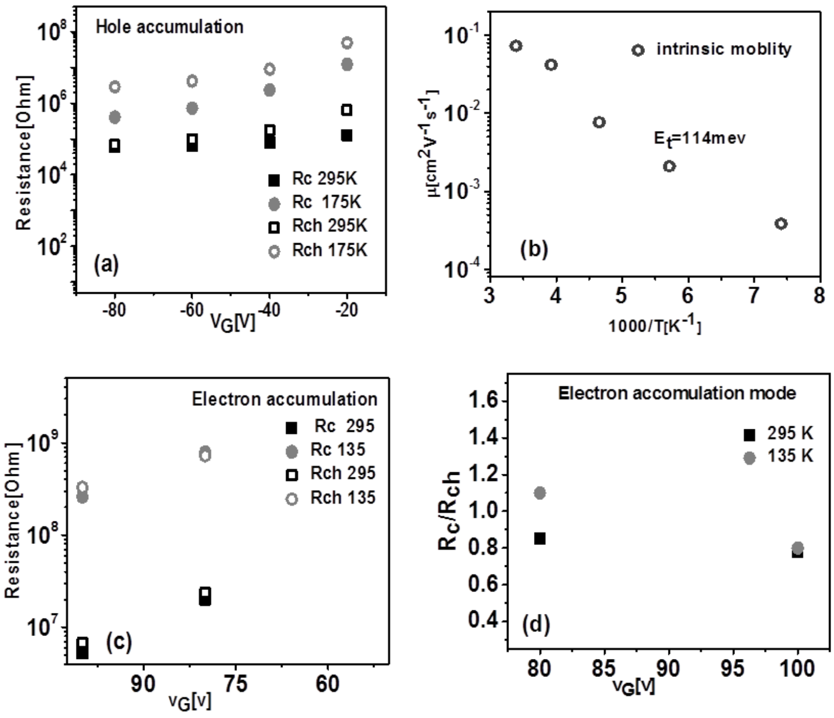

Figure 6.9 a) Contact resistance and channel resistance as a function of gate voltage at two different temperatures; b) intrinsic hole mobility as a function of temperature; c) contact and channel resistances as function of gate voltage for two different temperatures; d) ratio of contact and channel resistances for different gate voltages and temperatures. All plots are for electron accumulation mode. In all cases channel length and width were 50 µm and 16 mm, respectively.

For the electron accumulation mode, Figure 6.9.c shows similar trends in the contact resistance (Rc) and channel resistance (Rch) ($V_G > 80$ V) as a function of gate voltages at room and 135 K. it was noted, for $V_G < 80$ V, extraction of Rc and Rch is not valid due to the super-linear increase of the source-drain voltage, i.e., the device is in diode like mode. For $V_G > 80$ V, it has been found that: i) Rc is comparable to Rch; and ii) for the whole temperature range, the ratio of Rc/Rch ~1(see Figure 6.9.d). Under these conditions, it was concluded that the operating mechanism in *n*-channel is dominated not only by the contact resistance but also trapping. Therefore, it is not possible to reliable determine the intrinsic mobility in electron accumulation mode.

6.3.3 Variable temperature radiative recombination efficiency

Figure 6.10.a shows the temperature dependence of the emission brightness versus gate voltage for the hole accumulation mode for a device with channel length and width of this device were 50 µm and 16 mm, respectively. Reiterating at this point that the emission arises from Super Yellow. At temperatures above 135 K, the LEFETs exhibit high signal to noise optical output characteristics. Below 135 K, the data is not reliable due to a high gate leakage current and hence

the measured brightness was comparable to the noise floor of the measurement instrumentation. In general, as the temperature was decreased, the brightness decreased. For example, in hole accumulation mode, the brightness dropped from 196 cd/m^2 at 295 K to 57 cd/m^2 at 135 K. For electron accumulation mode (see Figure 6.10.b), the brightness dropped from 24 cd/m^2 at 295 K to 3 cd/m^2 at 135 K. It is interesting to note that, the brightness decreased only by factor of ~10 from room temperature to 135K; whilst the drain current decreased by a factor of ~500 from room temperature to 135 K. These results suggest that the recombination dynamics are temperature dependent.

To gain additional insight into the light emission and recombination processes, EQE was also measured as a function of gate voltage and temperature. For both hole (see Figure 6.10.c) and electron (see Figure 6.10.d) accumulation modes, the EQE increases as the temperature decreases. The maximum EQE was 0.3% at 135 K in the electron accumulation mode. This is an improvement by a factor 10 in terms of light emission compared to room temperature. For the hole accumulation mode, the EQE was 0.03% at 135 K. It was noted, in the ambipolar region of operation (V_G 25 V to –25 V) the PMT photocurrent was equal to the noise floor and hence the EQE could not be calculated in this region. Conventionally, the EQE is governed by the product of four different parameters according to:

$$\boldsymbol{\phi_{EQE} = \phi_{escape} \times \phi_{capture} \times \phi_{spin} \times \phi_{PLQY}} \qquad (6.2)$$

where ϕ_{escape} is the photon out-coupling factor (~ 0.20) [43]; $\phi_{capture}$ is the fraction of electrons and holes that recombine to form excitons (the recombination efficiency); ϕ_{spin} is related to the spin statistics for the formation of singlet or triplet excitons - in this case SY is singlet emitter so ϕ_{spin}= 0.25; and ϕ_{PLQY} is the photoluminensce quantum yield in the solid state (measured to be 65% at room temperature). The ϕ_{escape} and ϕ_{spin} components are expected to be independent of temperature, as these are related to the device geometry, and the type of emitter (singlet as used in this study), respectively. The PLQY is expected to be temperature dependent, as the non-radiative rate generally decreases with temperature in organic semiconducting fluorophores such as SY. Figure 6.11 shows the temperature dependence of the PLQY and it notes the change is smaller than expected given change in measured EQE, and taking into account Equation 6.2. By elimination, one must therefore conclude that the recombination efficiency ($\phi_{capture}$) plays a significant role in the temperature dependence of the EQE in these LEFETs. The reason for this strong dependency of the recombination efficiency on temperature is not completely clear but could be associated with an increased charge trapping at low energy sites and/or the two carrier concentrations becoming balanced at low temperatures.

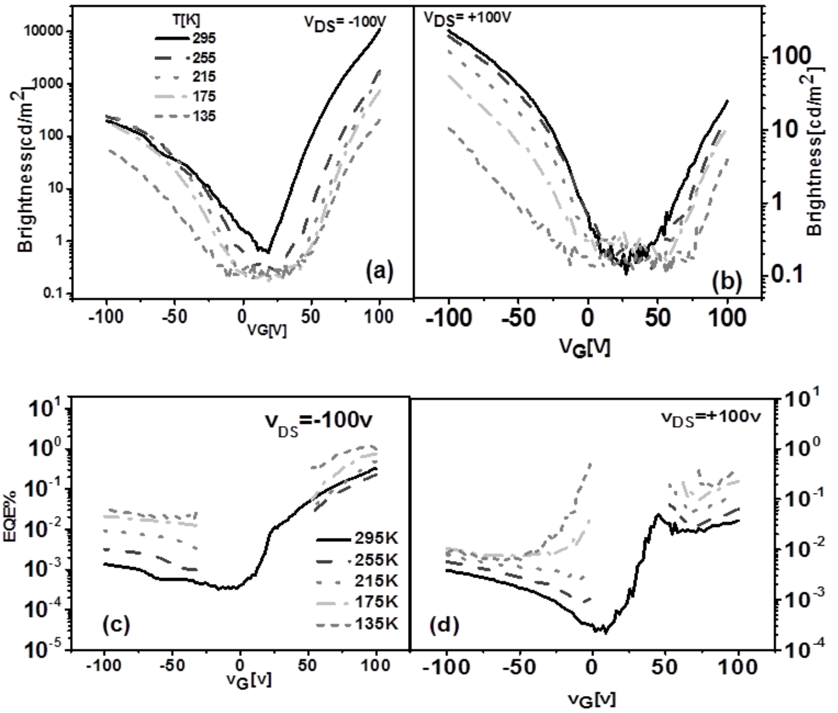

Figure 6.10 Brightness at different temperatures for a) *p*-mode operation; b) *n*-mode operation; EQE at different temperatures for c) *p*-mode operation; d) *n*-mode operation. Note that devices had channel lengths and widths of 50 µm and 16 mm, respectively.

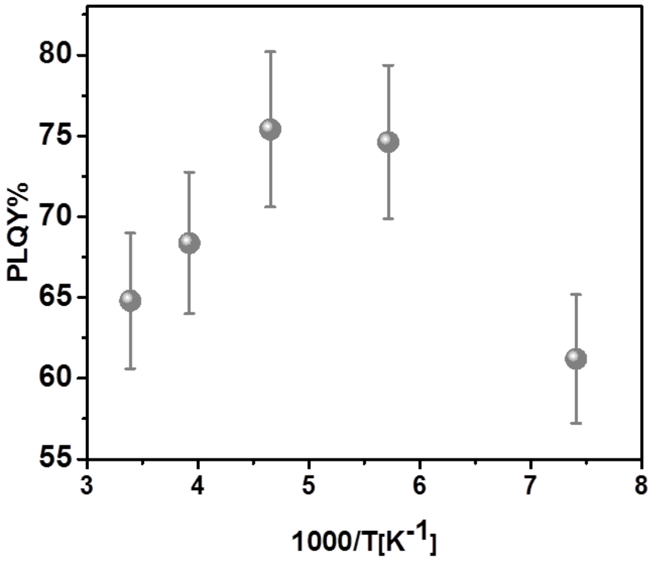

Figure 6.11 Photoluminescence Quantum Yield of a thin film of Super Yellow (emissive layer) on fused silica substrates as function of temperature.

6.4 Conclusion

In summary, charge transport (mobility and charge injection) and emissive (radiative recombination, brightness, EQE) properties of organic semiconducting polymers were measured in a heterostructure light-emitting field effect transistor. Our results demonstrate that, as the LEFET was cooled down, the intrinsic hole mobilities follow an Arrhenius response with activation energy of E_t = 114 meV and the overall EQE increases. While the PLQY of the emissive polymer increases with decreasing temperature it is insufficient to explain the improved EQE. Therefore, the improved EQE at low temperature is primarily due to an increased radiative recombination. Our results establish some basic rules for engineering high radiative efficiencies in light-emitting field effect transistors, which should aid in both materials and architecture design.

References

[1] A.J. Heeger, N.S. Sariciftci, E.B. Namdas, Semiconducting and metallic polymers, Oxford University Press, 2010.
[2] M. Muccini, A bright future for organic field-effect transistors, Nature materials, 5 (2006) 605-613.
[3] M. McCarthy, B. Liu, E. Donoghue, I. Kravchenko, D. Kim, F. So, A. Rinzler, Low-voltage, low-power, organic light-emitting transistors for active matrix displays, Science, 332 (2011) 570-573.
[4] M. Ahles, A. Hepp, R. Schmechel, H. von Seggern, Light emission from a polymer transistor, Applied physics letters, 84 (2004) 428-430.
[5] E.B. Namdas, J.S. Swensen, P. Ledochowitsch, J.D. Yuen, D. Moses, A.J. Heeger, Gate-Controlled Light Emitting Diodes, Advanced Materials, 20 (2008) 1321-1324.
[6] E.B. Namdas, P. Ledochowitsch, J.D. Yuen, D. Moses, A.J. Heeger, High performance light emitting transistors, Applied Physics Letters, 92 (2008) 183304.
[7] A. Hepp, H. Heil, W. Weise, M. Ahles, R. Schmechel, H. von Seggern, Light-emitting field-effect transistor based on a tetracene thin film, Physical review letters, 91 (2003) 157406.
[8] J. Veres, S. Ogier, G. Lloyd, D. De Leeuw, Gate insulators in organic field-effect transistors, Chemistry of Materials, 16 (2004) 4543-4555.
[9] R. Naber, M. Bird, H. Sirringhaus, A gate dielectric that enables high ambipolar mobilities in polymer light-emitting field-effect transistors, Applied Physics Letters, 93 (2008) 023301.
[10] B.B. Hsu, J. Seifter, C.J. Takacs, C. Zhong, H.-R. Tseng, I.D. Samuel, E.B. Namdas, G.C. Bazan, F. Huang, Y. Cao, Ordered polymer nanofibers enhance output brightness in bilayer light-emitting field-effect transistors, ACS nano, 7 (2013) 2344-2351.
[11] J.H. Seo, E.B. Namdas, A. Gutacker, A.J. Heeger, G.C. Bazan, Conjugated polyelectrolytes for organic light emitting transistors, Applied Physics Letters, 97 (2010) 043303.
[12] J.H. Seo, E.B. Namdas, A. Gutacker, A.J. Heeger, G.C. Bazan, Solution-Processed Organic Light-Emitting Transistors Incorporating Conjugated Polyelectrolytes, Advanced Functional Materials, 21 (2011) 3667-3672.
[13] E.B. Namdas, B.B. Hsu, J.D. Yuen, I.D. Samuel, A.J. Heeger, Optoelectronic Gate Dielectrics for High Brightness and High-Efficiency Light-Emitting Transistors, Advanced Materials, 23 (2011) 2353-2356.
[14] B.B. Hsu, C. Duan, E.B. Namdas, A. Gutacker, J.D. Yuen, F. Huang, Y. Cao, G.C. Bazan, I.D. Samuel, A.J. Heeger, Control of Efficiency, Brightness, and Recombination Zone in Light-Emitting Field Effect Transistors, Advanced Materials, 24 (2012) 1171-1175.
[15] M. Ullah, K. Tandy, S.D. Yambem, M. Aljada, P.L. Burn, P. Meredith, E.B. Namdas, Simultaneous enhancement of brightness, efficiency, and switching in RGB organic light emitting transistors, Advanced Materials, 25 (2013) 6213-6218.
[16] E.B. Namdas, B.B. Hsu, Z. Liu, S.C. Lo, P.L. Burn, I.D. Samuel, Phosphorescent Light-Emitting Transistors: Harvesting Triplet Excitons, Advanced Materials, 21 (2009) 4957-4961.
[17] K. Tandy, M. Ullah, P.L. Burn, P. Meredith, E.B. Namdas, Unlocking the full potential of light emitting field-effect transistors by engineering charge injection layers, Organic Electronics, 14 (2013) 2953-2961.
[18] G. Horowitz, R. Hajlaoui, P. Delannoy, Temperature dependence of the field-effect mobility of sexithiophene. Determination of the density of traps, Journal de Physique III, 5 (1995) 355-371.
[19] I. Hulea, S. Fratini, H. Xie, C. Mulder, N. Iossad, G. Rastelli, S. Ciuchi, A. Morpurgo, Tunable Fröhlich polarons in organic single-crystal transistors, Nature Materials, 5 (2006) 982-986.
[20] H. Bässler, Charge transport in disordered organic photoconductors, phys. status solidi b, 175 (1993) 15-56.
[21] N.F. Mott, E.A. Davis, Electronic processes in non-crystalline materials, Oxford University Press, 2012.

[22] M. Ullah, PhD dissertation , Johannes Kepler University, Linz (2011).
[23] S. Nelson, Y.-Y. Lin, D. Gundlach, T. Jackson, Temperature-independent transport in high-mobility pentacene transistors, Applied physics letters, 72 (1998) 1854-1856.
[24] A. Brown, C. Jarrett, D. De Leeuw, M. Matters, Field-effect transistors made from solution-processed organic semiconductors, Synthetic metals, 88 (1997) 37-55.
[25] G. Juska, K. Arlauskas, R. Österbacka, H. Stubb, Time-of-flight measurements in thin films of regioregular poly (3-hexyl thiophene), Synthetic metals, 109 (2000) 173-176.
[26] A. Armin, M. Velusamy, P.L. Burn, P. Meredith, A. Pivrikas, Injected charge extraction by linearly increasing voltage for bimolecular recombination studies in organic solar cells, Applied Physics Letters, 101 (2012) 083306.
[27] A. Armin, G. Juska, M. Ullah, M. Velusamy, P.L. Burn, P. Meredith, A. Pivrikas, Balanced Carrier Mobilities: Not a Necessary Condition for High-Efficiency Thin Organic Solar Cells as Determined by MIS-CELIV, Advanced Energy Materials, 4 (2014).
[28] M.N. Islam, B. Mazhari, An analytical model for current crowding and source contact resistance in top-contact organic thin-film transistors, Semiconductor Science and Technology, 23 (2008) 125027.
[29] M. Shur, T. Fjeldly, T. Ytterdal, K. Lee, Unified MOSFET model, Solid-state electronics, 35 (1992) 1795-1802.
[30] G. Reeves, H. Harrison, Obtaining the specific contact resistance from transmission line model measurements, Electron Device Letters, IEEE, 3 (1982) 111-113.
[31] A.K. Agarwal, B. Mazhari, Simultaneous extraction of source and drain resistances in top contact organic thin film transistors from a single test structure, Organic Electronics, 13 (2012) 2659-2666.
[32] J. Li, Y. Zhao, H.S. Tan, Y. Guo, C.-A. Di, G. Yu, Y. Liu, M. Lin, S.H. Lim, Y. Zhou, A stable solution-processed polymer semiconductor with record high-mobility for printed transistors, Scientific reports, 2 (2012).
[33] P. Wolfer, A. Armin, A. Pivrikas, M. Velusamy, P.L. Burn, P. Meredith, Solution structure: defining polymer film morphology and optoelectronic device performance, J. Mater. Chem. C, 2 (2013) 71-77.
[34] N.C. Greenham, R.H. Friend, D.D. Bradley, Angular Dependence of the Emission from a Conjugated Polymer Light-Emitting Diode: Implications for efficiency calculations, Advanced Materials, 6 (1994) 491-494.
[35] T. Van Woudenbergh, P. Blom, M. Vissenberg, J. Huiberts, Temperature dependence of the charge injection in poly-dialkoxy-p-phenylene vinylene, Applied Physics Letters, 79 (2001) 1697-1699.
[36] L. Bürgi, T. Richards, R. Friend, H. Sirringhaus, Close look at charge carrier injection in polymer field-effect transistors, Journal of Applied Physics, 94 (2003) 6129-6137.
[37] H. Klauk, G. Schmid, W. Radlik, W. Weber, L. Zhou, C.D. Sheraw, J.A. Nichols, T.N. Jackson, Contact resistance in organic thin film transistors, Solid-State Electronics, 47 (2003) 297-301.
[38] J. Zaumseil, K.W. Baldwin, J.A. Rogers, Contact resistance in organic transistors that use source and drain electrodes formed by soft contact lamination, Journal of Applied Physics, 93 (2003) 6117-6124.
[39] E. Meijer, G. Gelinck, E. Van Veenendaal, B.-H. Huisman, D. De Leeuw, T. Klapwijk, Scaling behavior and parasitic series resistance in disordered organic field-effect transistors, Applied physics letters, 82 (2003) 4576-4578.
[40] N. Greenham, I. Samuel, G. Hayes, R. Phillips, Y. Kessener, S. Moratti, A. Holmes, R. Friend, Measurement of absolute photoluminescence quantum efficiencies in conjugated polymers, Chemical physics letters, 241 (1995) 89-96.

[41] M. Ullah, K. Tandy, J. Li, Z. Shi, P.L. Burn, P. Meredith, E.B. Namdas, High-Mobility, Heterostructure Light-Emitting Transistors and Complementary Inverters, Acs Photonics, 1 (2014) 954-959.
[42] T.D. Anthopoulos, C. Tanase, S. Setayesh, E.J. Meijer, J.C. Hummelen, P.W. Blom, D.M. de Leeuw, Ambipolar organic field-effect transistors based on a solution-processed methanofullerene, Advanced Materials, 16 (2004) 2174-2179.
[43] A. Boudrioua, P. Hobson, B. Matterson, I. Samuel, W. Barnes, Birefringence and dispersion of the light emitting polymer MEH–PPV, Synthetic metals, 111 (2000) 545-547.

Chapter 7

Summary, Conclusions, and Outlook

The focus of the work presented in this thesis is divided into two parts. The first focus was on a new, solution processable dendritic class of OLED materials emitting yellow-green colours suitable for mass production techniques such as spin coating and inkjet printing. The dendritic structure was employed to provide independent control over photophysical properties without negatively impacting on charge transport. Different approaches including altering the type and number of dendrons and polymerisation of dendrimers were investigated. Throughout the course of this study, both the photophysical properties and electro-optical performance of these materials in devices were characterised. The second part of this work was on the basic behaviour of organic semiconductors including the photophysics and recombination in the LEFET architecture. The outcome of these studies were towards the dual purpose of having more efficient solution processed OLEDs for industrial display technology with simpler electrical circuits provided by LEFETs.

In *Chapter 1*, a summary of the current work and working knowledge of the light emitting devices which motivated the studies in this thesis was described. This was followed by a summary of the basic theoretical background applicable to the studies on organic semiconductors, dendritic structures, photophysical concepts, and temperature dependent measurement methods. The operational mechanism for standard light emitting devices such as OLEDs and LEFETs were then discussed. Finally, a summary of the objectives of the study was provided.

The experimental methods, calculations, and materials used throughout the work presented in this thesis were outlined and explained in *Chapter 2*. This included diverse discussions from theoretical and experimental concepts of optical techniques to device fabrication and electrical characterisation. One of the challenges in this project was the characterisation of dipole orientation applicable to OLED devices. The dipole orientation had never before been tested at the Centre for Organic Photonics and Electronics. The angle dependent PL spectrum setup was established and tested on a reference sample according to prior work in literature.

In *Chapter 3*, the optical and electrical characterisation of a dendritic material using a reported iridium complex with biphenyl dendron was described. This work was undertaken as a reference in order to learn more about the photophysical and device performance of this class of materials. By introducing the electron transport layer TPBi in neat devices, the electron injection was enhanced. Further, this induced hole blocking at the recombination zone, providing higher recombination rates and consequently higher internal quantum efficiencies. The EQE was improved to 11.5% for neat devices. This result was ten times better than previously reported results (0.1%). The 23% outcoupling value from this device indicated the possibility of horizontal orientation for emissive dipoles. This could be justified with the anisotropic orientation of the layer underneath, which could dominate the orientation of emissive layer.

In *Chapter 4*, a novel approach was demonstrated for solution-processable phosphorescent materials by the integration of hole-transporting carbazole-based IrIII dendrimers (D1) into the polymer backbone to create poly-dendrimer (P1). The maximum EQE values for single layer dendrimer (D1) and poly(dendrimer) OLEDs were 4.5% and 7% respectively. These results indicated the advantages of polymerisation on device performance, possibly due to better film forming and charge balance. The performance of dendrimer D1 in both neat and blended devices confirmed the outcoupling of 22.5% and 25%, respectively. The most outstanding result was achieved for poly(dendrimer) with maximum EQE of 30% indicating 40% outcoupling, which haven’t been reported for solution processed devices before. This is double the theoretical limit of (20%) requiring additional investigation of dipole orientation. The angular dependent PL measurements were performed in this regard and revealed the ratio of 73% horizontal dipoles which is higher than isotropic material with 67%. Moreover, a similar result was found for poly(dendrimer) P1 which could be due to the heteroleptic structure of these compounds. This is a new and promising achievement as it allows more efficient OLEDs to be realised via modifications made to the intrinsic properties of the material.

Further in this chapter, the study was extended using the doubly-dendronised dendrimer (D2) via adding additional carbazole dendrons to the dendrimer D1. The photophysical properties of D1 and D2 were characterised as well as their performance in devices. By introducing the second dendron attached to the ligands of IrIII dendrimers, both the intra- and inter-chain inter-chromophore interactions could be controlled by core encapsulation, leading to higher PLQY values in the solid state and longer life times of the emissive species. A drawback of this approach was a red-shift in the emission colour due to an increase in conjugation length of the ligand. The EQE of 6% was obtained for D2 which is slightly higher than its singly-dendronised counterparts with 4.5% EQE. This double dendron approach to control optoelectronic properties was also used for poly(dendrimers), providing the extra advantage of higher solution viscosity.

Although, this family of materials has potential for host-free single layer OLED devices, blended emissive layers showed further reduction in inter-chromophore interaction and concentration quenching. Adding a second dendron (i.e., in going from D1 to D2 and P1 to P2) seems to have an impact on film packing and morphology of the emissive layer, both of which play a crucial role in influencing device performance.

In *Chapter 5*, an ambipolar solution processable poly(dendrimer) was described whereby electron-transporting moieties (oxadiazole) were integrated into a carbazole based poly(dendrimer). Different distributions of electron and hole moieties were applied in these designs. In spite of the balance between charge carrier types provided with this approach, the recombination rate could not be increased sufficiently. The conclusion drawn was that this is likely due to the disorder introduced into the system with the addition of the electron moieties as well as a decrease in PLQY caused by quenching.

By using the dual functionality of LEFETs, there is the potential to achieve simultaneous measurements of the charge transport (mobility and charge injection) and emissive properties (radiative recombination, brightness, EQE) of organic semiconducting polymers. This was taken advantage of with the temperature dependent experiments described in *Chapter 6*. The results demonstrated that, as the LEFET was cooled down, the intrinsic hole mobilities followed an Arrhenius response with activation energy of E_t = 114 meV, and the overall EQE increased. While the PLQY of the emissive polymer increased with decreasing temperature it was insufficient to explain the improved EQE. It was concluded that the improved EQE at low temperatures was primarily due to an increased radiative recombination. Our results established some basic principles for engineering high radiative efficiencies in LEFETs, which should aid in both material and architecture design.

As well as concluding this work and summarising the findings throughout this thesis, it is necessary to acknowledge the potential next steps generated by these findings as follows:

i) A prospective approach to further increase OLED device performance would be to make use of an exciplex forming co-host for the emissive materials. In this case, phosphorescent dendrimers or poly(dendrimers) would be the guest material, and a combination of electron- and hole transporting materials would be the requirements for the co-host. This approach can provide the necessary isolation between cores to prevent concentration quenching, as well as an ambipolar host, which could ease both charge injection and transport.

ii) A second outlook would be towards more studies on the horizontal orientation of emissive dipoles. This could significantly enhance the intrinsic properties of the emissive materials, achieving higher light out-put coupling and hence EQEs without the need for device modifications. One approach to achieve this is via the creation of an anisotropic emissive layer provided by the heteroleptic design of emissive materials, or alternatively an anisotropic host system.

iii) One of the advantages using dendritic structures is the ability to independently control optical properties of materials while maintaining the electrical properties. Therefore third outlook suggests altering the emitting color by means of other cores for red or blue. Giving poly(dendrimers) provided excellent outcoupling and device performance for green and yellow in the work presented in this thesis, this outlook can lead to having highly efficient GRB (green-red-blue) pixels in display technology. A key next step could be studying device stability and degradation which is crucial for display technology as well as lighting.

iv) Another approach toward highly efficient LEFET devices would be employing the planar anisotropic materials which simultaneously enhance the charge transport and direction of light emission. A combination of these ideas could be used in LEFET structures to provide improved OLED efficiency with switching advantages.

Transfer characteristics of single layer super yellow (SY) LEFET